A Systems Analysis of the Oxidative Stress Response in Breast Epithelia and Triple-Negative Breast Cancer

---

A dissertation

Presented to the faculty of the School of
Engineering and Applied Science in partial
fulfillment of the requirements for the degree of

Doctor of Philosophy

---

by

Elizabeth J. Pereira

May 2020

APPROVAL SHEET

This Dissertation
is submitted in partial fulfillment of the requirements
for the degree of
Doctor of Philosophy

Author Signature: ______________________

This Dissertation has been read and approved by the examining committee:

Advisor: Kevin A. Janes

Committee Member: Shayn M. Peirce-Cottler

Committee Member: Mete Civelek

Committee Member: Amy H. Bouton

Committee Member: Janet V. Cross

Accepted for the School of Engineering and Applied Science:

Craig H. Benson, School of Engineering and Applied Science

May 2020

Abstract

In order to survive, cells must sense and respond to countless internal and external stimuli. Some stimuli will induce stress, which triggers variable responses depending on the type, severity and duration of stress. For cells living in an aerobic environment, reactive oxygen species (ROS) are a continual source of stress that must be dealt with. ROS are reactive derivatives of oxygen produced by normal cellular metabolism and in response to various microenvironmental factors. Depending on concentration and context, ROS can promote cell signaling and proliferation or cause oxidative damage to biomolecules and apoptosis or senescence. To deal with these pervasive, potentially harmful species, cells are equipped with several pathways to sense and detoxify ROS.

In this dissertation, we use systems biology approaches to interrogate a stress-associated transcriptional state in breast mammary epithelial cells. Using several bioinformatic and analytical approaches, we identify the antioxidant transcription factor NRF2 as a candidate regulator of the group of transcripts. From there, we use molecular and cellular biology techniques, image processing, and computational modeling to decipher the broader NRF2 network responsible for oxidative stress handling. We uncover that NRF2 is activated together with another stress-responsive pathway, the p53 pathway, in single cells to mount a coordinated response to oxidative stress in 3D spheroid culture. NRF2–p53 coordination is retained in normal primary breast tissue and hormone-negative DCIS. However, the two pathways are largely uncoupled in triple-negative breast cancers, where p53 is usually mutated.

We then develop a computational systems model of NRF2–p53 signaling in response to transient perturbations in oxidative stress. Using the model, we robustly test hypotheses regarding NRF2–p53 network architecture and coordination during different stages of breast cancer. The integrated NRF2–p53 model predicts variable extents of uncoupling among TNBCs lines, and high uncoupling coincides with the most-severe 3D growth alterations upon NRF2 knockdown, suggesting a reduced tolerance for oxidative stress.

While previous research has focused on NRF2's direct interaction with mutated TNBC tumor suppressors, our work describes an important systems-level role for wild-type NRF2 and p53 in oxidative-stress tolerance of normal breast–mammary epithelia and hormone-negative premalignancies.

Acknowledgments

Completing my PhD research in the Biomedical Engineering department at the University of Virginia has been one of the most challenging, rewarding, and formative experiences of my life. I could not have done it without the help and support of so many people, to whom I dedicate this dissertation to.

To my advisor, Kevin Janes – thank you for being an amazing mentor. You have taught me too many things to enumerate so I will summarize by saying thank you for showing me what great science looks like and the dedication it requires to perform it. I'll never forget when we spoke on the phone the summer before I arrived in Charlottesville and you said being in the Janes lab was a way of life and I thought you were kidding…turns out you weren't. I feel very privileged to have conducted my PhD research in your lab and grateful for the impact you've had on my development as a scientist.

To my thesis committee, Drs. Shayn Peirce-Cottler, Mete Civelek, Amy Bouton, and Janet Cross – thank you for providing feedback and support throughout my dissertation. Your comments and critiques during committee meetings helped to make my project more well-rounded and prepared me well for questioning from outside audiences. Amy and Janet – thank you for taking the time to critically review and provide feedback on the NRF2-p53 manuscript before submission. Your comments made the document much stronger overall.

I'd also like to thank collaborators who helped with different aspects of the research presented in this dissertation. Dr. Kristen Atkins, thank you for your help finding and analyzing clinical samples and your instruction on breast pathology. Beyond the scientific contributions, I'd also like to thank you for your perspective on scientific communication. Much of the impact of scientific research rests on effective communication to broader audiences, and the skills I learned from the scientific communication workshop taught by you and Janet Cross I will continue to use throughout my career. I'd also like to thank Dr. Chun-Chao Wang, who I worked closely with for the first year of my graduate work and who helped with many of the initial experiments and bioinformatics analyses related to NRF2. Your ability to plan and carry out experiments so efficiently was valuable to see early on and were skills I tried to emulate during my PhD. I'd also like to thank Taylor Marohl, Lixin Wang, Page Murray, Joseph Burns, Christina Lee, and Delia Calderon for help on different aspects of the research presented in this dissertation.

To the Janes Lab – you guys made lab a fun and productive environment that I'm going to miss very much. Whether it was Beer Fridays sponsored by Sham's overzealous shopping or figuring out what was beeping in lab and how to fix it, we always had a great time together. It has been amazing to be surrounded by a group of fun, brilliant scientists and I wish you all the best in your future endeavors! #itsyourcareer

Sham and TK – I could not have done grad school without you both. You are two of the most fantastic people I've ever met and I can't thank you enough for the support, feedback, motivation, and LOLs that you guys provided me over the past 5.5 years. I'm so thankful for the experiences that we've shared and the life-long friendships that we made.

And last but not least to my family – thank you for always believing in me, even when I didn't believe in myself. Charissa – thank you for being a kind, supportive, loving older sister and setting an example that I strived to follow. Mom – you have been my loudest cheerleader since day one and I would not be where I am today without your constant love and support. Thank you for always reminding me that there's more to life than academics and for instilling in me a faith in God that has carried me through many trials in my life.

Table of Contents

Table of Figures

Chapter 1 Introduction

1.1 Foreword

In order to survive, cells must sense and respond to countless internal and external stimuli. Some stimuli will induce stress, which triggers different responses depending on the type, severity and duration of stress. One particularly ubiquitous stressor cells must deal with are reactive oxygen species (ROS), which are highly reactive byproducts of normal cellular metabolism. Low to moderate levels of ROS facilitate intracellular signaling and can promote cell proliferation (1–4), while high levels cause oxidative damage to biomolecules and induce cell death (5). High levels of ROS are also implicated in the pathogenesis of multiple diseases, including cancer (6,7). Several processes associated with cancer initiation and progression induce ROS production, including oncogenic signaling, increased metabolic rate, and matrix detachment, and thus cancer cells must devise ways to survive in a prooxidant environment (8–14). Understanding the complex intracellular effects of ROS and their regulation in cells are key to understanding cancer initiation and progression (15,16).

In this chapter, we provide background on the intrinsic subtypes of breast cancer and the heritable lesions associated with each, emphasizing the triple-negative/basal-like subtype which is the focus of the research presented in this dissertation. We give a brief introduction of ROS and the types of stress they cause in the cell. Next, we discuss the NRF2 pathway, the main pathway that detoxifies oxidative stress, and its role in cancer. Finally, we discuss the p53 pathway, the main pathway that deals with genotoxic stress in the cell, and its role in cancer.

1.2 The intrinsic subtypes of breast cancer

Gene expression profiling has classified breast cancer into four intrinsic subtypes: luminal A, luminal B, HER2-enriched, and basal-like (17,18). The subtypes are very distinct in terms of clinical and pathologic features and therefore have different prognostic and therapeutic implications (19). Luminal A and B comprise the hormone-receptor positive subtype defined by expression of estrogen receptor (ER) and/or progesterone receptor (PR). Luminal breast tumors are treated with ER or PR antagonists (20) and patients with these tumors generally have better prognosis than those with hormone-negative tumors (21–23). HER2-enriched tumors overexpress the human epidermal growth factor receptor 2 and are treated with HER2 receptor antagonists, mainly monoclonal antibodies that bind HER2 and interfere with signaling (24). Basal-like tumors, so named because of their expression of basal cytokeratins 5/6, 14 and 17 (25,26), are mostly "triple-negative" (18), meaning they lack ER/PR expression and do not overexpress HER2 (27,28). Patients with basal-like breast cancer have the worst prognosis of the four subtypes, partly because of a lack of treatment options (29). Since most basal-like tumors do not depend on hormone signaling or HER2 overexpression for growth, they do not respond to the standard of care targeted therapies that inhibit these receptors and receptor pathways, leaving chemotherapy as the only treatment option (30). In addition, basal-like tumors are highly heterogeneous, both inter- and intra-tumorally, contributing to their poor prognosis and lack of treatment options (25,26,31,32).

An omics analysis of breast cancer sequencing data from the Cancer Genome Atlas revealed that the mutational profile of basal-like breast cancers is variable within the subtype and compared to the other subtypes of breast cancer (33). The predominant genetic lesions in basal-like tumors are in the tumor suppressors *BRCA1* and *TP53* (33,34). Germline *BRCA1* mutations are present in 10% of basal-like tumors, compared to 1% in other subtypes (33). Epigenetic inactivation of *BRCA1* through promoter hypermethylation occurs in another 50% of basal-like tumors, compared to 50-28% in other subtypes (35). *TP53* mutations are present in 80% of basal-like tumors, compared to 12-29% of luminal tumors (33). The enrichment of *BRCA1*-inactivation in the basal-like subtype (36) is thought to be linked to the high prevalence of *TP53* mutations. *TP53* loss makes cells more resistant to apoptosis (37), and thus more tolerant of BRCA1 loss (38,39). Loss of two of the main coordinators of the DNA damage response leave cells susceptible to mutation, and contributes to the increased genomic instability associated with basal-like tumors (33). Besides *BRCA1* and *TP53*, no other genes are mutated in more than 10% of basal-like breast tumors, emphasizing the genetic heterogeneity within the subtype.

While sequencing studies have given a clearer picture of the genetic landscape of breast tumors, they have done little to uncover any druggable oncogenes for the basal-like subtype. More research is needed to discover genes and pathways that are not explicitly mutated, but required for maintenance of the tumorigenic state (40).

1.3 Reactive oxygen species (ROS)

Reactive oxygen species are chemically reactive species derived from the incomplete reduction of oxygen. ROS can be categorized into radicals, molecules with at least one unpaired electron, or non-radicals. Radicals, including the superoxide anion (O_2^-) and the hydroxyl radical ($HO\cdot$), are more reactive than non-radicals such as hydrogen peroxide (H_2O_2) (41). For most cell types, ROS production mainly occurs through mitochondrial oxidative phosphorylation. Inherent leakiness of the electron transport chain (ETC), specifically from complex I and complex III, causes some electrons to flow out of the pathway and partially reduce oxygen to the superoxide anion. From here, superoxide is rapidly converted to hydrogen peroxide by superoxide dismutase enzymes (42). H_2O_2 is a small, diffusible, and relatively stable form of ROS, making it particularly important for intracellular signaling (43). Other endogenous sources of ROS include the membrane-bound enzyme NADPH oxidase, which produces ROS in response to various ligands, along with other enzymes such as xanthine oxidase, cyclooxygenases, and nitric oxide synthase. To detoxify excess ROS, cells are equipped with antioxidants, including the thiols glutathione and thioredoxin, which are regulated by the transcription factor NRF2 (44,45). Tight regulation of ROS by antioxidant systems is necessary to balance the generation of ROS and to curtail oxidative damage to biomolecules.

An in-depth review of ROS production and its role as a signaling intermediate from a computational modeling perspective is provided in Chapter 2. In the next section, we discuss oxidative damage caused by ROS.

1.4 Damaging effects of ROS

ROS pose a problem to the cell because they readily react with biological molecules. The hydroxyl radical, the most powerful oxidant among the ROS (46), has strong affinity for electron-dense sites such as aromatic or sulfur-containing compounds (41). For example, cysteine residues in proteins are preferential targets because of their nucleophilic sulfhydryl group (43). Chemical modification of biomolecules alters the charge of regions of the molecule and can lead to structural changes that interfere with normal functioning. Oxidative stress occurs when there is an imbalance between the production of ROS and elimination by antioxidants, causing increased damage to DNA, lipids, and proteins.

Genotoxic stress refers specifically to DNA damage by endogenous or exogenous chemical agents. Most endogenous DNA damage results from ROS (47), which can react with nucleobases or the 2-deoxyribose moiety (48). Approximately 100 different oxidative lesions have been identified in DNA, most occurring at double bonds and methyl groups of base pairs (49). One of the most common oxidative DNA lesions results from the oxidation of guanine, generating 8-hydroxydeoxyguanosine (8-OHdG), which is a biomarker for oxidative stress and some types of cancer (50,51). If unrepaired, 8-OHdG can cause G-T or G-A transversion mutations during DNA replication (52). The genome is estimated to suffer as many as 10^3 oxidative lesions per day (53), which if unrepaired, can go on to cause heritable damage (54).

Due to the harmful effects of ROS, the cell is armed with multiple mechanisms to detoxify ROS and repair the damage they cause. The next two sections will cover two of the main pathways responsible for sensing and responding to ROS.

1.5 NRF2

1.5.1 The role of NRF2 in normal cells

Redox imbalance triggers the cellular detoxification system, a two-stage process of metabolism. Phase I involves oxidation of xenobiotics. Oxidation is carried out mainly by the cytochrome P450 superfamily of enzymes (55), which use oxygen and NADH as a cofactor to add a reactive group to the toxin. Phase II, involves the transfer of hydrophilic compounds to the now reactive xenobiotic, carried out by a variety of enzymes including sulfotransferases, glutathione transferase, amino acid transferases, N-acetyl transferases, and methyltransferases (56). Conjugation reactions decrease the reactivity of the toxin, minimizing harmful effects to other biomolecules.

NRF2 coordinates the detoxification system by activating transcription of various Phase I and II enzymes (44,57). It is a member of the cap ‘n’ collar subfamily of basic region leucine zipper transcription factors and regulates gene expression through the antioxidant response element, a 9 base pair promoter sequence resembling the NRF2 binding motif [TGA[C/G]T[C/T][A/G]GCA] (58–60). Under normal conditions, NRF2 is maintained at low basal levels by its repressor KEAP1, a substrate adaptor protein for a Cul3-dependent E3 ubiquitin ligase (61,62). KEAP1 binds two motifs within the N-terminal Neh2 domain of NRF2 to enable ubiquitin conjugation and proteasomal degradation (63). The higher affinity ETGE motif is necessary for KEAP1 binding and the lower affinity DLG motif is necessary for proper orientation to facilitate polyubiquitination of lysine residues between the two motifs (64–66). Under conditions of electrophilic or oxidative stress, several cysteine residues of KEAP1 are modified causing a decrease in the affinity of KEAP1 for the Neh2 domain (67–69). The nature of the stress determines which cysteine residues are modified. Electrophilic compounds such as sulforaphane (SF) react with any of the three sensor cysteines Cys151/Cys273/Cys288 (70), whereas the oxidative stress-inducer hydrogen peroxide (H_2O_2) reacts with

Cys226/Cys613/Cys622/Cys624 (71). SF, a potent electrophile derived from cruciferous vegetables, reacts with KEAP1 cysteines through its sulfur-containing isothiocyanate group to form thionoacyl adducts (72,73). These modifications alter KEAP1 conformation and impair association with both Cul3 and NRF2 (63,74).

Once NRF2 is stabilized, it translocates to the nucleus, heterodimerizes with small Maf proteins (75) and binds to AREs to induce expression of cytoprotective genes (44,76,77). NRF2-induced genes mediate the antioxidant response by several mechanisms including drug metabolism, synthesis of reducing factors, regeneration of oxidized cofactors and proteins, synthesis of antioxidants, and iron sequestration (Table 1.1).

Table 1.1 The NRF2-regulated antioxidant system.

Category	Gene	Name/Function
ROS and xenobiotic detoxification	*CYP2A6* (78)	Cytochrome P450
	ALDH3B1 (79)	Aldehyde dehydrogenase
	NQO1 (80)	Quinone detoxification
NADPH production	*G6PD* (81)	Glucose-6-phosphate dehydrogenase
	PGD (81)	6-phosphogluconate dehydrogenase
	ME1 (45)	Malic enzyme
	IDH1 (81)	Isocitrate dehydrogenase
Glutathione antioxidant system	*GCLC* (82,83)	Glutathione synthesis
	GCLM (82,83)	Glutathione synthesis
	GPX2 (84)	Glutathione peroxidase
	GSTA1, GSTA2, GSTA3 (76)	Glutathione S-transferase
	GSTM1, GSTM2, GSTM3 (76)	Glutathione S-transferase
	GSR (85)	Glutathione reductase
	SLC7A11 (86)	Cysteine/glutamate transporter
Thioredoxin antioxidant system	*TXN* (87)	Thioredoxin
	TXNRD1 (45)	Thioredoxin reductase
	PRDX1 (88)	Peroxiredoxin
Heme and iron metabolism	*HMOX1* (89)	Heme oxygenase
	FTL (45)	Detoxifies Fe(II)
	FTH (45)	Detoxifies Fe(II)

1.5.2 NRF2 and cancer

ROS and antioxidants have a complex role in cancer development and progression. ROS can damage DNA, which increases mutation rate and promotes oncogenic transformation of cells (47). This fact has motivated antioxidant treatment for the prevention and therapy of cancer (90). However, cancer cells are also known to produce more ROS than normal cells (12) due to oncogenic signaling, increased metabolic activity, and mitochondrial dysfunction (91). Increased ROS generation leads to higher amounts of oxidative stress, which can cause apoptosis and senescence (92,93). These findings have motivated using ROS inducers or antioxidant inhibitors to promote ROS-induced apoptosis of cancer cells (94–96). Thus, as the main regulator of the antioxidant response, NRF2's role in cancer is not straightforward.

In some cancers, excessive ROS levels cause activation of the NRF2 pathway to counteract the toxic side effects of chronic oxidative stress (97). In lung cancer, activating mutations in the NRF2 pathway are common. Biallelic inactivation of NRF2's negative regulator KEAP1 occurs in up to 25% of non-small cell cancers (NSCLCs) (98), and activating mutations in NRF2 are found in 10% of tumors (99). Alternatively, NRF2 pathway activation can result from oncogenic KRAS, a mutation found in 20-30% of NSCLCs that activates NRF2 transcription through a TPA response element in the promoter region (100). Constitutive activation of NRF2-mediated gene expression confers a high antioxidant capacity to lung cancer cells, increasing survival and proliferation in the presence of high levels of oxidants and chemotherapies (101–104). However even within lung cancer, NRF2's effects can vary based on stage of tumor development. Using genetic knockout models, studies have shown that Nrf2-deficient mice are more susceptible to mutagen-induced lung carcinogenesis, but develop less proliferative tumors than wild-type mice (105,106), emphasizing NRF2's context-dependent role in cancer.

Compared to lung cancer in which NRF2 is a bona fide oncogene, less is known about NRF2's role in breast cancer. NRF2 is not mutated in breast cancers (98), but has been linked to important breast cancer oncogenes and tumor suppressors. These interactions promote various cancer cell phenotypes, including metabolic reprogramming (81), chromosomal instability (107), and oxidative stress. Activating mutations in breast cancer oncogene *PIK3CA*, occurring in 20% of breast cancers (98), activate the NRF2 pathway to support cancer cell proliferation and survival (81,108). Loss of function mutation of the tumor suppressor *BRCA1*, found in 5-10% of breast cancers (109), downregulates NRF2 expression leading to increased ROS levels (108,110). Higher ROS levels together with loss of DNA repair increase genomic instability and mutational load in BRCA1-mutated breast tumors (111). Missense mutants of the tumor suppressor p53 can bind NRF2 to activate a pro-tumorigenic proteasome gene program in breast cancer cells (112).

Due to the numerous examples of oncogenes and tumor suppressors leveraging wild-type NRF2 to promote cancer cell phenotypes, NRF2 must be studied in the context of its interacting partners to delineate its role in cancer.

1.6 p53

1.6.1 The role of p53 in normal cells

p53 is a transcription factor activated by a variety of cell-physiologic stresses including DNA damage, hypoxia, oncogene activation, ribosomal stress, and oxidative stress (113). p53 consists of a N-terminal transcriptional activation domain, a central DNA-binding domain, and a C-terminal tetramerization domain (114). In its active state, p53 exists as a tetramer (115,116) and binds to a consensus sequence consisting of two copies of the decamer [A/G][A/G][A/G]C[A/T][A/T]G[C/T][C/T][C/T] separated by up to 13 base pairs (117). p53 controls the expression of hundreds of genes that are involved in many different protective functions (118–120), a subset of which are listed in Table 1.2. p53's control over cell cycle arrest, DNA damage repair, and induction of apoptosis make it one of the most important tumor suppressor genes.

Due to the diversity of functions covered by p53 target genes (Table 1.2), the choice of which genes become activated in response to a stressor is important. The temporal dynamics of p53 signaling is one factor that determines target gene activation and cell fate (121,122). Certain stresses, such as ionizing radiation, cause pulses in p53 abundance, which induce genes involved in cell cycle arrest and DNA repair (123). In contrast, sustained p53 signaling activates genes involved in apoptosis and senescence. Concentration of p53 is another cue cells use to differentiate between severity of damage and decide which genes to activate. In response to high concentrations of H_2O_2, p53 activates its pro-oxidant gene targets, *TP53I3* and *BBC3*, leading to apoptosis. Lower concentrations of H_2O_2 induce low levels of p53 and activation of antioxidant gene targets *SESN2*, *SESN1*, and *GPX1* (124). In general, the choice between repair of damage and apoptosis depends on the type and severity of stress, the cell type, and the presence of other pro- and anti-apoptotic signals in the cell.

Under normal conditions, p53 is maintained at low basal levels by its negative regulator *MDM2*, an E3 ubiquitin ligase that targets it for degradation (125). Under conditions of genotoxic or oxidative stress, upstream kinases ATM and Chk2 phosphorylate p53, disrupting MDM2-p53 binding and allowing p53 to accumulate and activate target genes (126–128). *MDM2* itself is a p53 target gene, creating a negative feedback loop that controls p53 abundance after activation. In addition, p53 target gene *PPM1D* dephosphorylates upstream kinases ATM and Chk2, creating another negative feedback loop (129). These and other feedback loops ensure that p53 molecules are degraded soon after their synthesis to avoid inappropriately shutting down cell proliferation or inducing apoptosis in transiently perturbed cells.

Table 1.2 Examples of p53 target genes according to function.

Category	Gene	Name/Function
DNA damage repair	*DDB2* (130)	DNA damage-binding protein 2
	XPC (131)	DNA damage recognition and repair factor
	PCNA (132)	Proliferating cell nuclear antigen
Antioxidant	*PA26* (133)	Sestrin 1
	HI95 (124)	Hypoxia-induced gene 95 (Sestrin 2)
	GPX (134)	Glutathion peroxidase
	SOD2 (135)	Superoxide dismutase 2

Cell cycle control	*CDKN1A* (136)	Cyclin-dependent kinase inhibitor 1 (p21)
	GADD45A (137)	Growth arrest and DNA damage inducible alpha
	CCNG1 (138)	Cyclin G1
Apoptosis	*BAX* (139)	Bcl-2-associated X
	BID (140)	BH3-interacting domain death agonist
	Noxa (141)	Bcl-2 family protein
	PUMA (142)	p53 upregulated modulator of apoptosis
	FAS (143)	Fas cell surface death receptor
	CASP6 (144)	Caspase-6
Metabolism	*TIGAR* (145)	*TP53*-induced glycolysis and apoptosis regulator
	ALDH1A3 (146)	Aldehyde dehydrogenase family 1 member A3
Post-translational regulators of p53	*MDM2* (147,148)	Mouse double minute 2 (negative regulator of p53)
	PPM1D (149)	Protein phosphatase 1D

1.6.2 p53 and cancer

Inactivation of p53 is a common strategy used by cancer cells to avoid apoptosis and a prerequisite for the development of many cancers. The most common method of inactivation is mutation of the *TP53* gene, which occurs in over half of all cancers (150,151). Unlike other tumor suppressors, which are typically inactivated by deletions or truncating mutations, the majority of *TP53* mutations are missense mutations that result in a full-length, non-functional protein (152,153). This is important because most full-length *TP53* missense mutants can still form tetrameric complexes with copies of wild-type p53 remaining in the cell (154). Hetero-tetramers lack some or all of the transcriptional activity of wild-type p53, causing a potent dominant-negative effect (155). Since p53 mutants cannot activate transcription of genes, the p53-MDM2 negative feedback loop is no longer engaged and mutant p53 accumulates to high levels.

Many p53 mutants not only lose tumor-suppressive function and acquire dominant-negative activity, but also exhibit oncogenic properties that are independent of wild-type p53.

Gain of function (GOF) p53 mutants can bind and activate genes with tumor-promoting functions including multidrug resistance gene (156), MYC (157), EGFR (158), IGF2 (159), and many others in a mutant-specific manner (160). Numerous mutants with GOF properties have been identified, including hotspot mutations R280K, R273H, and R248Q (161). GOF p53 mutants have also been found to cooperate with other transcription factors to regulate a diverse set of genetic programs (162–164). In fact, GOF p53 mutants have been found to interact with or regulate the NRF2 pathway. One study found that multiple p53 GOF mutants, but not wild-type p53, bind to NRF2 to activate proteasome gene transcription in triple-negative breast cancer cells, resulting in resistance to chemotherapeutics (112). p53 GOF mutants have also been found to attenuate the expression of NRF2 antioxidant genes in response to oxidative stress (112,165).

While there are several links between NRF2 and mutated p53, in this dissertation we examine NRF2's regulation in coordination with wild-type p53 during key transitions in the progression of breast cancer.

1.7 Dissertation preview

In this dissertation we present a systems analysis of the stress-activated transcription factor NRF2 during normal mammary gland development, premalignancy, and invasive triple-negative breast cancer. We use image processing, molecular and cellular biology techniques, and computational modeling to decipher the broader NRF2 network responsible for oxidative stress handling. This systems-level approach uncovers a stress responsive network in which NRF2 is activated together with the tumor suppressor p53 in single cells in response to oxidative stress in normal breast epithelial cells and hormone-negative premalignancies. This work is detailed in the manuscript, Sporadic activation of an oxidative stress-dependent NRF2–p53 signaling network in breast epithelial spheroids and premalignancies (166), which is accepted pending minor revisions at *Science Signaling.* The work in the manuscript has been divided and rearranged for clarity in Chapter 4 and 5 of this dissertation.

This introduction chapter included a brief overview of ROS and the oxidative damage they inflict on a cell. Chapter 2 presents an in-depth review of ROS production and modulation of signaling pathways from a computational modeling perspective. The review provides detail on ROS' role as a signal transducer and takes inventory of existing computational models of ROS, helping contextualize the mechanistic model of oxidative stress handling presented in Chapter 5. This work was published in *Frontiers in Pharmacology* in November 2016 with me as first author (167).

Early on in my thesis I used image processing techniques to analyze the spatial association of two proteins in triple-negative breast cancer tissue. This work led to a coauthored publication and laid the technical groundwork for computational image analyses presented later in this dissertation (Chapter 4). Chapter 3 describes the coauthored work and additional image processing work on cancer tissue I completed during an internship at digital pathology startup company Proscia. This internship was sponsored by BME's Going Pro program and served as one of my Educational Elective Experiences.

In Chapter 4, we describe the experimental work which uncovered NRF2–p53 coordination in response to oxidative stress in breast epithelial cells and how coordination is altered along the progression to invasive triple-negative breast cancer. In Chapter 5, we use computational modeling to further characterize the NRF2–p53 network and predict oxidative stress tolerance in triple-negative breast cancer cell lines. In Chapter 6, we conclude with future applications of this work, focusing on areas where the NRF2–p53 computational model could provide valuable insight.

Together, this research discovers a novel stress-induced coupling between NRF2 and p53 in a wild-type setting. This coordination is important for normal glandular morphogenesis and maintenance, but could provide a redundancy that makes cells more tolerant to p53 mutation. Combining experimental and computational approaches, we developed a systems model of NRF2–p53 signaling with both explanatory and predictive power. More broadly, this dissertation demonstrates the power of using multidisciplinary approaches to holistically understand signaling networks, which can have important context-specific behavior.

Chapter 2 Computational Models of Reactive Oxygen Species as Metabolic Byproducts and Signal-Transduction Modulators

2.1 Abstract

Reactive oxygen species (ROS) are widely involved in intracellular signaling and human pathologies, but their precise roles have been difficult to enumerate and integrate holistically. The context- and dose-dependent intracellular effects of ROS can lead to contradictory experimental results and confounded interpretations. For example, lower levels of ROS promote cell signaling and proliferation, whereas abundant ROS cause overwhelming damage to biomolecules and cellular apoptosis or senescence. These complexities raise the question of whether the many facets of ROS biology can be joined under a common mechanistic framework using computational modeling. Here, we take inventory of some current models for ROS production or ROS regulation of signaling pathways. Several models captured non-intuitive observations or made predictions that were later verified by experiment. There remains a need for systems-level analyses that jointly incorporate ROS production, handling, and modulation of multiple signal-transduction cascades.

2.2 Introduction

Reactive oxygen species (ROS) play a complex role in cellular biology. Initially viewed merely as harmful byproducts of metabolism, ROS are now known to serve additional functions as intracellular regulators of various signaling pathways. At low levels, ROS function as a reactive second messenger mainly by reversible oxidation of key amino acids of target proteins. High ROS levels, by contrast, cause damage to various biomolecules (lipids, proteins, and DNA) and have been linked to pathologies including neurodegeneration (168,169), atherosclerosis (170,171), and renal disease (172,173). ROS play an especially complex role in cancer, with various oncogenes and tumor suppressors influencing, and influenced by, the redox environment of the cell (174,175).

It is challenging to study experimentally how endogenous and exogenous sources of ROS are handled by the cell. In addition, the context- and dose-dependent intracellular consequences of ROS can result in confounding observations. ROS has been found to stimulate proliferation in some cell types under certain experimental conditions (176,177) and inhibit proliferation (178) or induce apoptosis (179) in others. Such contextual and experimental complexities make it difficult to understand ROS holistically by experimentation alone.

Computational modeling approaches can tackle this problem by simulating the concurrent dynamics of many variables, including those that are difficult to access experimentally (180). In this chapter, we cover the handful of models described thus far for ROS production and ROS regulation of signaling pathways (Figure 2.1). We start with experimental and computational approaches to measure ROS production. We next focus on models that simulate ROS production by the mitochondria, the predominant intracellular source of ROS, and by membrane-bound enzymes, which link extracellular signaling to intracellular ROS production. We also discuss models that simulate ROS regulation of various signaling pathways, giving a broader view of the influence ROS have on intracellular signaling. Finally, we discuss the need for a systems-level analysis of ROS signaling to provide a generalizable framework that accounts for the many downstream cellular effects of ROS.

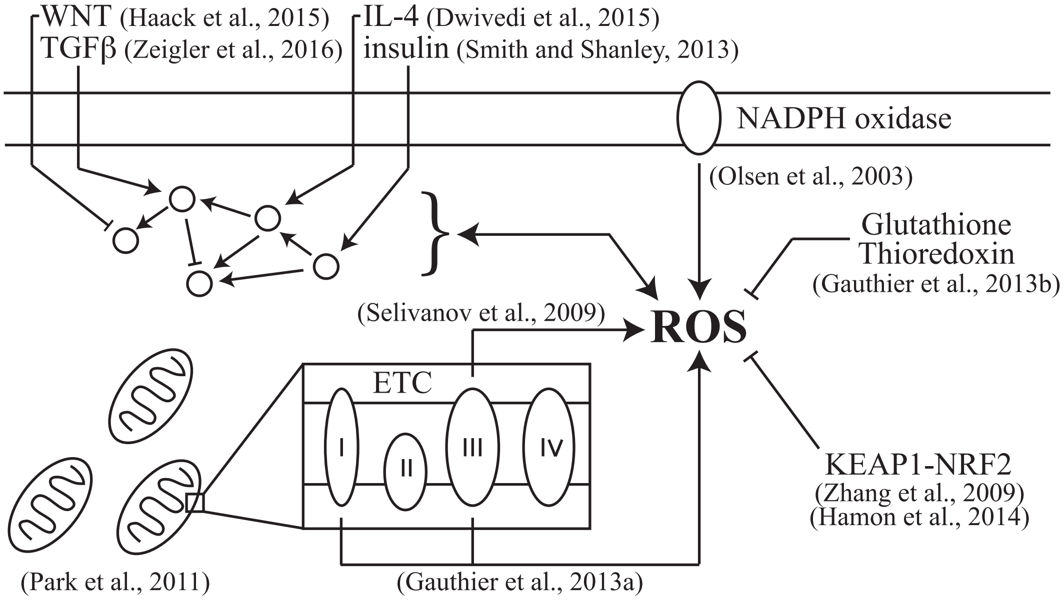

Figure 2.1 Computational models of reactive oxygen species (ROS) production and signal-transduction modulation.

2.3 Challenges of Measuring ROS

Reactive oxygen species are difficult to measure reliably within cells. For example, early measurements of cellular oxidative state used dyes such as 2′,7′-dichlorofluorescin (DCFH) which were later shown to create additional radical species (181). The secondary reactions and instability of the dye made long-term imaging with DCFH impossible. To address these deficiencies, researchers engineered fluorescent reporter proteins such as HyPer, RoGFP, and RxYFP (182–184), which undergo redox-sensitive conformational changes that elicit a change in fluorescence. Genetically encoded fluorescent proteins enable live-cell imaging and are further capable of localizing ROS production to specific sub-cellular compartments (185,186). Nevertheless, these sensors might miss low concentrations of H_2O_2 due to the endogenous enzyme peroxiredoxin, which is ~100-fold more active toward H_2O_2 compared to introduced probes (187).

Given these challenges, some groups have taken a more computational approach to calculating the kinetics associated with H_2O_2 (188). Lim et al. built a reaction-diffusion model to study localization of H_2O_2, which is important for control and specificity of redox signaling. They incorporated cytoplasmic diffusion into their reduced kinetic model of H_2O_2 clearance, in which peroxiredoxin is the dominant scavenging molecule (189). Using modeled concentration profiles obtained after bolus addition of H_2O_2 to the extracellular medium, the authors determined order-of-magnitude estimates for intracellular H_2O_2 diffusion through the cytosol, with a length scale of 4 μm and a time scale of 1 ms (190). The short length scale and rapid time scale indicate that H_2O_2 degradation and signaling are localized to the area where H_2O_2 is produced, contradicting the common modeling assumption of a well-mixed cytoplasm. This finding could explain discrepancies observed between bolus addition versus steady intracellular generation of H_2O_2 (191,192). Rapid H_2O_2 scavenging also has implications for intracellular signaling, as H_2O_2 reactivity is limited to molecules in the subcellular vicinity.

2.4 Computational models of ROS production

2.4.1 ROS Production By Complex III of the ETC

Physiologically, ROS production increases under hypoxic conditions. Hypoxia causes a decrease in the maximum reaction rate of complex IV, which is thought to cause excess electron leakage from other components of the ETC, such as complex III (193). After a return to normoxic conditions, ROS remain at higher hypoxic levels. The stable switch in ROS production is relevant during organ transplantation and other surgeries requiring an ischemic period. To better understand the mechanism behind this bistability, Selivanov et al. (194) modeled the Q cycle mechanism of Complex III in the mitochondrial respiratory chain as the primary mechanism of ROS generation. Complex III can take on as many as 400 redox states due to its binding to quinones. The authors elaborated a system of differential equations describing the evolution of all of the redox states of Complex III. Model simulations predicted that Complex III can exist in two different steady states, a low ROS-producing state and a high ROS-producing state. This bistability is dependent upon the initial conditions of the system, specifically the redox state as predicted by levels of semiquinone and free ubiquinol. If starting in a highly reduced state, the overall system remains reduced, whereas if it starts in a less reduced state, Complex III progresses to a steady state with low semiquinone concentration and thus low ROS production. The overall system evolves to the high ROS producing state either by an increase in succinate concentration, causing the reduction of ubiquinone to ubiquinol, or a decrease in oxygen content. Once switched to this high ROS-producing state, Complex III persists in that state even after a return to lower succinate concentration or normoxic conditions. The sustained increase in ROS production provides a mechanism that may contribute to reperfusion injury after ischemia.

The model predictions were experimentally validated in isolated rat brain mitochondria incubated with succinate with or without the addition of ADP. The addition of ADP, and subsequent synthesis of ATP, switches mitochondria to a low ROS-producing state and thereby lowers mitochondrial membrane potential. Once all the ADP is consumed, membrane potential increases to pre-ADP levels, but ROS production remains at the lower initial level. These results agree with model predictions that two levels of ROS production could coexist under the same set of parameters and give rise to metabolic heterogeneity in an isogenic population of cells.

2.4.2 ROS Production By Complexes I and III of the ETC

Reactive oxygen species are also produced by Complex I of the ETC. Gauthier et al. (195) built a computational model of the ETC focusing on ROS production by both complex I and III (Figure 2.1). Simulations were used to study the control of ROS production in cardiac myocytes under different metabolic conditions. The model is composed of non-linear ordinary differential equations describing the oxidation states of the various forms of ubiquinone, produced by complex I electron transfer, and the three subunits of complex III: cytochrome b, cytochrome c1, and the iron sulfur protein. The authors investigated how mitochondrial membrane potential, matrix pH, and ROS scavenging affect ROS production and control. When membrane potential increased 20 mV higher than unstressed cells to above ~150 mV (196), the model predicted that complex III ROS production as a function of membrane potential switches from zeroth order (constant production) to first order (exponential production). Increased membrane potential leads to a reduction in the Q cycle reaction rate, or conversion of ubiquinol to ubiquinone, causing a substantial increase in ROS production rate.

The model predictions agree with experimental results reporting a threshold membrane potential of 153 mV, above which ROS production increases dramatically (197). When simulating an increase in mitochondrial matrix pH, the model predicted that ROS production from complexes I and III increases during forward electron transport. This pH-dependent mechanism of ROS generation was experimentally observed by Selivanov et al. (198) who found that an increase in pH from 6 to 7 caused a threefold increase in ROS production rate.

During reverse electron transport, where electrons flow toward complex I in the presence of a weak reducing agent, complex I ROS production also increased with matrix alkalinization. The model therefore correctly predicted the dependence of ROS production on both mitochondrial membrane potential and matrix pH.

ROS levels are governed not only by production, but also by clearance through scavenging mechanisms. To gain a more complete picture of ROS dynamics, Gauthier et al. added glutathione and thioredoxin-mediated ROS scavenging mechanisms to the model (199). ROS production decreased to a minimum level as the mitochondrial environment became more oxidized and then rose again as the scavenging systems became depleted. This result agrees with the redox-optimized ROS balance hypothesis (199), which states that ROS levels are lowest at an intermediate mitochondrial redox potential. Together, the authors' minimal model of ROS regulation produced results that matched many independent experiments describing different regimes of ROS production, providing support for the hypothesis that the cellular redox state influences the rate of ROS production.

Applying their model, Gauthier went on to investigate ROS production and scavenging in the context of heart failure (200). Integrating the ETC-ROS model discussed above into a mitochondrial energetic-redox model (201) allowed the authors to test the hypothesis that mitochondrial Ca2+ mismanagement leads to high levels of ROS during heart failure. In agreement with this hypothesis, their model showed that under conditions of mismanaged mitochondrial Ca2+, NADH levels decrease drastically under simulated cardiac pacing, highlighting the link between compromised Ca2+ and NADH regulation. Lower amounts of NADH lead to lower NADPH levels and a decreased ability to reduce scavenging enzymes for reuse, causing ROS to accumulate. ROS levels in mitochondria increase under increased load (202), but surprisingly the model predicted that ROS production actually decreases under these conditions. The net increase in ROS abundance stems from an even-further reduction in ROS scavenging, which causes ROS accumulation in the cell. Therefore, in the setting of heart failure, preservation or restoration of scavenging enzymes may prove more effective than efforts to block ROS production (203).

In another model of ROS production by ETC complexes I and III, Bazil et al. (204) described ROS generation by oxidative phosphorylation coupled to ATP demand. They updated an existing kinetic model of oxidative phosphorylation (205) to include ROS generation by complexes I and III and first-order scavenging by superoxide dismutase and peroxidase. Model simulations agreed with previous findings that free radical production by complex III is higher than complex I production under physiological conditions (195). As ATP demand increases, the steady state production of ROS also increases, in line with experimental observations (206). The authors further applied their model to study reverse electron transport that is seen during reperfusion. Simulating ischemia/reperfusion led to bistability in ROS production (194,207) only when the activity of complex II was increased. Complex II activity requires electrons to be supplied to the quinone pool by the dehydrogenation of succinate to fumarate. The predicted importance of complex II agrees with work by Chouchani et al. (208) showing that succinate is a main driver of mitochondrial ROS production upon reperfusion (208). Therefore, complex II inhibition during reperfusion could prove useful to decrease ROS production and reperfusion injury (209).

2.4.3 ROS Production By the Mitochondrial Network

In a phenomenon known as ROS-Induced ROS Release (RIRR), damaged mitochondria produce an increased amount of ROS, which causes surrounding mitochondria to increase ROS production through a positive-feedback loop. Park et al. (210) used an agent-based model describing inter-mitochondrial signaling to study the role of mitochondrial network dynamics in mitochondria-driven ROS production (Figure 2.1). Simulations were performed with three different mitochondrial networks: uniformly distributed mitochondria, as seen in cardiomyocytes; irregularly distributed mitochondria, as in neurons; and sparsely distributed mitochondria, as found in white blood cells (211). The simulations introduced hydrogen peroxide as an initial oxidative stress, causing mitochondria in the surrounding area to produce more ROS. Mitochondrial ROS diffuse stochastically by random walk in 2D space, amplifying the local ROS response. Depending on the initial oxidative stress insult and the mitochondrial network dynamics, ROS production is blocked by antioxidant enzyme systems or becomes amplified by RIRR, which propagates ROS through the entire cell. The goal of the model was to predict the percent reactive mitochondria resulting from an initial oxidative stress input and the initial hydrogen peroxide concentration that causes RIRR.

The model indicated that ROS propagation is faster in the cardiomyocyte model than in the irregular distribution model, as shown by a higher dose dependence of reactive mitochondria as a function of initial oxidative stress. In addition to mitochondrial distribution, the model predicted that the density of mitochondria affects the response to oxidative stress inputs. Cells with a low density of mitochondria have considerable ROS propagation after low levels of oxidative stress, while cells with a high density of mitochondria only show strong ROS propagation after high levels of oxidative stress. The authors hypothesized that these differing responses to oxidative stress are due to differences in ROS signal transduction between mitochondrial networks. They further simulated the addition of different antioxidants to find that superoxide-scavenging antioxidants block ROS propagation more effectively in the cardiomyocyte model, while antioxidants that detoxify hydrogen peroxide are more effective in the irregular-distribution and low-density models of mitochondria. These results suggest that mitochondrial network configuration influences which molecular species is used to propagate ROS in the cell.

2.4.4 ROS Production in Relation to Antioxidant Signaling

Cyclosporin A (CsA) is an immunosuppressant, which indirectly causes oxidative stress (212) and adaptively activates the NRF2 pathway in the kidney. Hamon et al. (213) fused an in vitro pharmacokinetic model (214) of CsA distribution in cultured renal epithelial cells with a dynamical model of NRF2 signaling originally designed to capture the cellular response to xenobiotics (215). The authors adapted the NRF2 model to accommodate ROS as a state variable generated in proportion to cytosolic CsA (213). In the revised model, ROS are detoxified by glutathione peroxidase and further act as an oxidant and inhibitor of KEAP1, which degrades NRF2. Last, CsA was forbidden from interacting with the aryl hydrocarbon receptor as xenobiotics do in the original model, because experimental data was lacking for such an interaction. To parameterize the fused model, Bayesian inference was used together with transcriptomic, proteomic, and metabolomic data collected from cells treated with different concentrations of CsA dosed daily for 2 weeks. The model predicted that low doses of CsA yielded widespread oscillations throughout the network as cells metabolized the administered CsA and detoxified ROS before the next administration. At high doses, however, the cell is overwhelmed and the modeled network locks into an elevated state of ROS adaptation. These predictions were not followed up experimentally, but the work of Hamon et al. (213) nonetheless illustrates how toxicologic models can be repurposed for ROS specifically.

2.4.5 ROS Production in the Phagosome Membrane By NADPH Oxidase

Aside from the ETC, ROS also play a key role in pathogen clearance. Neutrophils utilize ROS to attack bacteria engulfed within a phagosome. The source of this ROS burst is not from mitochondrial respiration but from the NADPH oxidase complex at the plasma membrane (216) (Figure 2.1). Levels of ROS oscillate in the neutrophil (217), however, the mechanism behind these oscillations was unclear. Olsen et al. (218) proposed that the oscillations arose from interactions among myeloperoxidase, melatonin, NADPH, and NADPH oxidase. To explore the oscillatory behavior, they built a two-compartment, differential equation model of the phagosome and the cytoplasm (218). Without NADPH oxidase activity, model simulations exclusively produced damped oscillations that converged to a steady-state; by contrast, addition of NADPH oxidase elicited sustained oscillations similar to those reported experimentally (219). The authors triggered ROS oscillations in neutrophils with the activating chemotactic peptide FMLP and showed that pre-incubation with an inhibitor of NADPH oxidase blocked oscillations. Their model further predicted that melatonin would change the amplitude of the ROS oscillations measured. Pre-incubation of FMLP-activated neutrophils with melatonin confirmed the predicted increases in ROS amplitude. Computational and experimental modeling of NADPH oxidase in this setting allowed the authors to understand the basis of melatonin “priming” previously observed in neutrophils (220), underlining the power of pairing *in silico* and *in vitro* experiments.

2.5 Computational models of ROS as signal transduction modulators

2.5.1 ROS Production During WNT/β-Catenin Signaling

Reactive oxygen species are also generated as a secondary byproduct of multiple signal transduction cascades (221,222). Haack et al. (223) built a model of the WNT/β-catenin signaling pathway that included membrane-related processes as well as ROS signaling. The authors sought to explain experimental results showing that disruption of membrane lipid rafts inhibits WNT/β-catenin signaling, and also that ROS activate WNT signaling in the context of differentiation of human neural progenitor cells (224,225). The three-compartment model is based on mass-action kinetics and includes: a membrane model, in which WNT binds to receptor LRP6 causing its phosphorylation within lipid rafts; an intracellular model, in which AXIN binds phosphorylated LRP6 to prevent degradation of β-catenin; and a redox model, in which ROS increase the concentration of DVL-bound AXIN, making AXIN unable to degrade β-catenin. Simulations were initiated with a burst of ROS that was shown experimentally to coincide with the beginning of neural progenitor differentiation induced by growth-factor withdrawal. The model predicted an immediate, transient β-catenin stabilization resulting from redox-dependent DVL/AXIN binding, followed by a sustained β-catenin response arising from lipid raft-dependent canonical WNT signaling. The immediate β-catenin accumulation was observed experimentally by the authors in lipid raft-deficient cells that maintained a transient β-catenin response. By including ROS signaling, the extended WNT/β-catenin signaling model correctly captured experimental β-catenin nuclear dynamics during early neuronal differentiation.

2.5.2 ROS Modulation of IL-4 Signaling

Dwivedi et al. (226) looked at modulation of cell signaling by ROS in another setting, using the IL-4 signaling pathway as a redox-regulated case study. The authors sought to identify the most important mechanisms of redox regulation in the IL-4 pathway, which is important for regulating the effector T-cell response. The activated IL-4 receptor complex upregulates ROS through NADPH oxidase (227) , which influences signal transduction that proceeds through JAKs and culminates in the phosphorylation of STAT6. To identify the combination of regulatory mechanisms that best recapitulated the dynamics of IL-4 induced STAT6 phosphorylation, the authors turned to Monte Carlo analysis of an IL-4 ordinary differential equation model. Phosphorylated STAT6 dynamics were best captured by a model that incorporated a protein tyrosine phosphatase whose activity and nucleocytoplasmic shuttling were ROS sensitive. ROS regulation of phosphatase activity and localization, along with other ROS-independent mechanisms, were included in the systems-level model of IL-4 signaling, with parameters fit to experimental data in IL-4-stimulated Jurkat cells. The model predicted diminished STAT6 phosphorylation following IL-4 stimulation and ROS inhibition, which was confirmed experimentally by NADPH oxidase inhibition of IL-4-stimulated cells. Transient oxidation of protein tyrosine phosphatases was also observed experimentally by oxidized protein tyrosine phosphatase immunoprecipitation of extracts from IL-4-stimulated Jurkat cells. The authors' systems-level model provides a framework for investigating additional modes of receptor-initiated oxidation not previously explored.

2.5.3 ROS Crosstalk with Insulin Signaling

Smith and Shanley (228) adapted an existing differential equation model of insulin signaling (229) to incorporate ROS and study the interplay between insulin signaling and oxidative stress (Figure 2.1). Insulin-stimulated ROS production was assumed to occur through activation of NADPH oxidase and is about fivefold higher than the background level of mitochondrially produced ROS (230). ROS deactivate the phosphatases PTEN and PTP, activate the kinases JNK and IKK, and are detoxified by cytoplasmic SOD2. This model was used to make predictions about ROS, FOXO, SOD2, and insulin receptor abundances over long time scales.

When hydrogen peroxide was added as an oxidant to the system with or without insulin stimulation, the model predicted surprisingly different responses. Hydrogen peroxide alone caused modest glucose uptake and insulin alone caused strong glucose uptake, but hydrogen peroxide and insulin stimulation together were antagonistic, causing only moderate glucose uptake. In the model, this dampening effect of oxidative stress occurs because hydrogen peroxide and insulin together activate protein kinases (e.g., JNK, IKK), which cause hyperphosphorylation of IRS1 and decrease its ability to form the IRS1-PI3K complex that stimulates glucose uptake. The model also predicted that the FOXO-mediated antioxidant response depends critically on the extent of oxidative stress. With low oxidative stress, the antioxidant enzyme SOD2 is upregulated by FOXO through a JNK-mediated mechanism, but SOD2 is downregulated at higher levels of stress through an IKK-mediated mechanism. Although simplified in its handling of ROS and antioxidant pathways, this integrated systems model captures some of the complexities of oxidative stress for an important metabolic pathway.

2.5.4 ROS Production As One Node in A Larger Network of Cardiac Fibroblast Signaling

The previously discussed models incorporated ROS into a single canonical signaling pathway, but the generation and handling of ROS pervades multiple pathways and can lead to counterintuitive cell outcomes (231). Zeigler et al. (232) incorporated ROS as part of a much larger signaling network to identify regulators of cardiac fibrosis. A cardiac fibroblast signaling network was designed to study drivers of fibrosis, which is implicated in many cardiac pathologies (233). The network was compiled from experimental data on 10 pathways that are known to be important in cardiac injury, such as the IL-1 and TGFβ pathways. The model was formed using a logic-based differential equation approach (234), whereby species are represented as differential equations with rates of change dictated by Hill functions and truth tables comprised of interacting biomolecules. ROS production is controlled by the activity of NADPH oxidase and feeds into the truth tables of JNK and ERK activation, linking ROS generation at the plasma membrane to downstream intracellular responses.

In the model, reducing ROS levels had far-reaching and context-dependent effects on the network. Under baseline conditions, reductions in ROS caused a decrease in matrix metalloproteinase 9 (MMP9), which is important for the breakdown of extracellular matrix. By contrast, in an environment with high TGFβ signaling, like in a myocardial infarction, reducing ROS led to an increase in MMP9 activity. Therefore, a therapeutic prediction of the model is that antioxidant treatment for fibrosis would be more beneficial in the high TGFβ environment of myocardial infarct.

2.6 Conclusion and Future Outlook

The computational models of ROS biology covered in this review largely focus on ROS handling within the cell or on ROS modulation of canonical signaling pathways. In the future, we anticipate more sophisticated models that combine ROS handling and signaling concurrently. A prime test bed for such an integrated approach would be the NF-κB pathway, which is activated by ROS (235) and is responsible for inducing scavenging enzymes such as SOD2 (236). Finn and Kemp (237) have assembled a provisional model of IKKβ S-glutathionylation in the setting of antioxidants and chemotherapy-induced ROS. The coupling of signaling, production, and scavenging could give rise to feedback networks that explain the variable oxidative stress observed in some settings among single cells in very similar microenvironments (231).

There is also a need to build multiscale models that place ROS in the broader context of developing tissues, tumors, and infections (238–240). The dynamics of proliferation and death impinge on metabolism and signal transduction, which culminate to impact the redox state of cells in the population. Crosstalk between these cellular pathways may require different classes of modeling than those implemented so far (241,242). Advances in measurement will likewise expand the scope of targets modified by ROS (243) and reveal the extent to which molecular crosstalk is underappreciated.

Integration of ROS signaling into larger networks may allow researchers to predict outcomes of drug treatments that affect ROS generation, which causes drug resistance in some cancer contexts (244,245). A deeper understanding of ROS network dynamics could generate combinatorial treatments that avoid neutralizing drug efficacy. In the broader human population, there are many polymorphisms that affect ROS generation and scavenging, such as $p22^{phox}$ C242T and SOD2 A16V (246,247). These variants may tune how ROS interacts with other signaling networks, contributing to heterogeneous patient responses during therapy.

ROS are a fact of life that cannot be ignored. Like a living cell, investigators must find ways to deal with ROS holistically and achieve our goals despite their presence. The tools for pharmacologic modulation of ROS are predominantly limited to antioxidants. Systems modeling of ROS may one day provide a venue for exploring more-precise interventions that account for the complex biological processes involved.

Chapter 3 Techniques and approaches for biological image processing

3.1 Introduction

Biological images contain a vast amount of information, only a fraction of which can be accessed by the human eye. Image processing can extract quantitative information from pixels, which can be used to quantify patterns noted manually, or even to discover non-linear, complex patterns present in large imaging datasets (248).

Two main tasks of image processing are image segmentation and image classification. Image segmentation is the process of partitioning a digital image into multiple regions or sets of pixels with similar attributes (249). Image classification is the process of classifying what appears in an image into one of a set of predefined classes (250). Image processing pipelines begin with segmentation to extract meaningful regions of an image for analysis. A variety of analysis techniques can follow depending on the type of image and purpose of the study.

In this chapter I discuss two image processing pipelines using different types of biological images. Both pipelines incorporate image segmentation with different downstream analyses. The first deals with multicolor immunofluorescent images and uses staining quantification to measure paracrine signaling in triple-negative breast cancer cells. This work was included in a co-authored publication in *Developmental Cell* (251) and is presented in this chapter with permission by and in accordance to the author rights stated by Elsevier Publishing. I also discuss a generalized approach to analyze immunofluorescent images, as these techniques are used heavily throughout this dissertation (Chapter 4). The second pipeline deals with whole slide images (WSIs) of hematoxylin and eosin (H&E) stained cancer tissue and uses deep learning algorithms for tissue classification. I discuss the steps of a deep learning pipeline including image preprocessing, model training, and model validation and a pipeline designed to classify a particular type of skin pathology, squamous acanthoma. This work was completed during a two-month internship at digital pathology company Proscia.

3.2 An image processing pipeline to quantify GDF11-ID2 association in TNBC tissue

3.2.1 Background

In “Tumor-suppressor inactivation of GDF11 occurs by precursor sequestration in triple-negative breast cancer”, Bajikar et. al identify a tumor-suppressive role for growth-differentiation factor 11 (GDF11) in triple-negative breast cancer. GDF11 promotes an epithelial, anti-invasive phenotype when triple negative breast cancer cells are grown as 3D breast epithelial cultures and intraductal xenografts. GDF11 function is lost in TNBC due to deficient protein maturation, an uncommon mechanism of tumor suppressor inactivation. Interestingly in clinical TNBC samples, residual pockets of mature GDF11 were observed by immunohistochemistry using an antibody (GDF11-1E6) specific to GDF11’s mature form (Figure 3.1C,E). Thus, the defect in GDF11 maturation in tumors was incomplete, with some cells still able to properly process GDF11 to its active form. GDF11-1E6 foci were almost never found in normal specimens or in adjacent noncancerous tissue, where GDF11 function is presumably unaltered (Figure 3.1A,E). However, a TNBC-like pattern was noted in ~40% of basal-like DCIS cases (Figure 3.1B,E), raising the possibility that a shift in GDF11 regulation might coincide with the premalignant-to-malignant transition.

To determine if sporadically matured GDF11 in TNBC tissue remained functional, I used image processing techniques to measure the association of GDF11 and its effector, inhibitor of differentiation 2 (ID2), in immunostained tissue. ID2 is a transcription factor that was found to be required for GDF11’s tumor-suppressor functions in multiple in vitro and in vivo experiments. If mature GDF11 was associated with elevated levels of ID2 it would support that GDF11 remains functional when sporadically matured in TNBC.

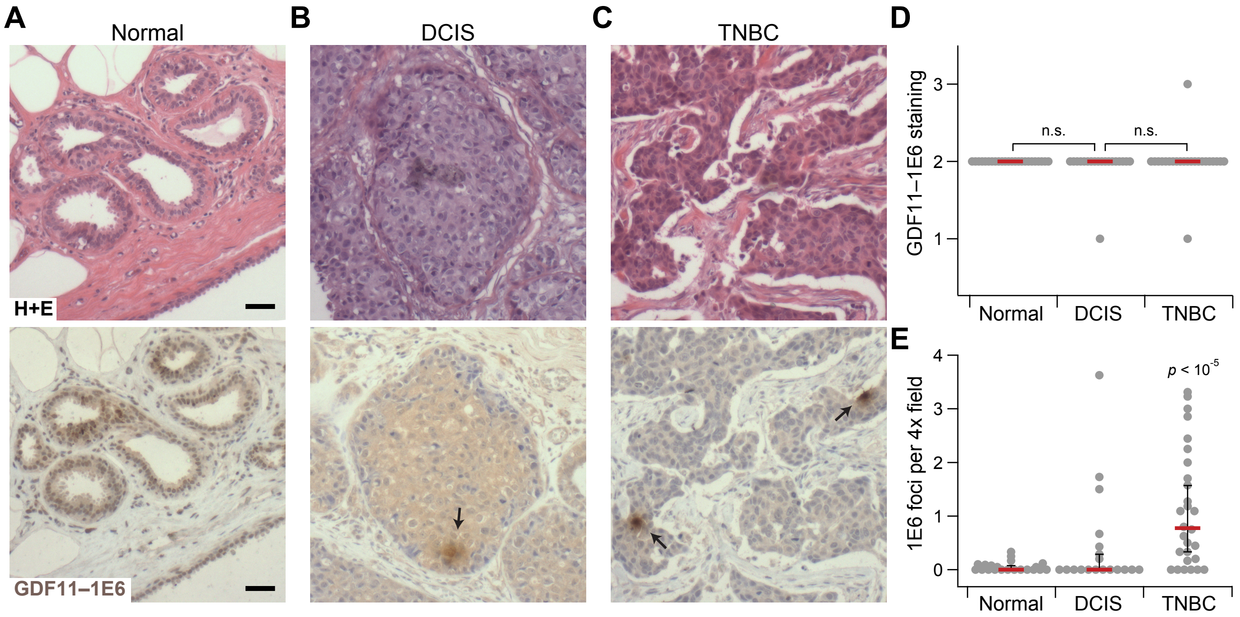

Figure 3.1 Maturation of GDF11 in TNBC progression.
(A-C) H&E staining and GDF11-1E6 immunohistochemistry for representative cases of normal breast tissue, ductal carcinoma *in situ* (DCIS) lesions, and TNBC specimens. GDF11-1E6 immunoreactive foci are indicated with pointed arrows. (D and E) Normal-DCIS-TNBC progression is not associated with altered overall GDF11-1E6 staining (D) but rather with the appearance of heterogeneous immunoreactive foci (E).

3.2.2 Design of an image processing pipeline to assess GDF11-ID2 association in TNBC tissue

To measure the association of focal GDF11 and ID2 staining, I developed a pipeline to acquire images of multicolor immunostained clinical tissue, locate GDF11 foci, and quantify ID2 intensity in regions adjacent to and outside of foci. First, TNBC clinical samples were immunostained for GDF11-1E6 and ID2 with DAPI as a nuclear counterstain. Fluorescent images were taken such that there was at least one example of GDF11-1E6 focal staining per image.

For image processing, the steps were as follows: 1) Locate regions of focal GDF11 staining, 2) expand outwards to define a local region around the focus, 3) quantify ID2 staining within the local region and 4) quantify ID2 staining outside of the focal region for comparison.

To find GDF11 foci, GDF11-1E6 channel grayscale images were segmented using Otsu's method of thresholding (Figure 3.2A,B). Thresholding is a means of image binarization in which every pixel above a certain threshold is classified as foreground and every pixel below the threshold value is classified as background. Otsu's method of thresholding iterates through all possible threshold values and chooses the value that minimizes the variance of the pixels in each class (249). Otsu's method worked well due to the roughly bimodal distribution of gray-tone values in GDF11-1E6 channel images, where the GDF11 foci had distinctly higher staining intensity compared to elsewhere in the image.

After thresholding, the binary image was filtered to exclude any objects classified as foreground that resulted from nonspecific binding of the antibody. Nonspecific staining presented as small, bright immunoreactive spots. Objects comprising less than 300 pixels were assumed to result from nonspecific binding and were excluded (Figure 3.2C). The mask now corresponding specifically to the GDF11 focus was dilated by a one-cell radius (Figure 3.2D) and the dilated mask was applied to the corresponding ID2 channel image to capture local ID2 staining around the GDF11 focus. For each image, a null distribution of ID2 staining intensity was created by randomly placing the dilated mask 1000 times outside of where the true focus was located. The ID2 immunoreactivity was quantified as the average ID2 fluorescence intensity within each mask.

Since all images were autoexposed to most accurately capture staining intensity, staining measurements were standardized before fusion across images. Nonparametric standardization was used as it is more robust to outliers (252) which are present in IF images from nonspecific antibody binding, photon noise arising from the emission and detection of light, and read noise arising from inaccuracies in quantifying numbers of detected photons (253). For each image, the ID2 immunoreactivity was standardized by subtracting the median ID2 fluorescence intensity of the randomly placed foci for that image and dividing by the associated interquartile range.

3.2.3 Mature GDF11 foci associate with elevated levels of GDF11 effector ID2 in TNBC

Once GDF11 foci has been isolated and ID2 staining quantified adjacent to and outside of foci, differences in ID2 fluorescence intensity could be statistically assessed. The distribution of ID2 fluorescence intensity around 46 foci (in 43 images) from 10 TNBCs was compared to 1000 random placements of the same mask outside of 1E6 foci on the same image by Kolmogorov-Smirnov test (Figure 3.3). GDF11–1E6 immunoreactive foci associated with significantly elevated ID2 immunoreactivity, supporting that TNBC-derived GDF11 remains bioactive when sporadically matured.

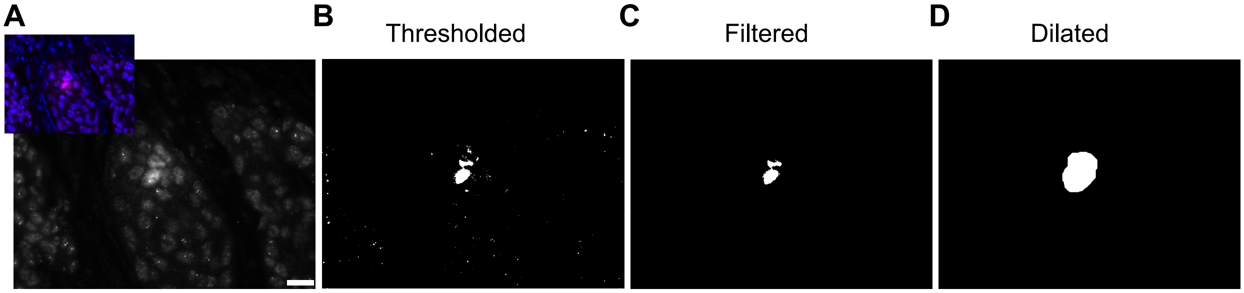

Figure 3.2 GDF11 foci identification and dilation.
(A) Raw GDF11-1E6 channel image. Merged (magenta) with DAPI nuclear counterstain (blue) in the upper left inset. Scale bar is 20 μm. (B) Binarized image after global Otsu thresholding with the graythresh MATLAB function. (C) Filtered image after removing objects with fewer than 300 pixels. White region is mask corresponding to GDF11-1E6 focus. (D) Mask dilated by a one-cell radius.

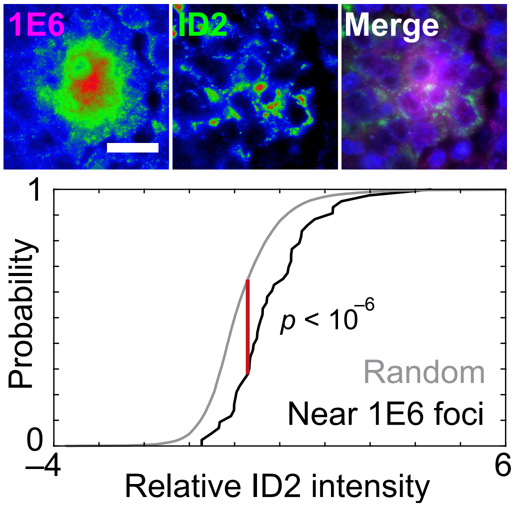

Figure 3.3 GDF11–1E6 immunoreactive foci associate with elevated ID2 immunoreactivity.
TNBCs were stained by immunofluorescence for GDF11-1E6 (magenta), ID2 (green), and DAPI as a nuclear counterstain (blue) (upper). Distribution of ID2 fluorescence intensity around 46 foci (in 43 images) from 10 TNBCs compared to 1000 random placements of the same mask outside of 1E6 foci on the same image (lower). Scale bar is 20 μm.

3.2.4 A generalized pipeline to quantify protein distribution patterns in IF images

The GDF11-ID2 processing pipeline was designed to study the association of two proteins in local regions of tissue. In this section I will discuss a generalized approach to analyze protein distribution and association in immunofluorescent images.

The first step of image processing is to isolate regions of interest (ROI) using image segmentation. Image segmentation strategies can be classified broadly into edge-based and region-based (249). Edge-based methods segment an image into objects based on edges detected by gray level discontinuities. Edge-based methods work best in images with good contrast between objects and background, including bright-field and differential interference contrast images (254,255). Region-based methods segment an image into various regions having similar characteristics and work well on fluorescent images (256). One of the simplest and most commonly used region-based techniques is thresholding, which segments an image based on a threshold intensity value. Thresholding is best for images in which the region of interest has different intensity properties than other areas of the image. Often, however, multiple segmentation techniques must be combined to isolate the desired region.

For single-cell analysis, objects can be easily isolated by thresholding a nuclear or cell membrane stain. To isolate other types of objects, such as foci of staining, a feature of the object that makes it visually distinct from the rest of the image must be leveraged to isolate it. In the example presented in this chapter, foci were isolated by thresholding on their concentrated, intense immunostaining pattern.

The next step is to define any secondary regions of interest for stain quantification. For example, if proximal neighboring cells are to be analyzed, the original ROI can be dilated by a fixed distance such as a one-cell radius to define a secondary ROI. If more distant neighbors are to be analyzed, the secondary ROI can be an annulus with inner and outer radii defined to capture cells within a desired distance.

Once ROIs are defined, staining is quantified within segmented objects using central tendency metrics such as the mean or median pixel value. If the original fluorescent images were taken at the same exposure, measurements can be combined across images for downstream analysis. If images were taken at different exposure times, measurements must be standardized so that pixels arising from different images have similar mean and variance to enable comparison (257). Standardization is achieved by subtracting a measure of central tendency (mean, median) and dividing by a measure of spread (variance, interquartile range).

Many segmentation pipelines can be created using the modules available in CellProfiler, an open-source software for cell image analysis (258). CellProfiler provides various methods of primary object identification and stain quantification in an easy-to-use graphical user interface. However, if a higher level of customization is required, pipelines can be created using MATLAB or another programming language. This can be useful if primary and secondary objects are not specifically defined by stains, as was the case in this chapter.

3.3 An image processing pipeline for tissue classification in digital histopathology slides

3.3.1 Background

Advancements in image digitization have made it possible to create high resolution images of entire glass pathology slides (259). Each image contains gigabytes of clinically relevant biological data, including complex morphometric features that are not visually discernable by the human eye. Automated image analysis is needed to extract quantitative data from these large, complex imaging datasets. Quantitative analysis of H&E-stained tissue features such as nuclear architecture and shape, epithelial morphology, and immune cell infiltration can aid in clinical diagnosis and tissue biomarker discovery (260–262).

Extracting and interpreting quantitative information from H&E images are challenging tasks that require algorithms that can learn and adapt to differences in tissue morphology across and within specimens. Machine learning algorithms have the flexibility required for these tasks due to their ability to learn from data without being explicitly programmed. For the purpose of this section, I will discuss deep learning, a subset of machine learning that has had much success in processing multidimensional imaging data (263,264).

Deep learning algorithms use layers of neural networks to learn high-level feature representations from data (265). A neural network consists of layers of neurons, or nodes, that perform transformations on input data (266). A neuron takes the weighted sum of inputs, adds a constant “bias” term and returns the output. Each layer of neurons processes information from the previous layer to learn increasingly complex features of an image. Features learned by deep learning algorithms are similar to those used in image segmentation algorithms described earlier in this chapter. For example, the learned features in the first layer of a model are usually basic, such as edges at a specific orientation in the image (265). Subsequent layers build in complexity, grouping similar features into motifs that are then detected as objects in final layers.

An important advantage of deep-learning algorithms is that they learn image features from the raw data without requiring manual feature engineering, making them adaptable to diverse datasets.

Deep learning models, also called convolutional neural networks (CNNs), can have 100s of layers of neural networks, made up of convolutional layers, activation layers, pooling layers and fully connected layers. Each convolution layer multiplies the pixel values of small regions of the input image by a sliding matrix of numbers called a feature. Convolution detects where a particular image feature is, such as a curve or a straight line, and produces a feature map. The feature map is then passed through an activation layer to add nonlinearity which allows the system to learn increasingly complex features. A common activation function is the rectified linear unit (ReLU), which maps negative values to zero. ReLU activation decreases model training time compared to other non-linear functions such as sigmoid or hyperbolic tangent (267,268). Pooling layers downsample the input by combining similar features in nearby areas of the image. Common strategies take the maximum or average value of local regions. Pooling decreases computational load and makes feature detection more robust by making it invariant to scale. Fully connected layers are the last layers of neural networks. A fully connected layer is unique in that each neuron within the layer is connected to each neuron in the previous layer. This allows high-level reasoning to happen because information is synthesized from the total input, rather than just from local regions as in the convolutional layers. For a classification problem, the output of the last fully connected layer is passed through a softmax function. Softmax transforms the output to produce an N dimensional vector of probabilities that sums to 1, where N is the number of class options (269). The order and number of layers in a CNN can be tailored to a particular image processing task depending on the type of input and desired output (270).

3.3.2 Steps of a deep learning algorithm for H&E tissue classification

To start, digital images of H&E-stained pathology slides are generated by a whole slide scanner. The scanner performs line or tile scanning to produce multiple high-resolution images that are stitched together to produce a final copy of the whole slide. Due to the gigapixel size of each image, WSIs require multiple processing steps before input into a machine learning algorithm (271).

A single slide has multiple tissue sections on it, and thus the first step is locating and extracting areas of tissue from background. Areas of tissue are found using thresholding to identify foreground (regions of tissue) from background. Tissue sections are divided into smaller subpatches to create square tiles of smaller, fixed dimension. The tiled dataset is then partitioned into training and test sets, with about two-thirds of the data reserved for training and one-third for testing (272). The training dataset is used to fit the parameters of the model and the test dataset to evaluate the performance of the model once it is trained. Training and test datasets must include tiles from all types of images the model will be used for. It's important to note that all training and testing images must be annotated by a pathologist to classify the type of tissue and define regions of tumor and normal tissue. This is so each tile has a ground truth for error calculation and performance evaluation during training and testing, respectively.

Training, or supervised learning, of the model consists of initialization of parameters, forward propagation, error calculation, and backward propagation to update parameters until the model achieves a specified accuracy (273,274). Parameters are initialized with random values (275) and the input data is propagated forward so that all neurons apply a transformation to the data. Once the final layer is reached and a classification of the input data is produced, the error is calculated between the model prediction and the ground truth using a loss function such as mean-squared error or cross-entropy loss (276,277). The gradient of the loss function with respect to each parameter is calculated during backpropagation and parameters are updated using a gradient descent optimization method to minimize the loss function (278). One epoch of training is completed when an entire training dataset has been passed through the network. At the end of each epoch, model accuracy is calculated as the sum of true positives and false negatives divided by the total number of samples (279). The process of forwardpass, error calculation, parameter update, and backward pass continues until model accuracy has converged to a specified percentage.

3.3.3 Convolutional neural networks (CNNs) for pixel-wise classification of skin cancers

The diagnosis of skin cancer, the most common type of cancer (280–282) would benefit from computer-aided classifiers due to the large volume of biopsies taken yearly and the variety of skin pathologies. Over 500 distinct skin pathologies exist (283), presenting a uniquely challenging classification problem.

To design a deep learning system to classify skin pathologies, we started from the U-Net model, which is composed of a contracting path and an expanding path (284). The contracting path follows the usual architecture of a CNN, using convolution and downsampling to reduce the size of the input while increasing the number of feature maps. The expanding path uses convolution and upsampling to recover the object details and spatial resolution lost in the contracting path. The output of U-Net is a heatmap of the same dimension as the input image that indicates the probability that each pixel belongs to a certain class or not. Pixel-level classification is useful for histopathology images because most tissue biopsies contain regions of normal and cancer tissue. A pixel-wise classification, rather than a single class label for the whole section, makes the results more interpretable by allowing the user to visualize which areas of the section were labelled tumor.

In the process of training U-Net models to learn various pathologies, one pathology, squamous acanthoma, was consistently being classified incorrectly as normal tissue. Squamous acanthoma (SA) is a benign neoplasm composed of squamous cells (285). The main distinguishing feature is the elongation and broadening of rete ridges, the epithelial extensions that project into the underlying connective tissue (outlined in blue in Figure 3.4A) (286). Disregarding the morphology of the rete ridges makes SA almost indistinguishable from normal skin epithelium (Figure 3.4B). The large-scale nature of SA features poses a challenge for CNN classification since models learn from small segments (tiles) of images. To provide contextual information, we created a pipeline with an additional classification model based on the whole tissue image. The whole tissue classification was used to amplify the results of the U-Net model, giving more confidence and context to the pixel-wise classification.

The tissue-level classification model required a slightly different architecture because the input images were whole tissue sections of varying dimension (Figure 3.4C) rather than tiles of fixed dimension (Figure 3.4D). Fully-connected layers require fixed-length vectors as input, so a spatial pyramid pooling (SPP) layer was added before the last fully connected layer (287). SPP pools values in local spatial bins that have sizes proportional to the image size, which fixes the number of bins regardless of the image size.

After adding contextual information in the form of whole tissue level classification, squamous acanthoma prediction increased to 97% accuracy (Figure 3.4E).

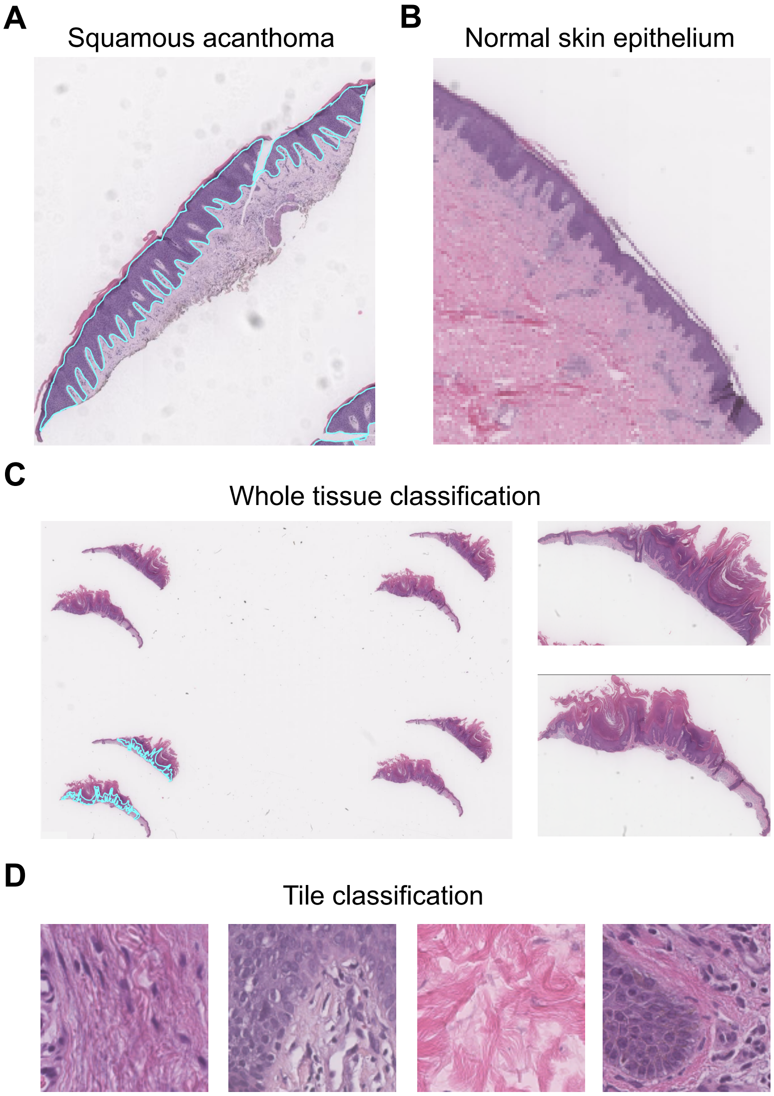

E

Actual

		Positive	Negative
Predicted	Positive	80	1
	Negative	3	41

Sensitivity = 96.4%

Specificity = 97.6%

Accuracy = 96.8%

Figure 3.4 Training and testing a squamous acanthoma classification model.
(A) A representative squamous acanthoma tissue section. Blue outlined region indicates rete ridges. (B) A representative normal skin epithelium tissue section included in the training dataset of images. (C) A whole slide image (left) with individual tissue sections (right) that are fed into whole tissue classification model. (D) Representative 512x512 tiles fed into U-Net model. (E) SA classification model performance results. Model including tissue-level and tile-level input has 97% accuracy.

3.4 Discussion

In this section, I described two applications of automated image processing used to extract meaningful information from different types of biological images. In the first, multicolor immunofluorescent images of TNBC tissue were analyzed to determine the spatial association of a tumor suppressor and its effector. In the second, digital H&E images of pathology slides were analyzed to classify diseased tissue. Both applications demonstrate the use of image pixel data to generate clinically-relevant interpretations of cancer tissue.

Immunofluorescence paired with image processing can be used to achieve spatially resolved, quantitative measurements of biological molecules in cultured cells or tissue sections. Recently, advancements in iterative immunofluorescence imaging techniques have facilitated the measurement of upwards of 40 proteins in the same biological sample (288–290). Multiplexed datasets of this size require image processing techniques to align, quantify, and normalize images at single-cell resolution (288). Machine learning algorithms would be useful for these large, multivariate imaging datasets to uncover protein properties that emerge at the single-cell and cell population levels. For example, unsupervised clustering techniques such as k-means clustering could be used to infer cell state or functional response to a drug based on compiled protein measurements per cell (291). Similar image processing techniques can be applied to other experimental pipelines, such as iterative fluorescence in situ hybridization (FISH) or single-molecule FISH, to measure RNA localization and cell-to-cell variability in gene expression (292–294).

While immunofluorescence is primarily a research tool, many imaging modalities used in the clinic, such as histopathology, also benefit from image processing techniques. Deep learning algorithms have been very successful at automatically learning complex representations of multidimensional data (264,295–297), but there are still important limitations to consider when building and using a model. Deep learning model performance relies heavily on the size and composition of the training dataset (298,299). Complex classification problems require hundreds of thousands of labelled images spanning all classes a model must distinguish between (300–302). Models trained on datasets that are too small or homogenous will overfit and not generalize well to new, unseen data (303). The scarcity of large labelled datasets limits the areas in which deep learning can currently be applied. Data augmentation is one approach that artificially increases the size and diversity of datasets by cropping, translating, and flipping training images (304–306). This is a convenient approach to reduce overfitting, as no new data or annotations must be collected.

While one of the main advantages of deep learning models is that they do not require feature engineering as traditional machine learning algorithms do, there is still a substantial amount of manual effort required to design accurate models (307). The architecture of the model, including the number and order of layers, the number of neurons per layer, and which activation function to use, is chosen in a mainly empirical manner depending on the model task. Aspects of model training including the error function and metrics to evaluate model performance also must be chosen from various options. The large number of tunable factors can make designing and training a deep learning model very time consuming and can also result in models that lack generalization.

Despite these limitations, deep learning is becoming the algorithm of choice for image analysis due to drastic improvements in accuracy over traditional machine learning approaches (308). Technological advancements in image acquisition, management, and sharing are facilitating the accessibility of data, relieving the constraints of training data curation. For example, the Cancer Imaging Archive is an open-access database that hosts an archive of medical images for over 40 types of cancer (309). Many of the image sets include pathologist annotations and clinical information to facilitate training of models to make clinically-relevant predictions. Open-source image analysis software, like the digital pathology analysis package

QuPath, is also available to allow users with less coding experience to apply machine learning techniques to their own datasets (310).

Image processing techniques have turned biological images into rich sources of data by removing the bottleneck of manual scoring and enabling identification and quantification of subtle patterns missed by the human eye. Biologists and clinicians would benefit by becoming conversant in image processing techniques to identify when and how to apply methods to extract data embedded in biological images.

Chapter 4 Sporadic activation of an oxidative stress-dependent NRF2–p53 signaling network in breast epithelial spheroids and premalignancies

4.1 Abstract

Breast–mammary epithelial cells experience different local environments during tissue development and tumorigenesis. Microenvironmental heterogeneity gives rise to distinct cell-regulatory states whose identity and importance are just beginning to be appreciated. Cellular states diversify when clonal 3D spheroids are cultured in basement membrane, and prior transcriptomic analyses identified a state associated with stress tolerance and poor response to anticancer therapeutics. Here, we examined the regulation of this state and found that it is jointly coordinated by the NRF2 and p53 pathways, which are co-stabilized by spontaneous oxidative stress within the 3D cultures. Inhibition of NRF2 or p53 individually disrupts some of the transcripts defining the regulatory state but does not yield a notable phenotype in nontransformed breast epithelial cells. In contrast, combined perturbation prevents 3D growth in an oxidative stress-dependent manner. Similar coordination of NRF2 and p53 signaling is observed in normal breast epithelial tissue and hormone-negative ductal carcinoma in situ lesions. However, the pathways are uncoupled in triple-negative breast cancer, a subtype in which p53 is usually mutated. Here, we find an oxidative stress-tolerance network that is important for single cells during glandular development and the early stages of breast cancer.

4.2 Introduction

Among glandular tissues, the breast–mammary epithelium is unique because of the dramatic expansion and reorganization that occurs after birth (311). During puberty, a branched network of epithelial ducts is pioneered by terminal end buds (TEBs), which emerge from the rudimentary gland and extend into the surrounding mesenchyme (312). TEBs contain a mixture of proliferating stem–progenitor cells and differentiating cells fated to the secretory luminal-epithelial or contractile basal-myoepithelial lineages. During morphogenesis, TEB cells are dynamically exposed to different microenvironments that inform final organization of the gland (313). Some microenvironmental cues are supportive or instructive to cells [hormones (314), growth factors (315), basement membrane (316)]. Others are deleterious or lethal [loss of polarity (317), detachment (318), ER stress (319)]. All of these cues are reconfigured aberrantly and heterogeneously during the early stages of breast–mammary cancer (320–322).

Stress and survival signals also juxtapose when breast–mammary epithelial cells are grown in 3D culture with reconstituted basement membrane ECM (323,324). Combining the appropriate adhesive and soluble cues yields TEB-like behavior in 3D-cultured multicellular epithelial fragments from the mammary gland (317). For single-cell cultures that reliably organize as 3D structures, clones or progenitors must iteratively proliferate, maintain cell-cell adhesions, and coordinate function to establish a multicellular ecosystem (325,326). Cell-regulatory states diversify within 3D organoids of primary breast–mammary epithelia (327–329) and also in the simplest 3D spheroids of isogenic cell lines (11,330–332). Identifying such cell-regulatory heterogeneities is important, because there are parallels to in situ lesions of the breast, where premalignant cells must survive and proliferate in the duct (333,334).

Previously, we identified a cluster of transcripts (Figure 4.1A) that covaries heterogeneously among hormone-negative, basal breast epithelial cells grown as 3D spheroids (333). The cluster contains *KRT5* (a PAM50 classifier for basal-like breast cancer) (19) along with multiple stress-tolerance genes, including *JUND* (335), *CDKN1A* (336), *MUS81* (337), and *HSPE1* (338). The transcripts in this cluster were among the strongest and most-negative predictors of breast-cancer response to chemotherapy and targeted agents in an independent clinical trial (339). We reported that individual genes in the cluster have complex time- and microenvironment-dependent relationships in 3D spheroids, animal models of ductal carcinoma in situ (DCIS), and clinical hormone-negative premalignancies (333). However, the overarching regulation of the cluster was not determined.

Here, we find that regulatory-state heterogeneity emerges from the coordinated action of two stress-responsive transcription factors—NRF2 (340,341) and p53 (342)—which become stabilized posttranslationally when breast-epithelial cells variably experience oxidative stress in 3D culture. Genetic disruption of NRF2 signaling alters the transcriptional cluster, but 3D phenotypes are buffered or redirected by compensatory increases in p53 signaling. Disabling p53 function synergizes with NRF2 deficiency, suppressing normal 3D proliferation and promoting irregular hyperproliferation in a transformed-yet-premalignant derivative. Among clinical specimens, NRF2–p53 coordination is retained in normal primary breast tissue and hormone-negative DCIS. However, the two pathways are largely uncoupled in triple-negative breast cancers (TNBCs), where p53 is usually mutated. Past work on NRF2 in breast cancer has focused on its direct interactions with TNBC tumor suppressors (110,162). Our results suggest a broader systems-level role for NRF2 and p53 in oxidative-stress tolerance of normal breast–mammary epithelia and hormone-negative premalignancies.

4.3 Results

4.3.1 Statistical bioinformatics links gene-cluster regulation to NRF2 and p53

We began by looking within the gene cluster (Figure 4.1A) for potential regulatory mechanisms. The only transcription factor in the cluster is JUND, and we showed previously that its chronic knockdown in MCF10A-5E cells (330) causes specific morphometric defects during spheroid growth (333). We revisited these results by acutely knocking down JUND with inducible shRNA and measuring transcript abundance of cluster genes by quantitative PCR (see Materials and Methods). Surprisingly, other than JUND itself, no transcripts were reliably altered by knockdown (Figure 4.2A), supporting a regulatory role for other factors outside of the cluster.

We constrained the search for candidate regulators by using maximum-likelihood inference (343) to estimate a frequency of bimodal transcriptional regulation (344) for the gene cluster. Given the 10-cell-averaged fluctuations from the original study (Figure 4.1A) (330), the maximum-likelihood approach inferred two lognormal regulatory states defined by transcript abundance (Figure 4.1B). The data supported a low-abundance regulatory state predominating in 58% of ECM-attached cells along with a second, high-abundance subpopulation in the remaining 42%. The frequency estimates placed quantitative bounds on the bimodal characteristics of upstream regulatory mechanisms.

Next, we applied a panel of bioinformatics approaches to search for transcription factors that might impinge upon the gene cluster (see Materials and Methods). The informatic methods adopt different strategies for assessing binding-site overrepresentation (345–348). Therefore, we intersected their respective outputs to arrive at predictions that were robust to algorithmic details. The analysis converged upon two transcription factors: the G1/S regulator E2F1 and the stress-response effector NRF2 (Figure 4.1C). We assessed the relative activation of the NRF2 and E2F1 pathways in single cells by quantitative immunofluorescence for total stabilized NRF2 protein or hyperphosphorylated RB (pRB = disinhibited E2F1; see Materials and Methods). In 3D spheroid cultures, pRB immunostaining was bimodal, but high-pRB cells were far rarer than the inferred regulatory frequency of the gene cluster (Figure 4.1D, upper). In 2D cultures, pRB staining was over twice as immunoreactive and nearly twice as prevalent in the population (Figure 4.1D, middle). The reduced proportion of high-pRB cells in 3D is consistent with the proliferative suppression of late-stage spheroid cultures (332). A 3D-like distribution of pRB was achieved in 2D cultures upon addition of dilute ECM (Figure 4.1D, lower) stemming from soluble proliferation-suppressing factors in the reconstituted basement membrane preparation (349). By contrast, NRF2 stabilization was only distinctly bimodal in 3D spheroids, and the observed frequency of low- and high-NRF2 states almost exactly coincided with that inferred for the gene cluster (Figure 4.1E). The results built a strong statistical argument for NRF2 as a covarying regulator of the gene cluster.

The NRF2-associated gene cluster (Figure 4.1A) was originally identified by quantitative analysis of transcriptomic fluctuations among 4557 genes profiled by oligonucleotide microarray (330). Recently, the same samples were reprofiled by 10-cell RNA sequencing (10cRNA-seq) (350), creating an opportunity to look more deeply at covariates with the NRF2-associated gene cluster. We used the median ranked fluctuations of the cluster across 10-cell samples (Figure 4.1A) and surveyed the 10cRNA-seq data for genes that covaried (Spearman $\rho > 0.5$, $q < 0.10$), identifying 633 candidates (Figure 4.3A). When this expanded cluster was assessed for functional enrichments by Gene Ontology (GO) (351), we noted multiple GO terms linked to cell stress ("Response to stress", "Oxidative stress") and the transcription factor p53 ("DNA damage response", "p53 pathway"; $q < 0.05$ by hypergeometric test). p53 is sporadically stabilized in regenerating epithelia such as the intestine and skin, but p53 activation in quiescent tissues is rare (352). Recognizing the residual proliferation observed in 3D cultures (Figure 4.1D), we immunostained for p53 and found nonuniform stabilization associated with the abundance of NRF2 in single cells (Figure 4.3B, estimated mutual information: MI = 0.15 [0.12–0.18]; see Materials and Methods). The analysis raised the possibility of a coordinated NRF2–p53 regulatory event triggered heterogeneously when breast epithelial cells proliferate and organize in reconstituted ECM.

NRF2 co-immunoprecipitates with p53 in triple-negative breast cancer cells harboring gain-of-function p53 mutations, but this complex is absent in MCF10A cells with wildtype p53 (162). Loss of wildtype p53 function in MCF10A cells yields only minor 3D culture defects, but gain-of-function p53 mutants strongly perturb 3D architecture (353). Suspecting that some of p53's effects could be explained through NRF2, we inducibly knocked down NRF2 with shRNA and inducibly coexpressed a truncated p53 (354) that acts as a dominant negative (DNp53; Figure 4.3C). Compared with the gene-cluster response to JUND knockdown or constitutive E2F1 activation through RB inhibition with overexpressed human papillomavirus E7 protein, we observed substantially more alterations upon NRF2 knockdown (66%) or inhibition of p53 (31%;

Figure 4.3D and 4.2, B to D). Compound perturbation of NRF2 and p53 elicited further nonadditive changes to multiple genes in the cluster, including synergistic reduction of the cyclin-dependent kinase inhibitor, CDKN1A, and the basal cytokeratin, KRT5 (interaction $p < 0.01$ by two-way ANOVA). Although p53 can antagonize certain NRF2 target genes in reporter assays (355), significant antagonism was detected for only one transcript in the cluster (MRPL33, Figure 4.2C). Phenotypically, disruption of NRF2 reduced mean 3D growth by 10–13% (Figure 4.4), but dual perturbation with p53 gave rise to a surprising increase in aborted spheroids unable to grow in the culture (Figure 4.3E). The penetrance of the phenotype (37%; range: 34–44%) was remarkably close to the percentage of cells showing stabilized NRF2 at the same time point of 3D culture (43%, Figure 4.1E). For this clonal basal-like breast epithelial line (330), we conclude that 3D culture heterogeneously elicits NRF2- and p53-inducing stresses, which must be withstood for extended proliferation.

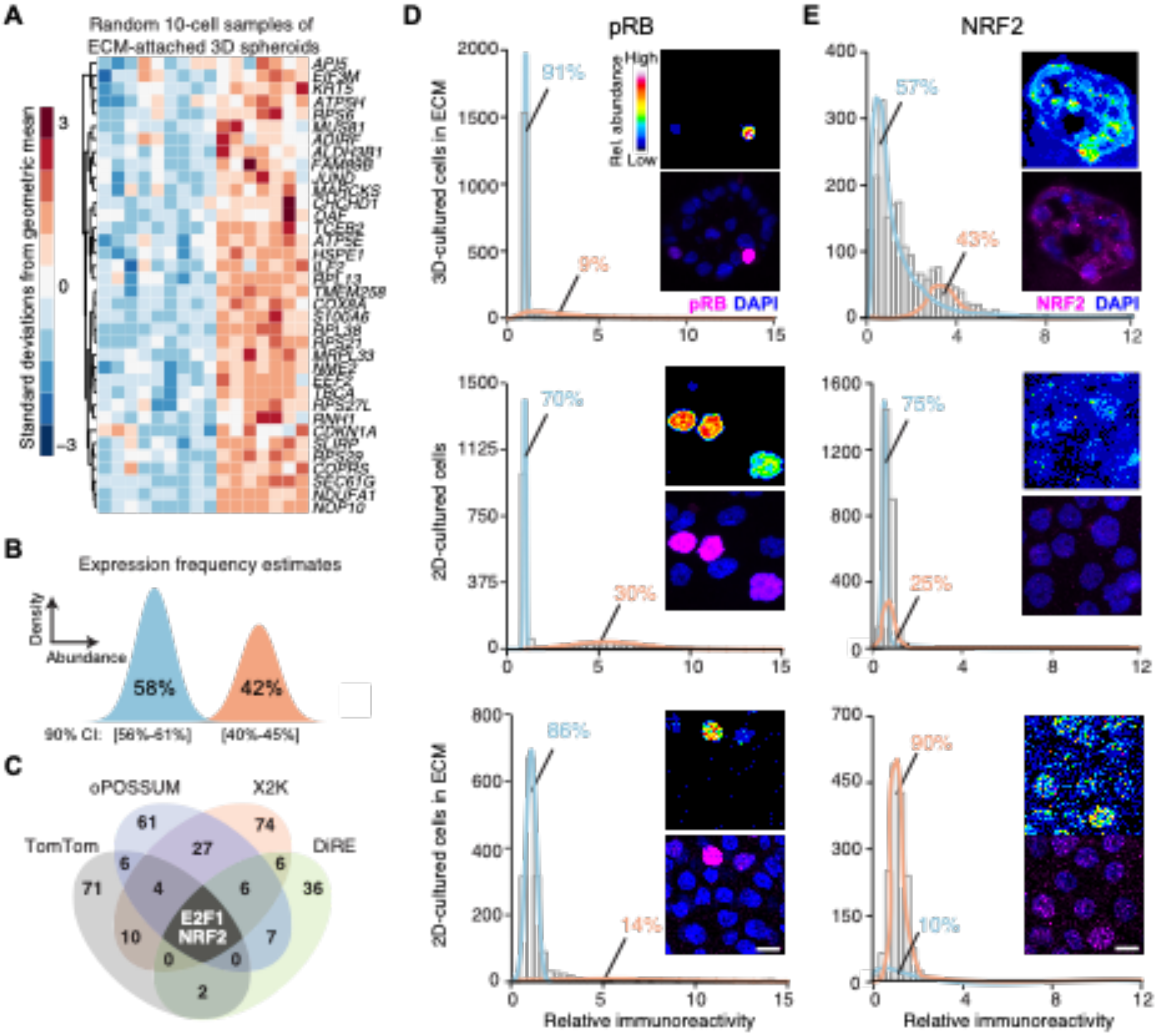

Figure 4.1 Transcriptomic fluctuations of ECM-cultured breast epithelial spheroids reveal a gene cluster associated with heterogeneous NRF2 stabilization in a 3D-specific environment.

(A) Microarray profiles of ECM-attached basal-like MCF10A-5E breast epithelial cells randomly collected as 10-cell pools (n = 16) from 3D-cultured spheroids after 10 days (330). (B) Maximum-likelihood inference (343) parameterizes a two-state distribution of transcript abundances for the gene cluster in (A). Inferred expression frequencies are shown as the maximum likelihood estimate with 90% confidence interval (CI). (C) Promoter-bioinformatics methods converge upon NRF2 and E2F1 as candidate regulators of the gene cluster. (D and E) Quantitative immunofluorescence of (D) hyperphosphorylated RB (pRB, an upstream proxy of active E2F1) and (E) NRF2 in 3D culture with ECM (upper), 2D culture (middle), and 2D culture with ECM (lower). Expression frequencies for a two-state lognormal mixture model (preferred over a one-state model by F test; $p < 0.05$) were calculated by nonlinear least squares of 60 histogram bins collected from n = 1100–1600 of cells quantified from 100-200 spheroids from two separate 3D cultures. For each subpanel, representative pseudocolored images are shown in the upper right inset and merged (magenta) with DAPI nuclear counterstain (blue) in the lower right inset. Scale bar is 10 μm.

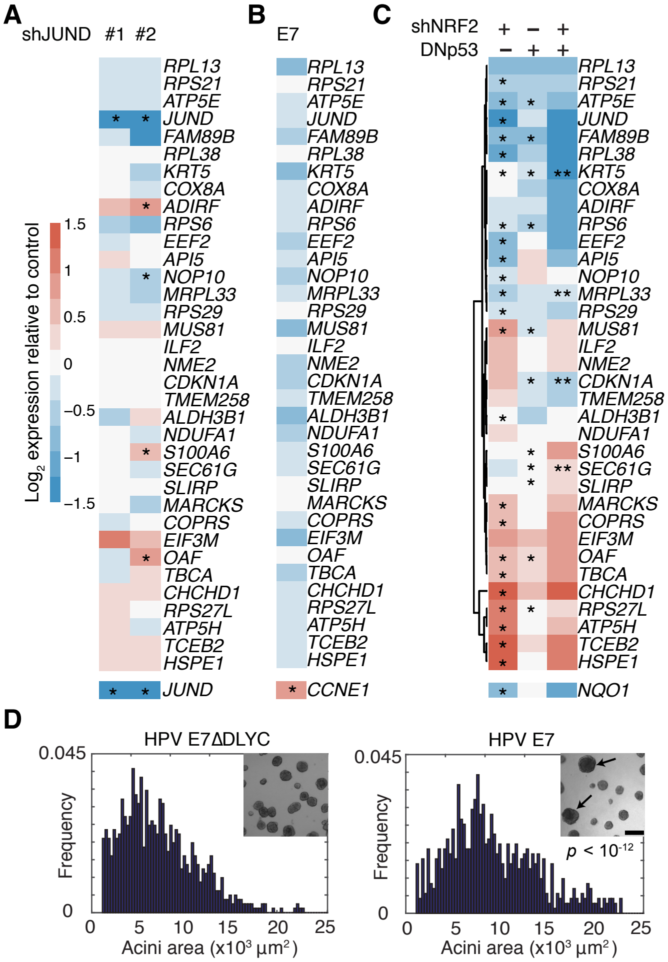

Figure 4.2 Abundance of the heterogeneously regulated gene cluster is perturbed by NRF2 knockdown or p53 disruption but not by JUND knockdown or human papillomavirus (HPV) E7-induced inhibition of RB.

(A) Inducible JUND knockdown does not reliably affect transcripts within the gene cluster other than JUND. (B) Constitutive inhibition of RB with HPV E7 does not significantly affect transcript abundance within the gene cluster. The E2F1 target gene CCNE1 was used as a control for efficacy of ectopic E7 expression. (C) Single and combined perturbations of NRF2 and p53 have complex effects on the gene cluster. The NRF2 target gene NQO1 was used as a control for efficacy of shNRF2. (D) E7 expression elicits hyperproliferation (332) compared to a ΔDLYC control that does not bind RB (356) For (A) and (C), MCF10A-5E cells with or without JUND or NRF2 knockdown or DNp53 were treated with 1 µg/ml doxycycline for 48 hr, grown as 3D spheroids for 10 days, and profiled for the indicated genes by quantitative PCR. For (B) and (D), MCF10A-5E cells stably expressing E7 or E7ΔDLYC were grown as 3D spheroids for 10 days and profiled for the indicated genes by quantitative PCR or imaged by brightfield microscopy and segmented after 22 days. For (A) to (C), data are shown as the log2 geometric mean relative to the negative control (shGFP (A and C) or E7ΔDLYC (B) with or without FLAG-tagged LacZ (C)), with asterisks indicating significant changes or interaction effects (rightmost column of (C)) by two-way ANOVA of n = 8 (A and C) or 4 (B) independent 3D-cultured samples and a false-discovery rate of 5%. For (D), size histograms were compared by K-S test and scale bars are 200 µm.

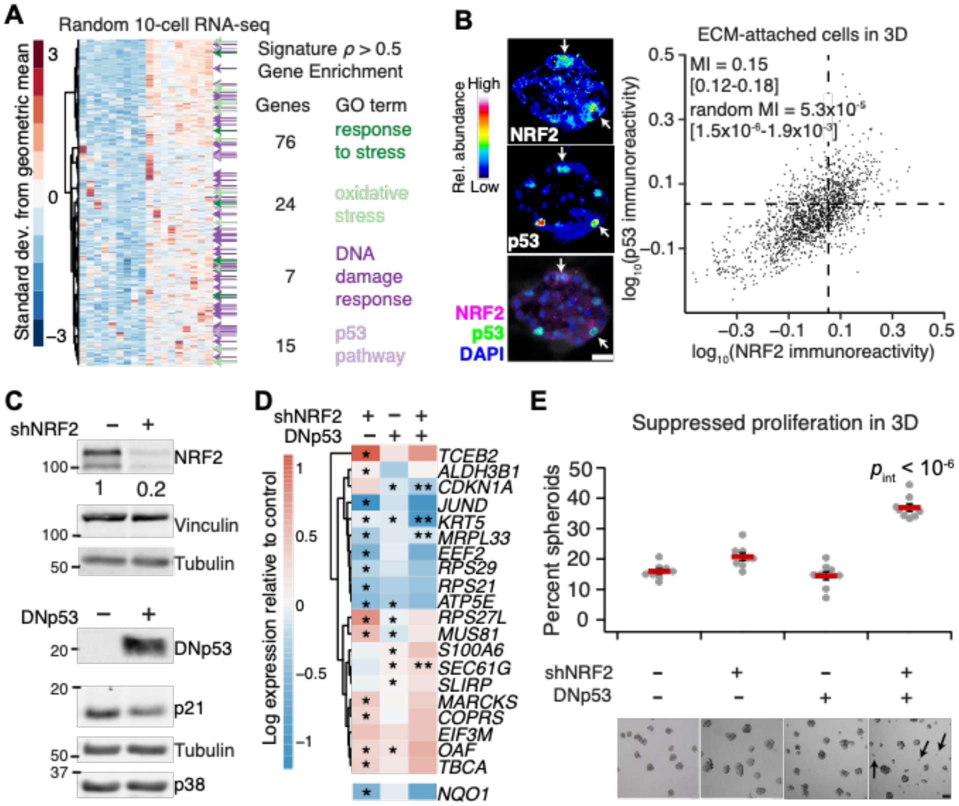
A
Random 10-cell RNA-seq
Standard dev. from geometric mean
3
0
−3
Signature ρ > 0.5
Gene Enrichment
Genes
GO term
76
response to stress
24
oxidative stress
7
DNA damage response
15
p53 pathway
B
Rel. abundance
High
Low
NRF2
p53
NRF2
p53
DAPI
ECM-attached cells in 3D
MI = 0.15
[0.12-0.18]
random MI = 5.3x10^-5
[1.5x10^-6-1.9x10^-3]
log10(p53 immunoreactivity)
log10(NRF2 immunoreactivity)
0.5
0.3
0.1
−0.1
−0.3
C
shNRF2
−
+
NRF2
1
0.2
Vinculin
Tubulin
DNp53
−
+
DNp53
p21
Tubulin
p38
100
100
50
20
20
50
37
D
shNRF2
DNp53
Log expression relative to control
1
0.5
0
−0.5
−1
TCEB2
ALDH3B1
CDKN1A
JUND
KRT5
MRPL33
EEF2
RPS29
RPS21
ATP5E
RPS27L
MUS81
S100A6
SEC61G
SLIRP
MARCKS
COPRS
EIF3M
OAF
TBCA
NQO1
E
Suppressed proliferation in 3D
Percent spheroids
50
40
30
20
10
0
p_int < 10^-6
shNRF2
DNp53

Figure 4.3 Transcriptome-wide covariate analysis of the NRF2-associated gene cluster suggests a coordinated adaptive-stress response involving p53.
(A) Transcripts covarying with the median NRF2-associated fluctuation signature (Figure 4.1A) measured by 10-cell RNA sequencing (350) of ECM-attached MCF10A-5E cells grown as 3D spheroids (n = 18 10-cell pools from GSE120261). Selected Gene Ontology enrichment analysis (green and purple) is shown for the transcripts with a Spearman correlation (ρ) greater than 0.5. (B) Stabilization of NRF2 and p53 proteins is coordinated in ECM-attached MCF10A-5E cells grown as 3D spheroids. Representative pseudocolored images for NRF2 (upper left) and p53 (middle left) are shown merged with DAPI nuclear counterstain (lower left). White arrows indicate concurrent NRF2 and p53 stabilization. Median-scaled two-color average fluorescence intensities are quantified (right) along with the log-scaled and background-subtracted mutual information (MI) with 90% CI for n = 1691 cells segmented from 50–100 spheroids from two separate 3D cultures. (C) Genetic perturbation of NRF2 by inducible shRNA knockdown (upper) and p53 by inducible expression of a FLAG-tagged carboxy terminal (residues 1-13, 302-390) dominant-negative p53 (DNp53, lower) (354). MCF10A-5E cells were treated with 1 µg/ml doxycycline for 72 hr (upper) or 24 hr (lower) and immunoblotted for NRF2 or FLAG with vinculin, tubulin, and p38 used as loading controls and p21 used to confirm efficacy of DNp53. The negative control for shNRF2 was an inducible shGFP, and the negative control for DNp53 was FLAG-tagged LacZ. (D) Single and combined perturbations of NRF2 and p53 have complex effects on the associated gene cluster (Figure 4.1A). NQO1 was used as a control for efficacy of shNRF2, CDKN1A shows efficacy of DNp53. MCF10A-5E cells with or without NRF2 knockdown or DNp53 were treated with 1 µg/ml doxycycline for 48 hr, grown as 3D spheroids for 10 days, and profiled for the indicated genes by quantitative PCR. Data are shown as the log2 geometric mean relative to the negative control (shGFP + FLAG-tagged LacZ), with asterisks indicating significant changes (left and middle columns) or interaction effects (right column) by two-way ANOVA of n = 8 independent 3D-cultured samples and a false-discovery rate of 5%. The complete set of transcripts in the gene cluster is shown in Figure 4.2C. (E) Dual inactivation of NRF2 and p53 causes synergistic proliferative suppression in MCF10A-5E 3D spheroids. Black arrows indicate proliferation-suppressed spheroids. Data are shown as the mean percentage of proliferation-suppressed spheroids ± s.e.m. of n = 8 independent 3D-cultured samples after 10 days. Statistical interaction between NRF2 and p53 (pint) was assessed by two-way ANOVA with replication. Scale bars are 20 µm (B) and 100 µm (E).

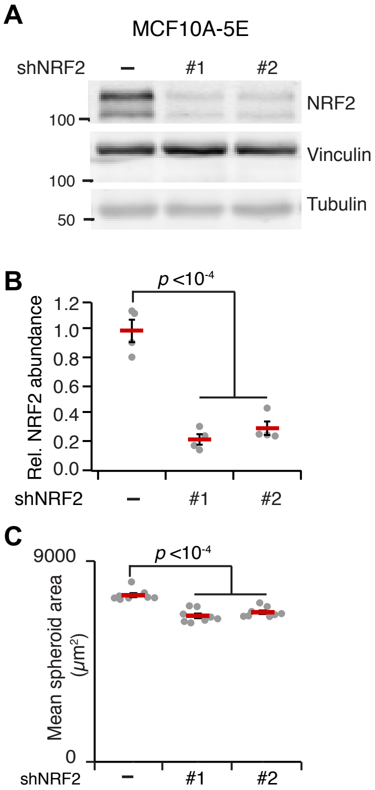

Figure 4.4 NRF2 knockdown and 3D phenotype quantification in MCF10A-5E cells.
(A) Knockdown of endogenous NRF2 by shRNA in doxycycline-treated MCF10A-5E cells. MCF10A-5E cells were treated with 1 µg/ml doxycycline for 72 hr and immunoblotted for NRF2 with vinculin and tubulin used as loading controls. (B) Densitometry from replicated NRF2 knockdown. Data are shown as the mean ± s.e.m. of n = 4 biological replicates. (C) Inducible knockdown of NRF2 causes mild growth inhibition of MCF10A-5E 3D spheroids. Data are shown as the mean ± s.e.m. of n = 8 independent 3D-cultured samples after 10 days.

4.3.2 NRF2 disruption in basal-like premalignancy causes similar p53 adaptations but different 3D phenotypes

We next asked how the cellular, molecular, and phenotypic relationships between NRF2 and p53 change in basal-like premalignancy by using isogenic MCF10DCIS.com cells (357) as a proxy for ductal carcinoma in situ (358). MCF10DCIS.com cells express oncogenic HRAS (359) and hyperproliferate as 3D spheroids (Figure 4.5A), but they retain wildtype p53 function, albeit at reduced levels compared to parental MCF10A cells (Figure 4.5 B,C). By two-color immunostaining, we found that NRF2–p53 co-stabilization was even more pronounced in MCF10DCIS.com cells (Figure 4.7A, MI = 0.30 [0.27–0.33]). To identify common adaptive programs downstream of NRF2 deficiency, we inducibly knocked down NRF2 and profiled 3D spheroids by RNA sequencing (see Materials and Methods). Among transcripts consistently increased or decreased in both MCF10A-5E and MCF10DCIS.com spheroids, there was a significant enrichment in gene signatures encompassing p53, including transcriptional programs downstream of BRCA1, ATM, and CHEK2 (Figure 4.7B). Consistent with these results, NRF2 knockdown in MCF10DCIS.com cells was sufficient to stabilize p53 significantly (Figure 4.6A). Stabilization of wildtype p53 upon NRF2 knockdown was also observed in premalignant CHEK2^{1100delC} SUM102PT cells (360) and became even more pronounced when these cells were reconstituted with inducible wildtype CHEK2 (Figure 4.6 B,C) (361). Thus, NRF2 impairment promotes p53 pathway activity in basal-like breast epithelia without the need for specific oncogenic drivers.

Despite many transcriptomic alterations in common with MCF10A-5E cells (Figure 4.7B), MCF10DCIS.com cells yielded very different 3D phenotypes when NRF2 or p53 were perturbed. NRF2 knockdown did not detectably alter 3D growth (Figure 4.8A) but instead gave rise to more round, organized MCF10DCIS.com spheroids of high circularity compared to control (Figure 4.7C), which reverted upon addback of an RNAi-resistant NRF2 mutant (Figure

4.8B). NRF2 deficiency also increased rounding in 3D cultures of SUM102PT cells with or without CHEK2 reconstitution (Figure 4.8C). By contrast, p53 disruption in MCF10DCIS.com cells with either DNp53 or a gain-of-function p53R280K mutant increased the prevalence of hyperenlarged outgrowths (Figure 4.7D). Combined NRF2–p53 perturbation elicited a synergistic increase in non-spherical hyper-enlargement (Figure 4.7E, interaction $p < 0.05$ by two-way ANOVA), starkly contrasting the proliferative suppression observed with the same combination in nontransformed MCF10A-5E cells (Figure 4.3E). The data suggested that the coordinate transcriptional adaptations of NRF2 and p53 are conserved in premalignant cells but insufficient to buffer the cellular phenotypes caused by single-gene perturbations in either pathway.

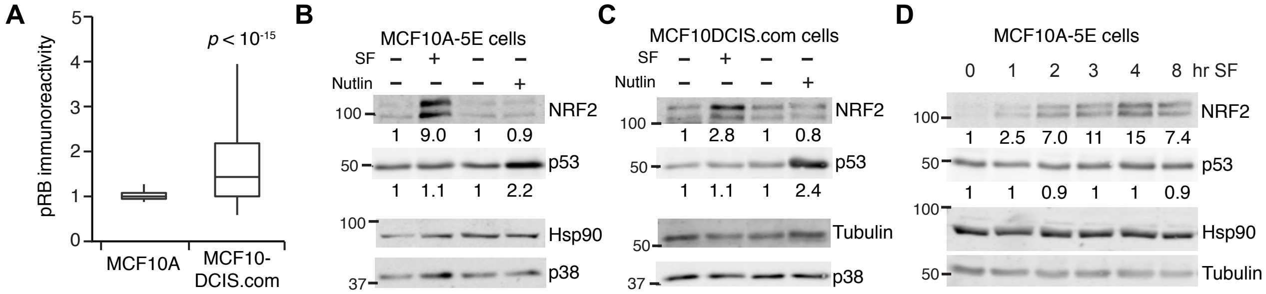

Figure 4.5 Proliferation differences and signaling similarities between MCF10A-5E and MCF10DCIS.com cells.

(A) MCF10DCIS.com cells show sustained RB phosphorylation (pRB) in 3D cultures compared to MCF10A-5E spheroids. pRB staining was quantified after 10 days of 3D culture collected from n = 1350 cells from 60–70 spheroids per cell line. (B and C) Both MCF10A-5E and MCF10DCIS.com cells stabilize NRF2 in response to the electrophile sulforaphane (SF) and stabilize p53 in response to the MDM2 inhibitor Nutlin-3. (D) p53 is not stabilized by SF for up to eight hours in MCF10A-5E cells. Cells were treated with 10 µM SF for two hours or 10 µM Nutlin-3 for four hours (B and C) or 10 µM SF for the indicated times (C) and immunoblotted for NRF2 and p53 with Hsp90, tubulin, and p38 used as loading controls. Representative immunoblots are shown from biological duplicates.

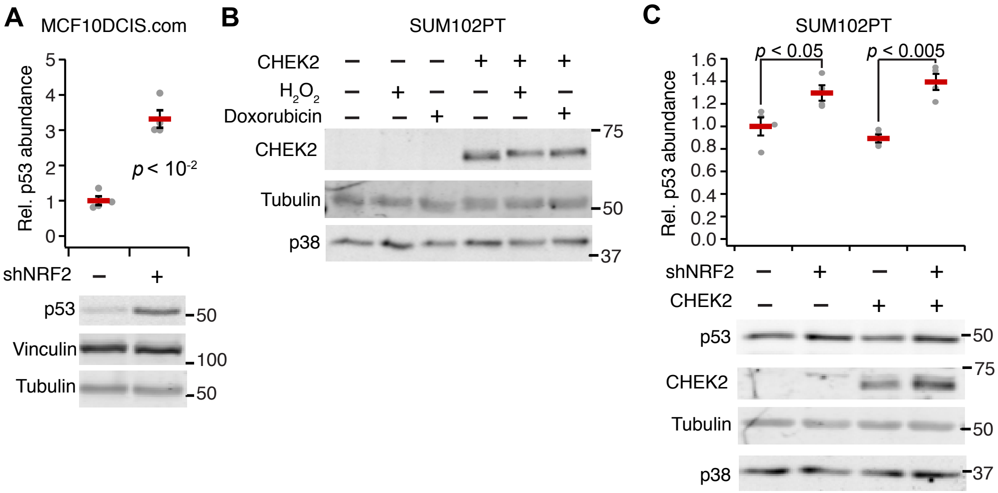

Figure 4.6 NRF2 knockdown causes p53 stabilization in premalignant breast epithelial cell lines.

(A) Inducible knockdown of NRF2 causes p53 stabilization in MCF10DCIS.com cells. MCF10DCIS.com cells were treated with 1 µg/ml doxycycline for 72 hr and immunoblotted for p53 with vinculin and tubulin used as loading controls. Representative immunoblots are shown of n = 4 biological replicates. (B) Reconstituted CHEK2 expression in *CHEK2*^{1100delC} SUM102PT cells. Note that reconstituted CHEK2 is upshifted upon H_2O_2-induced oxidative stress and doxorubicin-induced DNA damage, suggesting modification by upstream kinases. (C) Inducible knockdown of NRF2 causes p53 stabilization in SUM102PT cells and becomes more pronounced upon reconstitution of wild-type CHEK2. SUM102PT cells were treated with 1 µg/mL doxycycline for 72 hr and immunoblotted for p53 and CHEK2 with tubulin and p38 used as loading controls. Representative immunoblots are shown as the mean ± s.e.m. of n = 4 biological replicates.

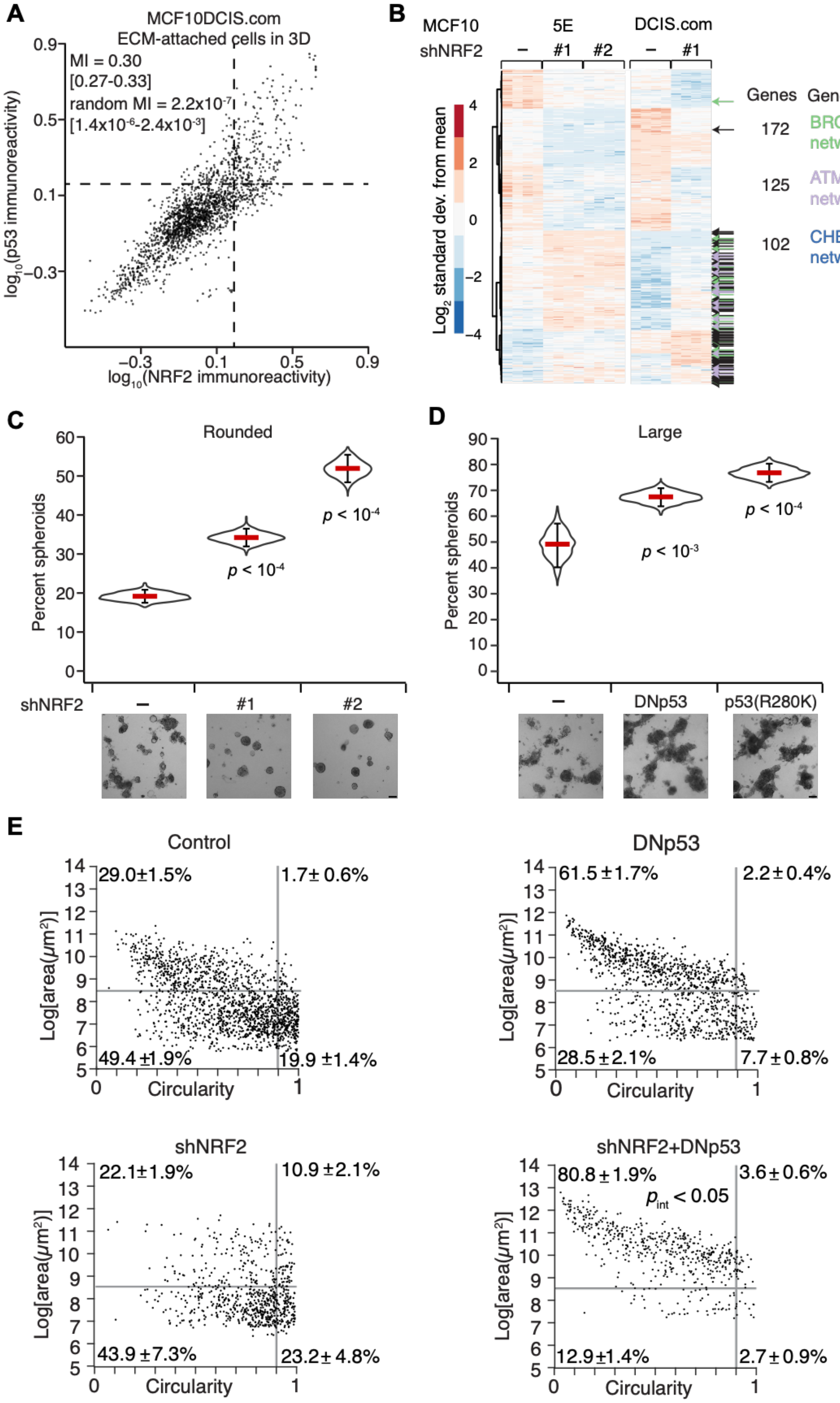
A
MCF10DCIS.com
ECM-attached cells in 3D
MI = 0.30
[0.27-0.33]
random MI = 2.2x10⁻⁷
[1.4x10⁻⁶-2.4x10⁻³]
log10(p53 immunoreactivity)
log10(NRF2 immunoreactivity)
0.9
0.5
0.1
−0.3
B
MCF10
5E
DCIS.com
shNRF2
–
#1
#2
Log2 standard dev. from mean
4
2
0
−2
−4
Genes
Gene set
172
BRCA1 network
125
ATM network
102
CHEK2 network
C
Rounded
Percent spheroids
p < 10⁻⁴
p < 10⁻⁴
shNRF2
–
#1
#2
D
Large
Percent spheroids
p < 10⁻³
p < 10⁻⁴
–
DNp53
p53(R280K)
E
Control
29.0±1.5%
1.7± 0.6%
49.4 ±1.9%
19.9 ±1.4%
DNp53
61.5 ±1.7%
2.2 ± 0.4%
28.5 ± 2.1%
7.7 ± 0.8%
shNRF2
22.1±1.9%
10.9 ±2.1%
43.9 ±7.3%
23.2± 4.8%
shNRF2+DNp53
80.8 ± 1.9%
3.6 ± 0.6%
p_int < 0.05
12.9 ±1.4%
2.7 ± 0.9%
Log[area(μm²)]
Circularity
0
1

Figure 4.7 NRF2–p53 co-stabilization is enhanced and shNRF2-induced p53 adaptations are preserved in basal-like premalignancy but have different morphometric consequences.

(A) Stabilization of NRF2 and p53 proteins is coordinated in ECM-attached MCF10DCIS.com cells grown as 3D spheroids. Median-scaled two-color average fluorescence intensities are quantified along with the log-scaled and background-subtracted mutual information (MI) with 90% CI for n = 1832 cells segmented from 70–110 spheroids from two separate 3D cultures. (B) Common changes in transcript abundance identified by RNA sequencing of MCF10A-5E (5E) and MCF10DCIS.com (DCIS.com) cells grown as 3D spheroids with or without NRF2 knockdown. The negative control for shNRF2 was an inducible shGFP (5E) or shLacZ (DCIS.com). Data are shown as log2-transformed Z-scores for genes detected at >5 transcripts per million from n = 4 biological replicates. Enriched gene sets for the BRCA1, ATM, and CHEK2 networks are indicated, with black denoting multiple enrichments. The complete list of enrichments is available in file S2. (C) NRF2 knockdown elicits a rounding phenotype in 3D-cultured MCF10DCIS.com cells. (D) p53 perturbation causes hyper-enlargement of 3D-cultured MCF10DCIS.com cells. (E) Dual inactivation of NRF2 and p53 synergistically increases the percentage of non-spherical, hyper-enlarged structures in 3D-cultured MCF10DCIS.com cells. For (C) to (E), cells with or without inducible perturbations were treated with 1 µg/ml doxycycline for 48 hr, grown as 3D spheroids for 10 days, imaged by brightfield microscopy, and segmented. For (C) and (D), data are shown as the mean ± 90% bootstrap-estimated CI from n = 8 biological replicates. For (E), data are shown as the mean ± s.e.m. of n = 8 biological replicates. Statistical interaction between NRF2 and p53 perturbations (p_{int}) was assessed by two-way ANOVA with replication. Scale bars are 100 µm.

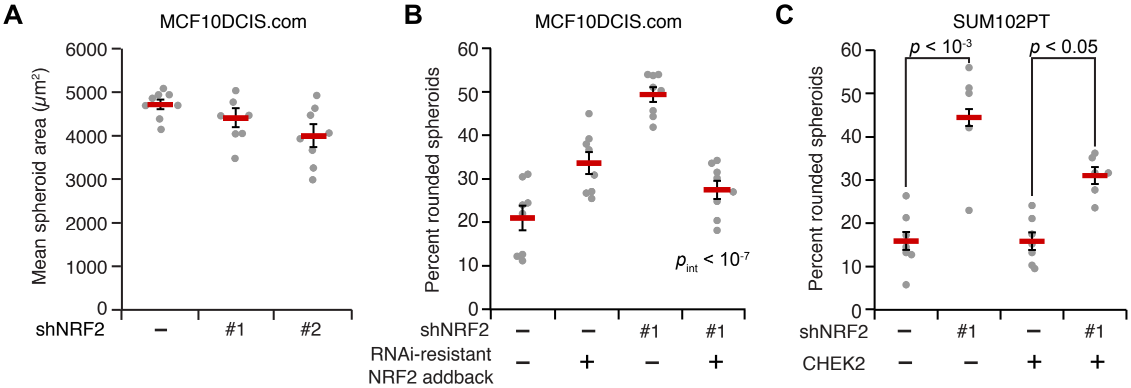

Figure 4.8 Premalignant breast epithelial cell lines have similar adaptations to NRF2 knockdown in spheroid culture.

(A) NRF2 knockdown in MCF10DCIS.com cells does not alter spheroid growth. (B) NRF2 knockdown in MCF10DCIS.com cells causes an increase in rounded spheroids (Figure 4.7C) that is reverted upon addback of an RNAi-resistant version of NRF2. (C) NRF2 knockdown in SUM102PT cells causes increased rounding with or without wild-type CHEK2 reconstitution. Data are shown as the mean ± s.e.m. of n = 8 independent 3D-cultured samples after 8 days (A and B) and n = 6 independent 3D-cultured samples after 16 days (C). For (C), cultures were treated with 1 μg/ml doxycycline at day 8 and analyzed at day 16. For (B) and (C), rounded spheroids were gated as in Figure 4.7, C and E.

4.3.3 NRF2 and p53 are coordinately stabilized by sporadic oxidative stress

Coordination of the NRF2–p53 pathways could be achieved if they shared the same inducer. We thus considered various potential upstream-and-intermediate triggers for NRF2 and p53 stabilization in basal-like breast epithelia. Inhibition of KEAP1 with the electrophile sulforaphane (362) stabilized NRF2 but not p53, and pharmacologic inhibition of MDM2 with nutlin-3 (363) stabilized p53 but not NRF2 (Figure 4.5, B to D), suggesting they act as parallel pathways downstream of a common inducer. An obvious candidate was DNA damage given *CDKN1A* and *MUS81* in the gene cluster (Figure 4.1A) and the most-recognized function of p53 (364). However, chemotherapy-induced double-strand breaks did not appreciably stabilize NRF2 in cells with wildtype p53 (Figure 4.9A), and genetically driving hyperproliferation (365) did not detectably impact regulation of the gene cluster in 3D spheroids (Figure 4.2 B,D). The lack of NRF2–p53 co-induction by conventional agonists prompted a search for less canonical activators.

One shared inducer of the KEAP1–NRF2 and ATM–CHEK2–p53 pathways is oxidative stress (71,366). In human breast tissue, elevated levels of reactive oxygen species are generated and tolerated by basoluminal progenitors (367), which are the cells of origin for basal-like breast cancer (368). We documented local niches of Nrf2 stabilization in the murine mammary gland during puberty (Figure 4.10), potentially linking NRF2 and oxidative stress in expanding progenitor(-like) cells, such as MCF10A. When MCF10A-5E cells were exogenously stimulated with H_2O_2, NRF2 was rapidly stabilized and, importantly, p53 also accumulated after several hours (Figure 4.9B). Recognizing oxidative-stress heterogeneities in 3D spheroids (11,331,369), we used the genetically-encoded sensor HyPer-2 (370) together with a novel mRFP1-NRF2 reporter (NRF2rep) to colocalize intracellular H_2O_2 with stabilized NRF2 (see Materials and methods and Figure 4.11). We observed a small-but-nonzero mutual information between HyPer-2 fluorescence ratios and NRF2rep (Figure 4.9C, MI = 0.05 [0.02–0.10]; randomized MI = 0.0004 [0.0001–0.0007]), suggesting a weak (or complex) connection between the two. Next, we evaluated whether oxidative stress resided upstream of NRF2–p53 coordination by using the vitamin E analog Trolox to quench reactive oxygen species in the 3D cultures. Trolox treatment halved the mutual information between stabilized NRF2–p53 and significantly reduced the synergistic proliferative suppression caused by dual perturbation of NRF2 and p53 (Figure 4.9D,E and 4.12). Together, the data strongly suggested that NRF2 and p53 pathway co-regulation involves upstream heterogeneities in oxidative stress.

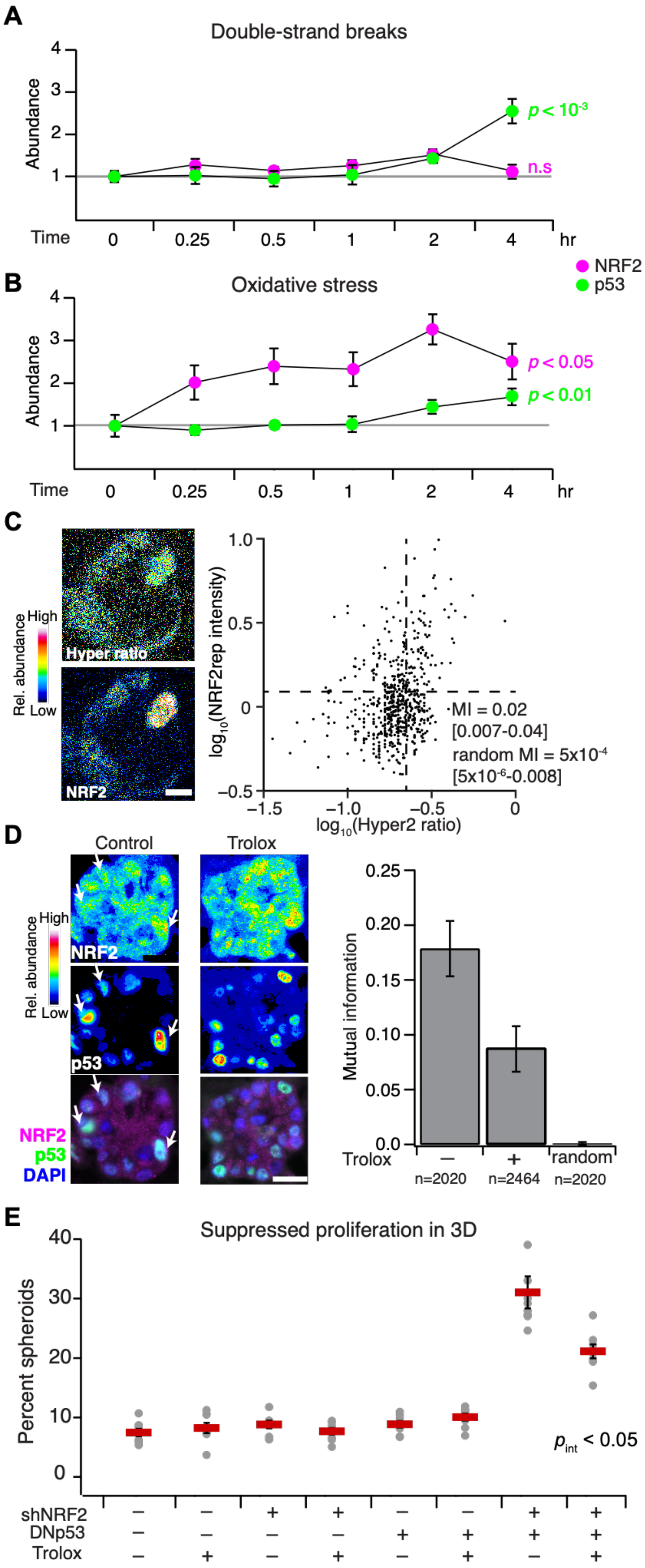
A
Double-strand breaks
Abundance
4
3
2
1
Time
0
0.25
0.5
1
2
4
hr
$p < 10^{-3}$
n.s
NRF2
p53
B
Oxidative stress
Abundance
$p < 0.05$
$p < 0.01$
C
High
Low
Rel. abundance
Hyper ratio
NRF2
$\log_{10}$(NRF2rep intensity)
$\log_{10}$(Hyper2 ratio)
MI = 0.02
[0.007-0.04]
random MI = 5x10^{-4}
[5x10^{-6}-0.008]
D
Control
Trolox
NRF2
p53
NRF2
p53
DAPI
Mutual information
Trolox
–
+
random
n=2020
n=2464
n=2020
E
Suppressed proliferation in 3D
Percent spheroids
p_{int} < 0.05
shNRF2
DNp53
Trolox

Figure 4.9 NRF2–p53 signaling coordination and 3D phenotypes arise from spontaneous and oncogene-induced oxidative stress.
(A and B) NRF2 and p53 are jointly activated by oxidative stress but not by DNA double-strand breaks. MCF10A-5E cells were treated with 5 µM doxorubicin (double-strand breaks) or 200 µM H_2O_2 (oxidative stress) for the indicated time points, and NRF2 (magenta) or p53 (green) protein abundance was estimated by quantitative immunoblotting. Data are shown as the mean ± s.e.m. of n = 3 (A) or 4 (B) independent perturbations. (C) Endogenous oxidative stress is associated with NRF2 stabilization in 3D spheroids. MCF10A-5E cells stably expressing HyPer-2 (370) and mRFP1-NRF2 reporter (NRF2rep) were grown as 3D spheroids for 10 days and imaged by laser-scanning confocal microscopy. Representative pseudocolored images for HyPer-2 ratio (upper left) and mRFP1-NRF2 reporter (lower left) are shown. HyPer-2 ratios and mRFP1-NRF2 reporter fluorescence are quantified (right) along with the log-scaled mutual information (MI) with 90% CI for n = 605 cells segmented from 10–25 spheroids from four separate 3D cultures. (D) The antioxidant Trolox suppresses endogenous NRF2–p53 coordination during 3D culture. Representative pseudocolored images for NRF2 (upper left) and p53 (middle left) are shown merged with DAPI nuclear counterstain (lower left). White arrows indicate concurrent NRF2 and p53 stabilization. The log-scaled and background-subtracted MI (right) is shown with 90% CI estimated from n = 1000 bootstrap replicates. (E) Trolox interferes with the synergistic proliferative suppression caused by dual inactivation of NRF2 and p53 in MCF10A-5E cells. Data are shown as the mean percentage of proliferation-suppressed spheroids ± s.e.m. of n = 8 independent 3D-cultured samples after 10 days. The overall effect of Trolox on spheroid size is shown inFigure 4.12. Statistical interaction between Trolox and NRF2–p53 (pint) was assessed by three-way ANOVA with replication. For (D) and (E), MCF10A-5E cells cultured for 10 days in 3D with or without 50 µM Trolox supplemented every two days. Scale bars are 10 µm (C) and 20 µm (D).

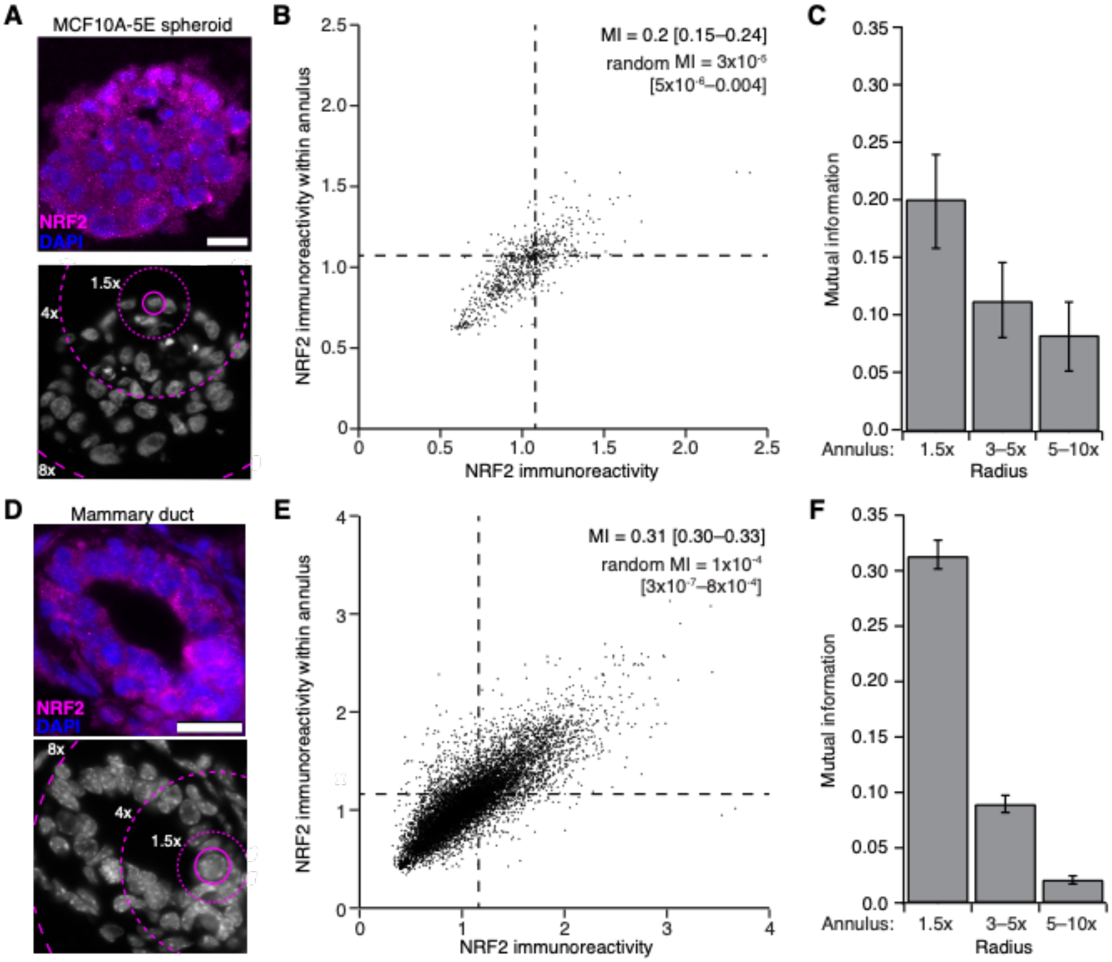

Figure 4.10 Local niches of NRF2 stabilization in MCF10A-5E 3D spheroids and pubertal murine mammary glands.

(A to C) Quantification of neighboring NRF2 stabilization in MCF10A-5E 3D spheroids. (D to F) Quantification of neighboring NRF2 stabilization in murine mammary glands during puberty. In (A) and (D), representative merged images for NRF2 (magenta) with DAPI nuclear counterstain (blue) are shown (top). DAPI stain is shown below with magenta rings defining neighboring annuli used for mutual information (MI) calculations. In (B) and (E), MI is shown between NRF2 staining in single cells and surrounding cells within a radius equal to 1.5x the median cell diameter for n = 737 MCF10A-5E cells and 10316 mammary epithelial cells. In (C) and (E), MI is shown between NRF2 staining in single cells and surrounding cells that fall within annuli of different radius from a single cell. MI is shown with 90% CI estimated from n = 1000 bootstrap replicates.

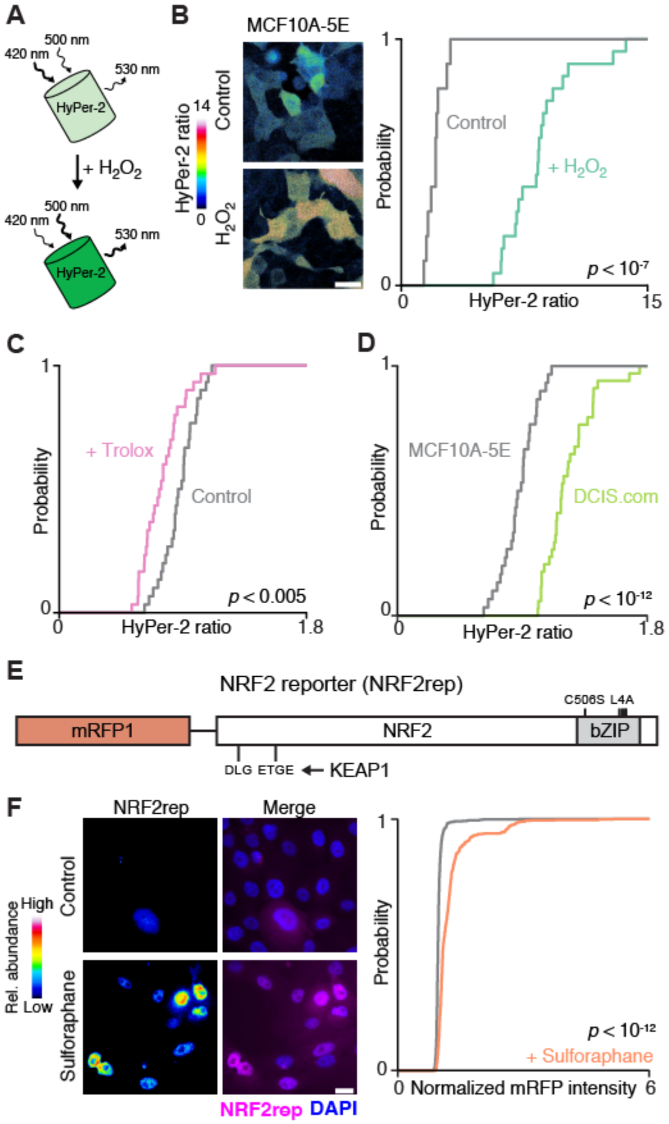

Figure 4.11 Description and validation of the HyPer-2 probe for H_2O_2 and the mRFP1-NRF2 reporter.

(A) Schematic of HyPer-2. Increases in intracellular H_2O_2 cause an increase in 530 nm fluorescence upon excitation at 500 nm and a reduction upon excitation at 420 nm. (B) HyPer-2 fluorescence ratios increase in MCF10A-5E cells treated with 200 μM H_2O_2. (C) HyPer-2 fluorescence ratios are decreased in MCF10A-5E cells cultured with the antioxidant Trolox (50 μM for 48 hours). (D) HyPer-2 fluorescence ratios are significantly elevated in transformed MCF10DCIS.com (DCIS.com) cells compared to MCF10A-5E cells. (E) Schematic of the mRFP1-NRF2 reporter (NRF2rep). NRF2 is fused to mRFP1 at its N-terminus, and the DNA-binding domain is mutated (C506S) along with four leucines (L4A) in the leucine zipper region of the bZIP domain. NRF2rep remains targeted by KEAP1 through its DLG and ETGE binding motifs. (F) NRF2rep increases in MCF10A-5E cells treated with 10 μM sulforaphane for 2 hours. Representative pseudocolored images for NRF2rep (left) are shown merged with DAPI nuclear counterstain (right). For (B) to (D) and (F), HyPer-2 fluorescence ratios and mRFP1-NRF2 fluorescence are summarized as cumulative density plots. Scale bars are 20 μm.

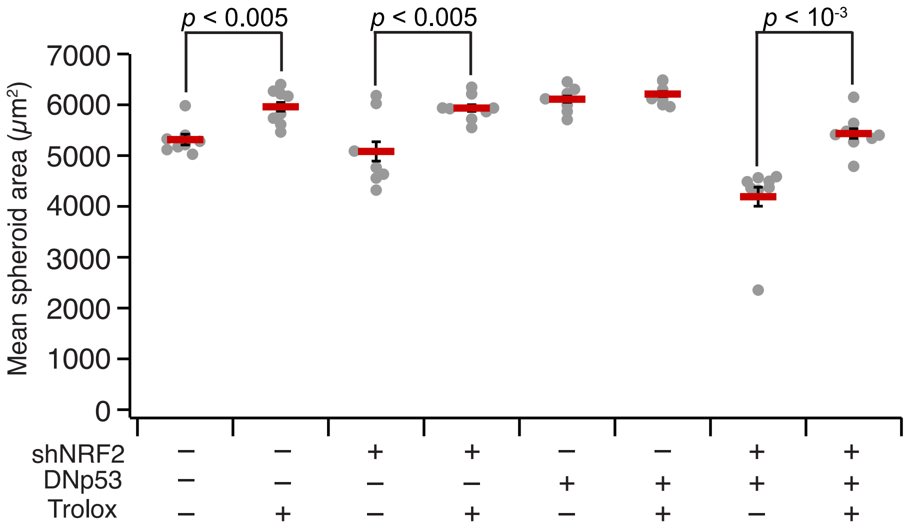

Figure 4.12 Antioxidant treatment causes an overall increase in MCF10A-5E spheroid size.
MCF10A-5E cells were treated with 50 μM Trolox for two days before 3D culture, and Trolox was included in media refeeds and supplemented every two days between refeeds. Data are shown as the mean ± s.e.m. of n = 8 independent 3D-cultured samples after 10 days.

4.3.4 NRF2–p53 co-regulation occurs in normal breast tissue and hormone-negative DCIS but not invasive TNBC

The regulatory heterogeneities observed in 3D culture often reflect adaptations in hormone-negative premalignancy (333) that become further disrupted in TNBCs (334). We thus sought to quantify NRF2–p53 coordination in TNBC and premalignant DCIS lesions, using adjacent-normal tissue as a comparator. The *TP53* gene is frequently mutated in TNBC (33) and gives rise to loss of p53 protein or hyperstabilization of a dominant-negative mutant in tumors (371). By contrast, prior immunohistochemistry of NRF2 abundance in breast carcinomas was inconclusive (372), owing to an anti-NRF2 antibody that was later shown to be non-specific (373). There was an opportunity to revisit NRF2–p53 abundance heterogeneities from the perspective of co-stabilization, with a focus on TNBC and its precursor lesions. Using a knockout-verified commercial antibody (374), we immunoblotted with our production lot and confirmed detection of basal and induced NRF2 with only ~35% immunoreactivity attributed to nonspecific bands (Figure 4.13, A to C). By immunohistochemistry, the antibody detected endogenous NRF2 stabilized with electrophiles in paraffin sections of cell pellets (Figure 4.13D). The antibody has also been used independently to track NRF2 abundance in other solid tumors. However, when we stained adjacent-normal epithelium immunohistochemically, NRF2 was not clearly discernible (Figure 4.14A, upper). In MCF10A 3D spheroids, stabilized p53 is not detected by immunohistochemistry either (375), and yet we readily visualized it by immunofluorescence (Figure 4.3B). Therefore, to improve signal-to-background and facilitate multiplex quantification, we used two-color immunofluorescence after antigen retrieval, segmenting 24,949 normal and transformed epithelial cells in 15 cases of TNBC and hormone-negative DCIS.

In adjacent-normal epithelium, we observed local niches of stabilized NRF2 in lobules and ducts, which often corresponded with stabilized p53 (Figure 4.14A, lower, and 4.15).

Stabilized NRF2 was frequently detected in the cytoplasm, consistent with the prolonged cytoplasmic localization observed in H_2O_2-treated cells compared to cells stressed with an electrophile (Figure 4.16). The results corroborated recent findings that KEAP1 senses oxidative stress differently than electrophilic stress (71). The patterns of NRF2–p53 co-accumulation were largely preserved in hormone-negative DCIS (Figure 4.14B and 4.17A), even in cases with hyperstabilized p53 that was likely mutated (see below). Nuclear localization of NRF2 was also more prominent, perhaps reflecting the stronger ROS generation rates of transformed cells (376). Strikingly, NRF2 and p53 were almost completely uncoupled in invasive TNBCs (Figure 4.14 and 4.17), reflecting a profound shift in single-cell regulation. We quantified NRF2–p53 coordination by mutual information and found that it was largely eliminated in regions of invasive TNBC, irrespective of whether p53 was chronically stabilized or not (Figure 4.14D). Such alterations were not apparent in regional estimates of protein abundance by cell population-averaged fluorescence, where neither NRF2 nor p53 were reproducibly different among groups (Figure 4.14E,F). We conclude that 3D culture in reconstituted basement membrane co-stimulates the NRF2–p53 pathways akin to that observed in normal breast tissue and hormone-negative premalignancy. Full-blown TNBC, by contrast, evokes a different set of dependencies.

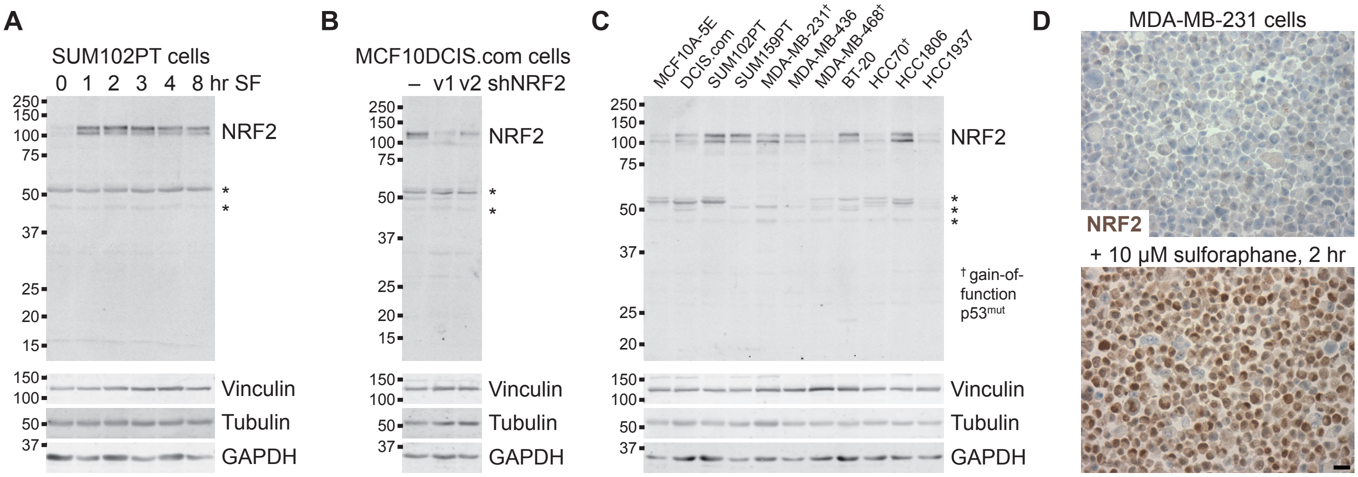

Figure 4.13 Anti-NRF2 antibody validation for immunohistochemistry.
(A) NRF2 is the predominant band induced with the electrophile sulforaphane (SF) in SUM102PT cells. Similar results were obtained with various cell lines. (B) Specificity of the ~100 kDa NRF2 immunoreactive band confirmed by shRNA-mediated knockdown in MCF10DCIS.com cells. Similar results were obtained with various cell lines. (C) NRF2 abundance varies across triple-negative cell lines. Breast cancer lines with gain-of-function p53 are indicated (†). (D) Increased immunohistochemical staining in MDA-MB-231 cell pellets treated with sulforaphane as indicated. Scale bar is 20 µm. For (A) to (C), asterisks indicate minor nonspecific bands that are likely denaturation-induced epitopes based on the staining of control cell pellets in (D).

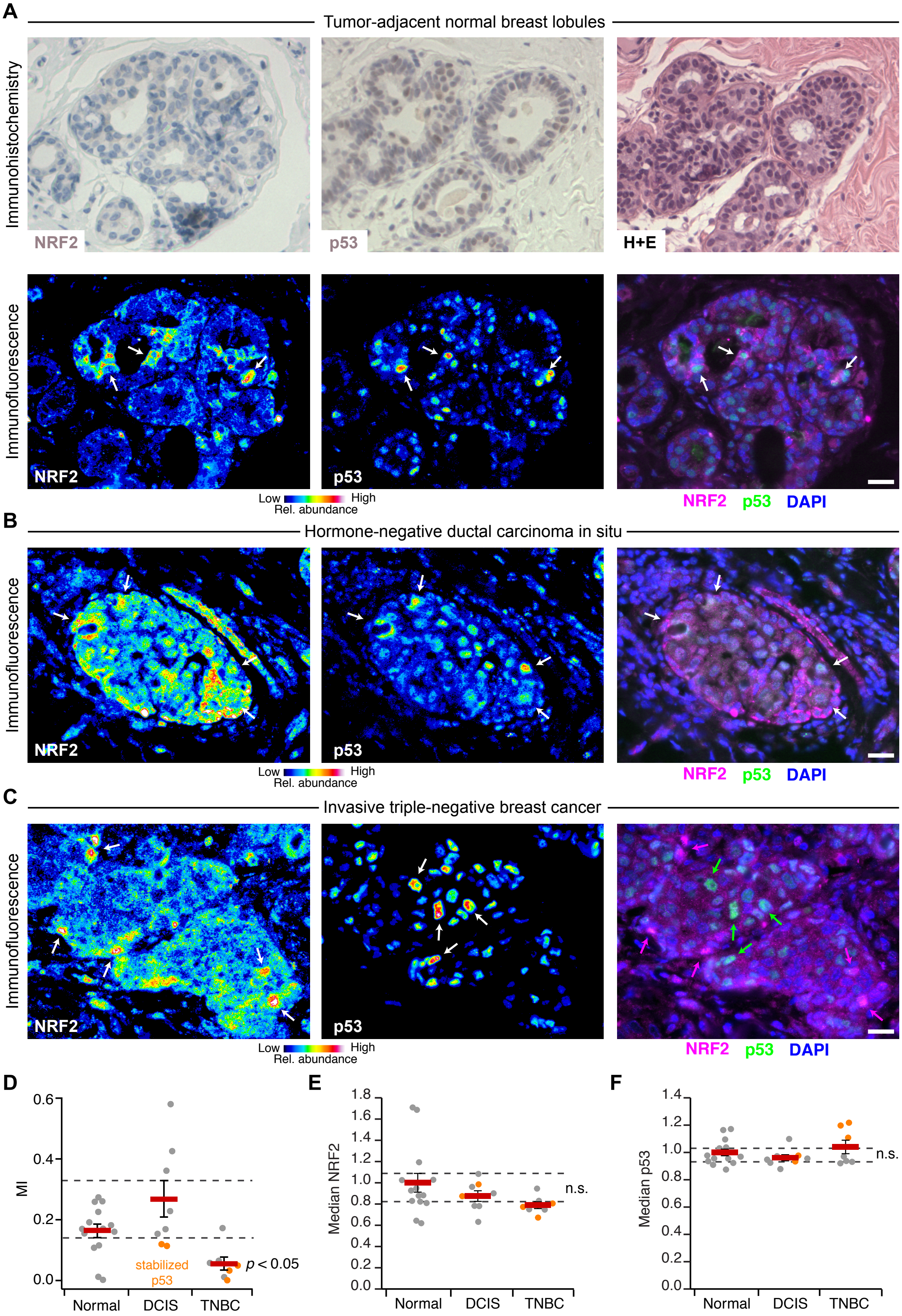
A
Tumor-adjacent normal breast lobules
Immunohistochemistry
NRF2
p53
H+E
Immunofluorescence
NRF2
p53
Low
High
Rel. abundance
NRF2 p53 DAPI
B
Hormone-negative ductal carcinoma in situ
Immunofluorescence
NRF2
p53
Low
High
Rel. abundance
NRF2 p53 DAPI
C
Invasive triple-negative breast cancer
Immunofluorescence
NRF2
p53
Low
High
Rel. abundance
NRF2 p53 DAPI
D
MI
0.6
0.4
0.2
0.0
stabilized p53
$p < 0.05$
Normal
DCIS
TNBC
E
Median NRF2
1.8
1.6
1.4
1.2
1.0
0.8
0.6
0.4
0.2
0.0
n.s.
Normal
DCIS
TNBC
F
Median p53
1.4
1.2
1.0
0.8
0.6
0.4
0.2
0.0
n.s.
Normal
DCIS
TNBC

Figure 4.14 NRF2 and p53 are co-stabilized in breast epithelial tissue and premalignant lesions but uncoupled in triple-negative breast cancer.

(A) Immunohistochemistry (upper) and immunofluorescence (lower) for NRF2 and p53 in tumor-adjacent normal breast lobules. Hematoxylin and eosin (H+E, upper right) histology is from a serial paraffin section for p53. Images from a tumor-adjacent normal breast duct are shown in Figure 4.15 (B and C) Multicolor immunofluorescence for NRF2 and p53 in (B) hormone-negative ductal carcinoma in situ and (C) triple-negative breast cancer. (D) NRF2–p53 mutual information (MI) is lost in triple-negative breast cancer. (E and F) Overall NRF2 and p53 immunoreactivity is not consistently altered during triple-negative breast cancer progression. n.s., not significant ($p > 0.05$). For (A) to (C), immunofluorescence is shown as representative pseudocolored images for NRF2 (left) and p53 (middle) are shown merged with DAPI nuclear counterstain (right). White arrows indicate concurrent NRF2 and p53 stabilization, and magenta or green arrows indicate stabilization of NRF2 or p53 separately. Scale bars are 20 μm. For (D) to (F) data are shown as the mean ± s.e.m. of n = 14 cases with tumor-adjacent normal epithelium (Normal), 8 cases with ductal carcinoma in situ (DCIS), and 7 cases of triple-negative breast cancer (TNBC).

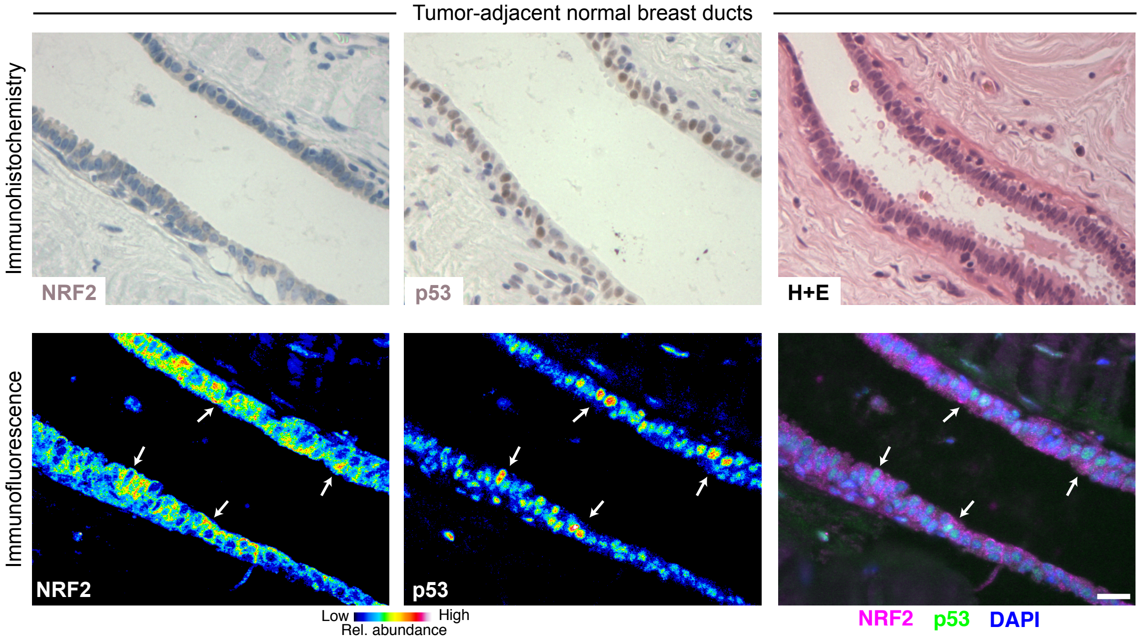

Figure 4.15 NRF2 and p53 are co-stabilized in breast epithelial ducts.
Immunohistochemistry (upper) and immunofluorescence (lower) for NRF2 and p53 in tumor-adjacent normal breast ducts. Hematoxylin and eosin (H+E, upper right) histology is from a serial paraffin section for p53. Immunofluorescence is shown as representative pseudocolored images for NRF2 (left) and p53 (middle) are shown merged with DAPI nuclear counterstain (right). White arrows indicate concurrent NRF2 and p53 stabilization. Scale bar is 20 μm.

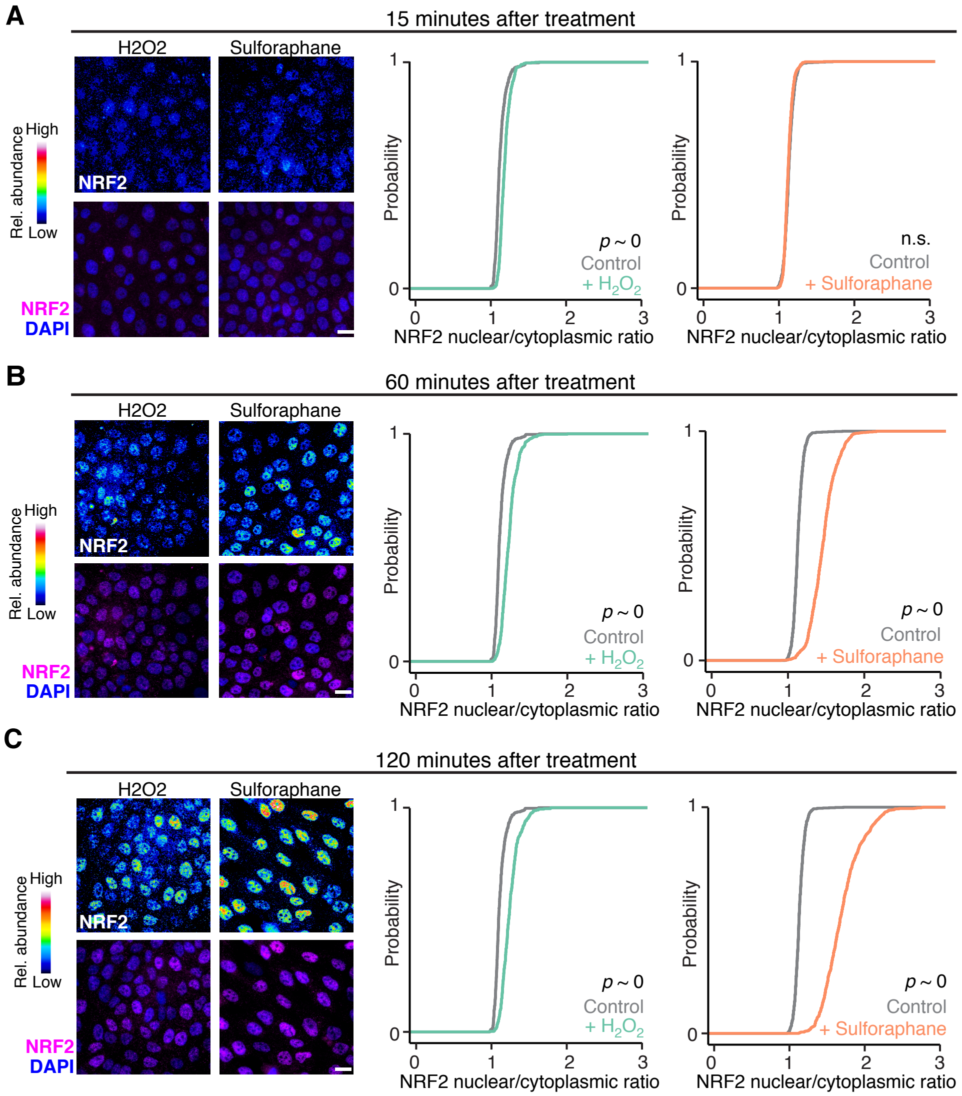

Figure 4.16 Oxidative stress stabilizes NRF2 in the cytoplasm more so than electrophilic stress.

(A to C) Time course of NRF2 stabilization in MCF10A-5E cells were treated with 200 μM H_2O_2 or 10 μM sulforaphane for the indicated times and analyzed by immunofluorescence for NRF2 from n = 400–800 cells per time point. For each subpanel, representative pseudocolored images for NRF2 are shown on the top and merged with DAPI nuclear counterstain on the bottom. Scale bar is 20 μm. Cytoplasmic and nuclear NRF2 immunoreactivity is summarized as cumulative density plots.

4.4 Discussion

Our results posit ROS as an endogenous, spatially heterogeneous trigger of dual NRF2–p53 activation in breast–mammary epithelia surrounded by basement membrane ECM. NRF2 and p53 regulate target-gene abundance—both cooperatively and independently—to promote stress tolerance and adaptation. NRF2 deficits are buffered by compensatory increases in p53 signaling, and dramatic ROS-dependent phenotypes arise when both pathways are perturbed. In hormone-negative premalignant lesions, stabilization of NRF2–p53 remains coordinated, even in cases where p53 has likely mutated. At this preinvasive stage, NRF2–p53 coordination should be most important for tumorigenesis. After invasion through basement membrane and progression to TNBC, the stromal microenvironment reduces overall NRF2 signaling and uncouples it from (now-mutant) p53. Our results describe a robust stress-responsive network important for mammary gland morphogenesis and the early stages of breast cancer.

The mammary gland is unique in its regenerative capacity, with the majority of development happening postnatally. Breast tissue goes through numerous cycles of proliferation and reorganization throughout puberty and lactation, requiring many mechanisms essential for tumor formation such as invasion (312), reinitiation of proliferation (377), resistance to apoptosis (378), and angiogenesis (379). Therefore, it is of no surprise that breast cancer cells reengage cellular programs normally used during development. The coordination of NRF2 and p53 in cell culture models and clinical cases of DCIS (Figure 4.7A and 4.14D) provides one example of a normal glandular development processes repurposed by premalignant cells to survive stresses associated with transformation. Other examples of this phenomenon include premalignant breast cells using autophagy, a protective mechanism activated during normal alveolar formation (380), to survive anoikis within the hypoxic, nutrient-deprived intraductal environment (381–383). In fact, NRF2 transcriptionally regulates the autophagy substrate p62 (384) and induces autophagy in response to oxidative stress in multiple disease contexts including breast cancer (385–387), suggesting that multiple NRF2-regulated processes can be useful during premalignancy.

Our work begins to uncover a group of genes jointly regulated by NRF2 and p53. Compound perturbation of NRF2 and p53 caused non-additive changes in multiple transcripts in the NRF2-associated gene cluster, including *CDKN1A* and *KRT5* (Figure 4.3D), suggesting complex regulation by the two stress-responsive transcription factors. *CDKN1A*, the canonical p53 target gene (388), also contains an NRF2 binding site in its promoter region (389), providing further evidence of its dual regulation. Regulation of the cyclin-dependent kinase inhibitor (p21) by multiple stress-responsive pathways is advantageous, as it provides multiple checks before a cell commits to senescence (122). Evidence of *KRT5* transcriptional regulation by p53 (390,391), but not NRF2, exists in the literature. Our findings suggest that the basal-like cytokeratin could be important for stress tolerance, as has been shown for other keratins (392,393). Further research to identify genes dually regulated by NRF2 and p53 could define a core genetic program important for the oxidative stress response in breast epithelial cells.

NRF2's role as master transcriptional activator of hundreds of enzymes that detoxify oxidative and electrophilic stressors make the pathway distinctly important for handling oncogenesis-associated cellular stresses. It would seem that targeting the pathway could re-sensitize cancer cells to their environment and make them more susceptible to stress-induced apoptosis. However, NRF2 pathway perturbation in breast cancer cells has yielded conflicting results in the literature, in which both NRF2 stabilization (394,395) and NRF2 inhibition (396,397) has suppressed growth and migration of cancer cells. Our results suggest that the effects of NRF2 pathway targeting will vary based on tumor stage, as suggested elsewhere (105), and is unpredictable based on NRF2 levels alone (Figure 4.14E).

Cancer mutations engage and cooperate with cell signaling in ways that are not captured by DNA sequencing (398). The coupling of the NRF2 and p53 pathways described here provides a robust oxidative stress-handling network for glandular morphogenesis and maintenance. But, this same coupling creates a redundancy upon which p53 mutations can occur and neoplasms can evolve. Our results give pause to the nutraceutical use of sulforaphane as a potent NRF2 stabilizer (395)—in lung cancer, where KEAP1–NRF2 mutations are common and *TP53* is secondary, antioxidants accelerate tumor progression (399). Effective therapeutic targeting will require a holistic evaluation of NRF2 signaling in relation to p53 and other tumor suppressors and oncogenes that impinge on the pathway.

4.5 Materials and methods

4.5.1 Plasmids

shRNA targeting sequences from the RNAi consortium (400) were cloned into tet-pLKO.1-puro as previously described (343) for shLuc (TRCN0000072250, Addgene #136587), shNRF2 #1 (TRCN0000281950, Addgene #136584), shNRF2 #2 (TRCN0000284998, Addgene #136585), shJUND #1 (TRCN0000416347, Addgene #136581), shJUND #2 (TRCN0000416920, Addgene #136583).

For the mRFP1-NRF2 reporter (Addgene #136580), the DNA binding domain of NRF2 was mutated (C506S) along with four leucines (L4A) in the leucine zipper region of the bZIP domain by site-directed mutagenesis of the pBabe mRFP1-NRF2 hygro plasmid (Addgene #136579) originally prepared by subcloning into pBabe mRFP1 hygro. The RNAi-resistant (RR) version of NRF2 (Addgene #136522) was prepared by introducing four silent mutations into the sequence targeted by shNRF2 #1 in pEN_TT 3xFLAG-NRF2 (Addgene #136527). Site-directed mutagenesis was performed with the QuikChange II XL kit (Agilent).

pDONR223 CHEK2 was obtained from the human Orfeome V5.1 (401). CHEK2 amplicon was prepared with XbaI and MfeI restriction sites and cloned into pEN_TTmiRc2 3xFLAG (Addgene #83274) that had been digested with SpeI and MfeI (Addgene #136526). BirA* was cloned out of pcDNA3.1 mycBioID (Addgene) (402) with XbaI and SpeI restriction sites and cloned into pEN_TTmiRc2 digested with SpeI and Mfe1 (Addgene #136521). CDKN1A and NRF2 PCR amplicons were prepared with SpeI and MfeI restriction sites and cloned into pEN_TTmiRc2 BirA* (Addgene #136521). Luciferase PCR amplicon was prepared with SpeI and EcoRI restriction sites and cloned into pEN_TTmiRc2 3xFLAG digested with SpeI and MfeI sites (Addgene #136519). p53DD (p53DN) and p53(R280K)-V5 PCR amplicon was prepared with SpeI and MfeI restriction sites and cloned into pEN_TTmiRc2 (Addgene #25752) digested with SpeI and MfeI (Addgene #136520, #136525).

pEN_TT donor vectors were recombined into pSLIK neo (Addgene #25735), pSLIK zeo (Addgene #25736), or pSLIK hygro (Addgene #25737) by LR recombination to obtain pSLIK 3xFLAG-Luciferase zeo (Addgene #136533), pSLIK p53DD zeo (Addgene #136534), pSLIK 3xFLAG-Luciferase hygro (Addgene #136528), pSLIK 3xFLAG-NRF2(RR) hygro (Addgene #136535), pSLIK BirA* hygro (Addgene #136537), pSLIK BirA*-CDKN1A hygro (Addgene #136538), pSLIK BirA*-NRF2 hygro (Addgene #136539), pSLIK p53(R280K)-V5 hygro (Addgene #136540) and pSLIK 3xFLAG-CHEK2 neo (Addgene #136536).

pLXSN HPV16E7 (403) and the ΔDLYC mutant (Addgene #136588) were provided by Scott Vande Pol. pCDH-Hyper2-puro (369) was provided by Joan Brugge.

4.5.2 Cell lines

The MCF10A-5E clone was previously reported and cultured as described for MCF-10A cells (323,330). MCF10DCIS.com cells were obtained from Wayne State University and cultured in DMEM/F-12 medium (Gibco) plus 5% horse serum (Gibco). SUM102PT cells were obtained from Asterand Biosciences and cultured in Ham's F-12 (Gibco) plus 10 mM HEPES (Gibco), 10 ng/ml epidermal growth factor (Peprotech), 5 mM ethanolamine (Sigma), 50 nM sodium selenite (Sigma), 5 µg/ml apo-Transferrin (Sigma), 10 nM Triiodo-L-Thyronine (VWR), 5 µg/ml insulin (Sigma), 1 µg/ml hydrocortisone (Sigma), and 5% fatty acid free bovine serum albumin (VWR). All cell lines are female, were grown at 37°C, authenticated by short tandem repeat profiling by ATCC, and confirmed negative for mycoplasma contamination.

4.5.3 Viral transduction and selection

Lentiviruses were prepared in human embryonic kidney 293T cells (ATCC) by triple transfection of the viral vector with psPAX2 + pMD.2G (Addgene) and transduced into MCF10A-5E, MCF10DCIS.com, HCC1937, SUM159PT, MDA-MB-231, HCC1806, and MDA-MB-468 as previously described (334). Retroviruses were prepared similarly by double transfection of the viral vector with pCL ampho (Addgene) and transduced into MCF10A-5E cells as previously described (331). Transduced cells were selected in growth medium containing 2 μg/ml puromycin, 300 μg/ml G418, 100 μg/ml hygromycin, or 25 μg/ml zeocin until control plates had cleared. For RNAi-resistant addback, viral titers were adjusted to match the endogenous protein abundance as closely as possible. For mRFP1-NRF2 fluorescent reporter, we used the minimum viral titer that gave sufficient signal in sulforaphane-treated cells compared to DMSO-treated cells.

4.5.4 3D culture

3D overlay cultures were performed on top of Matrigel (BD Biosciences) as described previously for MCF-10A cells (404) with culture media previously optimized for each cell line (334). For each culture, 45 μl of Matrigel was spread with a pipette tip on the bottom of an 8-well chamber slide. A suspension of 5000 single cells per well was laid on top of the Matrigel in culture media supplemented with 2% Matrigel. 3D culture medium was replaced every four days as originally described (404). For antioxidant supplementation, cells were treated with 50 μM Trolox (Calbiochem) for two days before 3D culture, and Trolox was included in media refeeds and supplemented every two days between refeeds. For long-term knockdown experiments, cells were treated with 1 μg/ml doxycycline (Sigma) for three days before 3D culture, and doxycycline was maintained in the 3D culture medium throughout the experiment. For experiments with long-term knockdown and inducible overexpression, cells were treated with 1 μg/ml doxycycline for two days before 3D culture, and doxycycline was maintained in the 3D culture medium throughout the experiment.

4.5.5 RNA purification

RNA from cultured cells was isolated with the RNeasy Plus Mini Kit (Qiagen) according to the manufacturer’s protocol. RNA from 3D cultures at day 10 was extracted by lysing individual wells in 500 μl RNA STAT-60 (Tel-Test) and purified as described previously (334).

4.5.6 RNA sequencing and analysis

Total RNA was diluted to 50 ng/µl and prepared using the TruSeq Stranded mRNA Library Preparation Kit (Illumina). Samples were sequenced on a NextSeq 500 instrument with NextSeq 500/550 High Output v2.5 kits (Illumina) to obtain 75-bp paired-end reads at an average depth of 15 million reads per sample. Adapters were trimmed using fastq-mcf in the EAutils package (version ea-utils.1.1.2-537) with the following options: -q 10 -t 0.01 -k 0 (quality threshold 10, 0.01% occurrence frequency, no nucleotide skew causing cycle removal). Quality checks were performed with FastQC (version 0.11.7) and multiqc (version 1.5). Datasets were aligned to the human (GRCh38.86) genome using HISAT2 with the option: --rna-strandness RF (for paired end reads generated by the TruSeq strand-specific library). Alignments were assembled into transcripts using Stringtie (version 1.3.4) with the reference guided option. Transcripts that were expressed at greater than five transcripts per million across all samples were retained for downstream analysis. Differential gene expression analysis was carried out using edgeR (version 3.8) (405) on raw read counts corresponding to transcripts that passed the abundance-filtering step. Trimmed Mean of M-values normalization (TMM) normalization using the calcNormFactors function was done before differential expression analysis using exactTest in edgeR. The 1,132 transcripts that were commonly differentially expressed (5% FDR) between MCF10A-5E shControl and shNRF2 #1, shControl and shNRF2 #2, and MCF10DCIS.com shControl and shNRF2 #1 are shown in Figure 4.7B. Gene Set Enrichment Analysis was done on transcripts that were differentially upregulated or downregulated in shNRF2 compared to shControl using the Molecular Signatures database collections C1-C4, C6, C7 (406,407).

4.5.7 Quantitative PCR

cDNA synthesis and quantitative PCR were performed as previously described (334,408). Human samples were normalized to the geometric mean of ACTB, HINT1, PP1A, and TBP (Figures 4.3D and 4.2C); B2M, GAPDH, GUSB, HINT1, PRDX6 (Figure 4.2A); or ACTB, B2M, GUSB, PPIA, PRDX6 (Figure 4.2B).

4.5.8 Brightfield imaging and quantification of spheroid phenotypes

Brightfield 3D images were acquired on an Olympus CKX41 inverted microscope with a 4× Plan objective (four fields per chamber) and a qColor3 camera (Qimaging). Images were segmented using OrganoSeg (409) to produce morphometric measures for each segmented spheroid. 'Rounded' spheres were classified as having circularity greater than 0.9 (Figures 4.7, C,E, and 4.8 B,C). 'Hyper-enlarged' spheres were classified as having an area greater than $e^{8.5}$ ~ 5000 μm^2 (Figure 4.7 D,E). 'Proliferation suppressed' spheres were classified as having an area less than 1600 μm^2 for MCF10A-5E cells after 10 days of 3D culture (Figures 4.3E and 4.9E).

4.5.9 Clinical samples

Cases were identified from the pathology archives at the University of Virginia and build upon a cohort of samples previously described (333,334). Hormone-negative DCIS lesions were deemed negative (less than 10% expression frequency) for estrogen receptor and progesterone receptor by clinical immunohistochemistry, and TNBC cases were additionally scored negative for HER2 amplification by clinical DNA chromogenic in situ hybridization. All clinical work was done according to IRB-HSR approval #14176 and PRC approval #1363 (502-09).

4.5.10 Immunofluorescence

MCF10A-5E and MCF10DCIS.com 3D cultures were embedded at day 10 of morphogenesis, and 5-μm sections were cut and mounted on Superfrost Plus slides (Fisher). For clinical samples, paraffin tissue sections were dewaxed and antigens retrieved on a PT Link (Dako) with low-pH EnVision FLEX Target Retrieval Solution (Dako) for 20 min at 97°C. Immunofluorescence on cryosections and antigen-retrieved slides was performed as previously described (330) with the following primary antibodies: NRF2 (Santa Cruz #sc-13032, 1:100), phospho-Rb (Cell Signaling #8516, 1:1600), p53 (Santa Cruz #sc-126, 1:200). Slides were incubated the next day for 1 hr in the following secondary antibodies: Alexa Fluor 555-conjugated goat anti-rabbit (1:200; Invitrogen), Alexa Fluor 647-conjugated goat anti-mouse (1:200; Invitrogen).

4.5.11 Image acquisition–analysis and mutual information calculation

Fluorescent images were collected on an Olympus BX51 fluorescence microscope with a 40× 1.3 numerical aperture (NA) UPlanFL oil-immersion objective and an Orca R2 CCD camera (Hamamatsu) with no binning. Images were segmented in CellProfiler (258) using DAPI to identify nuclei. Nuclear objects were dilated to a median diameter of 15 µm to capture approximately one whole cell. NRF2 staining was quantified in the nucleus, the whole cell, and the cytoplasm (whole cell area – nuclear area). p53 and pRB staining was quantified in the whole cell. Immunoreactivity was quantified as the median fluorescence intensity of the whole cell unless otherwise noted.

For pRB and NRF2 immunofluorescence (Figure 4.11 D,E), log-transformed distributions were analyzed with the MClust function in R using the unequal variance model with either one or two mixture components specified. Model fit was evaluated by F test.

MCF10A-5E cells stably expressing pCDH-HyPer2-puro were imaged at 37°C in Hank's Balanced Salt Solution (Gibco) with a 40× 1.3 NA EC Plan Neofluar oil-immersion objective on a Zeiss LSM 700 laser scanning confocal microscope. 405 nm and 488 nm lasers were used to sequentially excite two excitation peaks of HyPer-2 and collect fluorescence emission from 500–550 nm. To calculate HyPer-2 ratios on a pixel-by-pixel basis, 488-nm images were divided by 405-nm images and thresholded in ImageJ to remove background pixel values (~10%). For quantification of cells cultured in 2D (Figure 4.11, B to D), the mean HyPer-2 ratio per image was used for analysis. For quantification of cells cultured as spheroids (Figure 4.9C), cells were manually segmented to calculate the median HyPer-2 ratio per cell.

Clinical samples were imaged on an Olympus BX51 fluorescence microscope with a 40× 1.3 NA UPlanFL oil-immersion objective and an Orca R2 CCD camera (Hamamatsu) with 2×2 binning and fixed exposure times for NRF2 (150 msec) and p53 (50 msec). Images were autoexposed in the DAPI channel for nuclear segmentation and in the unlabeled FITC channel for autofluorescence estimation. Image fields were classified as follows: Normal—bilayered epithelium, intact basement membrane (visualized by FITC autofluorescence), and normal cytoarchitecture; DCIS—multilayered and disorganized epithelium (with partial or complete luminal filling), intact basement membrane, cytologic atypia; TNBC—invasive carcinoma cells with cytologic atypia and no discernable basement membrane. All images were segmented in CellProfiler as described above. After nuclear identification, nuclei outside of the ductal epithelium (fibroblasts, endothelial cells, and immune cells) were manually removed using the IdentifyObjectsManually module. Because paraffin fixation of tissue increases autofluorescence (410), the analysis excluded images that were dominated by autofluorescent bleedthrough into the Alexa 555 channel localizing NRF2. Spearman correlation was calculated between cellular FITC–555 channels and FITC–DAPI channels on a pixel-by-pixel basis for each image. Images with a FITC–555 correlation coefficient above the 95th percentile for FITC–DAPI correlation (in which autofluorescent artifacts were negligible due to the low exposure time) were excluded from further analysis.

For NRF2 quantification in neighboring cells (Figure 4.10), spheroid and mouse mammary gland images were loaded into CellProfiler and the IdentifyObjectManually module was used to manually identify regions of ductal epithelium. The images were cropped manually, and cell nuclei within the cropped area were identified by DAPI staining. Nuclear area was dilated to a median diameter of ~15 μm to define a cell. Position, area, and median NRF2 staining intensity were measured for each cell. Measurements were loaded into MATLAB, and single-cell NRF2 intensities were normalized to the median intensity of all exposure-matched cells. Neighboring cells were defined as cells located within a radius of 1.5 times the median cell diameter. For more distant neighbors, annular areas of 3–5 and 5–10 times the median cell diameter were used. Cells that fell within the applied search area were used to calculate the median neighbor NRF2 intensity. The original cell at the center of the search area was not included in the intensity calculations, and cells with NRF2 intensity values equal to 0 or lacking neighboring cells within the defined search area were excluded from calculations.

To quantify the association between fluorescence channels, we used mutual information in lieu of standard correlation measures (Pearson, Spearman). After appropriate transformation and binning into discrete high-low states, mutual information provides greater flexibility to capture nonlinear relationships (411) and more stringency to detect compressions in dynamic range (412). Median fluorescence intensity distributions were transformed by their respective cumulative distribution functions (probability integral transform) to produce uniformly distributed random variables (413). The uniform distributions were split into low and high states at the 67th percentile, and the joint–marginal state probabilities estimated for the two fluorescence channels (R, G) were used to calculate the mutual information (MI) as follows:

$$MI = \sum \sum p_{RG} log \frac{p_{RG}}{p_R p_G}$$

MI confidence intervals were estimated by bootstrapping the segmented cell population 1000 times. To create a randomized (null) dataset, the values of one fluorescence channel were randomly shuffled before analysis.

Clinical samples often had fewer areas of classified cells for imaging, which require an added analysis step in the mutual information calculation. For a classification (normal, DCIS, TNBC) comprised of two images from one case, we evaluated batch effects by hypergeometric test to determine if the two images separated by high-vs.-low staining intensity. If so, the case for that classification was excluded.

4.5.12 Quantitative immunoblotting

Quantitative immunoblotting was performed as previously described (334). Primary antibodies recognizing the following proteins or epitopes were used: NRF2 (Santa Cruz Biotechnologies, #sc-13032, 1:1000), p53 (Santa Cruz Biotechnology #sc-126, 1:1000), p21 (Proteintech #10355-1-AP, 1:1000), total Chk2 (Cell Signaling #2662, 1:1000), GAPDH (Ambion #AM4300, 1:20,000), tubulin (Abcam #ab89984, 1:20,000), p38 (Santa Cruz Biotechnology #sc-535, 1:5000), Hsp90 (Santa Cruz Biotechnology #sc-7947, 1:5000).

4.5.13 Promoter bioinformatics

The 36 transcripts of the Figure 4.1A gene cluster (20, 24) were assessed with four promoter analysis algorithms to identify recurrent transcription factor (TF) candidates (242). First, distant regulatory elements (DiRE) analysis was conducted using the DiRE website (https://dire.dcode.org) (345) searching evolutionary conserved 5’ untranslated regions (5’ UTR ECRs) and promoter regions (promoter ECRs) for genes on the human genome (hg18). A random set of 7500 genes was selected as background control genes. Second, Expression2Kinases (X2K) software was used to identify upstream TFs for the Figure 4.1A gene cluster (41). The potential TFs were selected from ChIP-X Enrichment Analysis (ChEA) database using “mouse + human” as the background organisms (414). The p value from the Fisher Test and Z-score were used for sorting and ranking. Third, from the National Center for Biotechnology Information (NCBI), we collected the proximal promoter of each transcript—defined as 1416 base pairs (bp) upstream and 250 bp downstream of the transcription start site to remain within the 60 kb sequence limit—for use as an input set for MEME (415,416). Using MEME-defined motifs from classic discovery mode, the top three enriched motifs were searched against the JASPAR CORE (2018) database (containing 1404 defined TF binding sites for eukaryotes) (417) or HOCOMOCO Human (v11) database (containing 769 TF binding motifs) (418) using TOMTOM (125) to identify transcription factor recognition sequences. Last, oPOSSUM (43) was used to identify potential TFs targeting transcripts in the cluster. We selected Single Site Analysis – Human mode and used all 24,752 genes in the oPOSSUM database as a background. All vertebrate profiles with a minimum specificity of 8 bits in the JASPAR CORE Profiles were selected as TF binding sites sources. oPOSSUM was run with the following parameters: conservation cutoff of 0.4, matrix score threshold of 85%, amount of upstream/downstream sequence: 2000/0, and sort results by Fisher score.

Chapter 5 Integrated systems modeling of NRF2–p53 oxidative stress handling

5.1 Abstract

In Chapter 3, we used experimental methods to examine the regulation of a stress tolerance transcriptional state in breast epithelial 3D spheroids. We found the state to be jointly coordinated by the antioxidant response regulator, NRF2, and the tumor suppressor, p53, in response to spontaneous oxidative stress. NRF2–p53 signaling remains coordinated in 3D spheroid models and clinical cases of ductal carcinoma in situ, but becomes uncoupled when cells invade into the surrounding mesenchyme in triple-negative breast cancer. In this chapter, we fuse together separate computational models of NRF2 and p53 regulation to create an integrated systems model of oxidative-stress handling. The integrated model captures NRF2–p53 coordination and the oxidative-stress capacity of cells with disrupted NRF2 or p53 seen experimentally. For triple-negative breast cancer lines, of which almost all have mutated p53, model predictions of stress tolerance coincide with 3D-growth phenotypes when NRF2 is perturbed. This work builds a simple network model that allows for abstraction to different genetic and transcriptomic backgrounds to make clinically relevant predictions about the oxidative stress capacity of TNBC tumors.

5.2 Introduction

Reactive oxygen species (ROS) play a complex role in cancer initiation, progression, and treatment. ROS can act as carcinogens by damaging nucleic acids (8,419,420) and have been shown to increase cancer cell proliferation and metastasis (421,422). In contrast, ROS can also induce cancer cell senescence and apoptosis (93) and lowering ROS levels through endogenous antioxidant signaling can promote tumorigenesis (376,423). Perhaps a reason for this paradox is the dual nature of ROS as a damaging oxidant but also a secondary messenger for intracellular signaling (421,424). The extent to which ROS play a tumor-promoting or tumor-suppressing role is both context- and dose-dependent (425), and thus hard to predict.

Despite the uncertainty regarding the effects of ROS on cancer cells, ROS are undoubtedly linked to tumorigenesis. Many of the processes involved in transformation, such as survival of extracellular matrix detachment, increased metabolic activity, and oncogene activation cause increased ROS generation (11,426). Cancer cells have developed numerous strategies to survive higher levels of oxidative stress, including developing an enhanced, endogenous antioxidant response.

Previously, we found that two stress-responsive transcription factors, NRF2 and p53, are coordinately activated by spontaneous oxidative stress encountered by normal and premalignant breast epithelial cells. Premalignant breast epithelial cells engaged the NRF2–p53 network more frequently than normal cells due to their increased ROS levels (Figures 4.3B, 4.7A, 4.9, 4.11D). Perturbing both pathways led to dramatic, ROS-dependent phenotypes of normal and premalignant cells grown in basement membrane (Figures 4.3E and 4.7E). In triple-negative breast cancer (TNBC) tissue, NRF2–p53 coordination was significantly reduced regardless of p53 mutation status (Figure 4.14D). These results suggested that oxidative stress handling by the coordinated response of NRF2 and p53 is essential during the early stages of hormone-negative breast cancers.

To more robustly test the connections between NRF2, p53, and oxidative stress in multiple non-transformed and transformed settings, we set out to build a computational systems model of NRF2–p53 signaling. We use elements from separate models of NRF2 and p53 signaling in the literature to build a fused network model activated by oxidative stress. After calibrating based on quantitative protein measurements of various pathway species, the model recapitulates relative pathway coordination observed experimentally and reconciles 3D phenotypes upon dual NRF2–p53 perturbation. TNBC-specific systems models predict differential oxidative stress capacities among cells with mutated p53, which corresponds to growth phenotypes upon genetic perturbation of the NRF2 pathway in 3D basement membrane cultures. Our results show that even in the setting of p53 mutation, different levels of residual NRF2–p53 coordination exist that predict susceptibility to NRF2 pathway perturbation. More broadly, this suggests the utility of NRF2–p53 coordination in predicting clinical response to oxidative stress-inducing cancer therapies.

5.3 Results

5.3.1 An integrated NRF2–p53 model of oxidative stress reconciles pathway coordination with 3D phenotypes

To connect NRF2 and p53 co-stabilization with spontaneous heterogeneities in oxidative stress, we assembled an integrated computational-systems model. The model expands or condenses isolated modules of NRF2 and p53 signaling from the literature, fusing them through known or reported mechanisms of crosstalk and convergence (Figure 5.1A). For the NRF2 pathway, we streamlined the detailed model of Khalil et al. (427) at several points. Instead of relying on ill-defined kinetic parameters for KEAP1-mediated ubiquitination, KEAP1:NRF2 complexes were modeled as separate oxidized or reduced species with distinct half-lives estimated by experiment (see Materials and Methods). We likewise abandoned the elaborate multistep encoding of thioredoxins, peroxiredoxins, and glutathione transferases (427) by substituting a simpler, lumped pool of antioxidant enzymes in the model. The resulting architecture is similar to the general negative-feedback control scheme of stress-response gene-regulatory networks described by Zhang & Anderson (428). Last, we retained the nucleocytoplasmic trafficking of stabilized NRF2 to account for observations that H_2O_2 stimulation retains NRF2 in the cytoplasm longer than treatment with the electrophilic stress, sulforaphane (Figure 4.16). Oxidative stress feeds directly into the NRF2 module according to a basal production rate of reactive oxygen species (ROS), which was adjusted in the final model to yield steady-state intracellular H_2O_2 concentrations consistent with the literature (429).

For the p53 pathway, we built upon the base model of Batchelor et al. (430), which was originally used to describe oscillations in p53 abundance after ionizing radiation. In this model, the kinases ATM and CHEK2 act as aggregate sensors–transducers of the DNA damage response (Figure 5.1A). They phosphorylate and stabilize p53 against degradation triggered by the ubiquitin ligase MDM2, which is also directly phosphorylated and inactivated by ATM. Stabilized p53 promotes its own degradation by inducing MDM2 transcripts and deactivates ATM–CHEK2 by enhancing transcription of the phosphatase PPM1D. For the integrated model, oxidative stress replaced DNA double-strand breaks as the pathway trigger, recognizing that ATM autoactivates in the presence of oxidants (128). Further, in response to oxidative stress, proper induction of many antioxidant enzymes requires p53 (124), which contributes to the overall antioxidant pool along with ARE target genes (Figure 5.1A). As a final candidate for NRF2–p53 crosstalk, we considered reports that the p53 target gene, p21 (CDKN1A), directly stabilizes NRF2 by interfering with KEAP1-catalyzed turnover (431,432). Together, the modifications provided an integrated model of NRF2–p53 signaling downstream of oxidative stress with enough molecular detail to enable kinetic and functional predictions.

We revisited the oxidative stress time course (Figure 4.9B) to append immunoblot quantification of ATM–CHEK2 phosphorylation and p21 abundance after H2O2 addition (Figure 5.2A). Exogenous H_2O_2 was encoded as an extracellular spike-in that decayed rapidly and spontaneously (433) amidst a basal ROS generation rate yielding a realistic intracellular H_2O_2 burden at steady state (429). The H_2O_2 partition coefficient in the model was calibrated to capture the magnitude of NRF2 stabilization (see Materials and Methods). Likewise, the parameters for H_2O_2-induced autoactivation of ATM–CHEK2 and signal inactivation were defined to align with the time-delayed kinetics and duration of p53 stabilization (Figure 5.2B). In this model, addition of p53–p21–NRF2 crosstalk (431) caused NRF2 stabilization to peak earlier and deactivate faster than observations (Figure 5.2C). We were also unable to detect even transient short-range interactions between inducible BirA*-fused versions of p21 or NRF2 and endogenous NRF2 or p21 by proximity ligation (Figure 5.3). The results thus argued against p53–p21–NRF2 crosstalk during oxidative stress in these cells.

With the provisionally calibrated base model, we sought to test whether the encoded mechanisms of regulation were sufficient to capture prior observations relating NRF2, p53, and oxidative stress. The data obtained by quantitative fluorescence microscopy (Figures 4.3B, 4.7A, and 4.9C) presumably arose from spontaneous oxidative stress that was occurring transiently and asynchronously during imaging. We mimicked oxidative-stress transients by triggering a step increase in the rate of ROS production for two hours followed by relaxation of the system for an additional 10 hours (Figure 5.1B). The magnitude of the step was sampled lognormally to elicit intracellular H_2O_2 concentrations within the range of HyPer-2 ratios observed experimentally (see Materials and Methods). We represented the asynchrony of image acquisition by randomly selecting ten snapshots of the network for each model iteration. This collection of 1000 snapshots (100 random generation rates x 10 random time points) was used to quantify coordination of species within the model.

For connecting oxidative stress to NRF2 stabilization (Fig. 4.9C), we expanded the base model to include the mRFP1-NRF2 reporter, which does not bind DNA or interact with MAF proteins and requires ~1 hr to mature fully (434) (see Materials and Methods). By contrast, HyPer-2 becomes fully oxidized within ~1 min of H_2O_2 addition (370), enabling intracellular H_2O_2 concentration in the model to be used directly as a surrogate of HyPer-2 fluorescence ratio. We calculated the mutual information from 1000 simulated snapshots and found that the two reporters were statistically coupled in the model (Figure 5.1C, MI = 0.14 [0.10–0.19]; randomized MI = 0.001 [2.8×10^{-6}–0.0005]). Associations were stronger than those observed by experiment (Figure 4.9C) due to the early time points sampled in the model (yellow-orange times in Figure 5.1C), suggesting that peak H_2O_2 transients may be difficult to observe in practice. We next compared endogenous NRF2–p53 co-stabilization between MCF10A-5E and MCF10DCIS.com cells. The base MCF10A-5E model was adjusted to reflect i) proportional differences in species abundance estimated from RNA-seq (see Materials and Methods) and ii) an increased ROS generation rate estimated from HyPer-2 imaging (Figure 4.11D). NRF2–p53 mutual information was much less dependent on signaling transients, and coupling was substantially higher in MCF10DCIS.com cells. The simulations are consistent with immunofluorescence data (Figures 4.7A, 4.9C, 5.1, D and E) and support that NRF2–p53 pathway kinetics are accurately encoded in the base model.

We asked whether the base model could also relate to the synergistic phenotypes observed upon dual NRF2–p53 perturbation in MCF10A-5E and MCF10DCIS.com cells (Figure 4.3E and 4.7E). We mimicked shNRF2 by reducing the NRF2 production rate fivefold in the model (Figure 4.3C) and encoding secondary transcriptional adaptations in other components by using the associated RNA-seq data (Figure 4.7B). For DNp53, the p53 species was rendered unable to induce transcription of MDM2, PPM1D, p21, and its share of the antioxidant enzyme pool. After re-establishing steady state, the perturbed models were challenged with the random step increase in ROS production described above. We used the time-integrated intracellular H_2O_2 concentration as the overall measure of oxidative stress experienced during simulation with either the MCF10A-5E or MCF10DCIS.com initial conditions. For both cell lines, the base model predicted synergistic increases in oxidative stress beyond the linear superposition of shNRF2 and DNp53 effects (Figure 5.1F). Encouragingly, the same conclusions were reached with models that simply encoded the reduced NRF2 production rate without secondary adaptations (Figure 5.1G). Beyond oxidative-stress inducers and antioxidant target enzymes, we conclude that the NRF2– p53 network does not require any additional mechanisms to capture signaling coordination or phenotypic interactions.

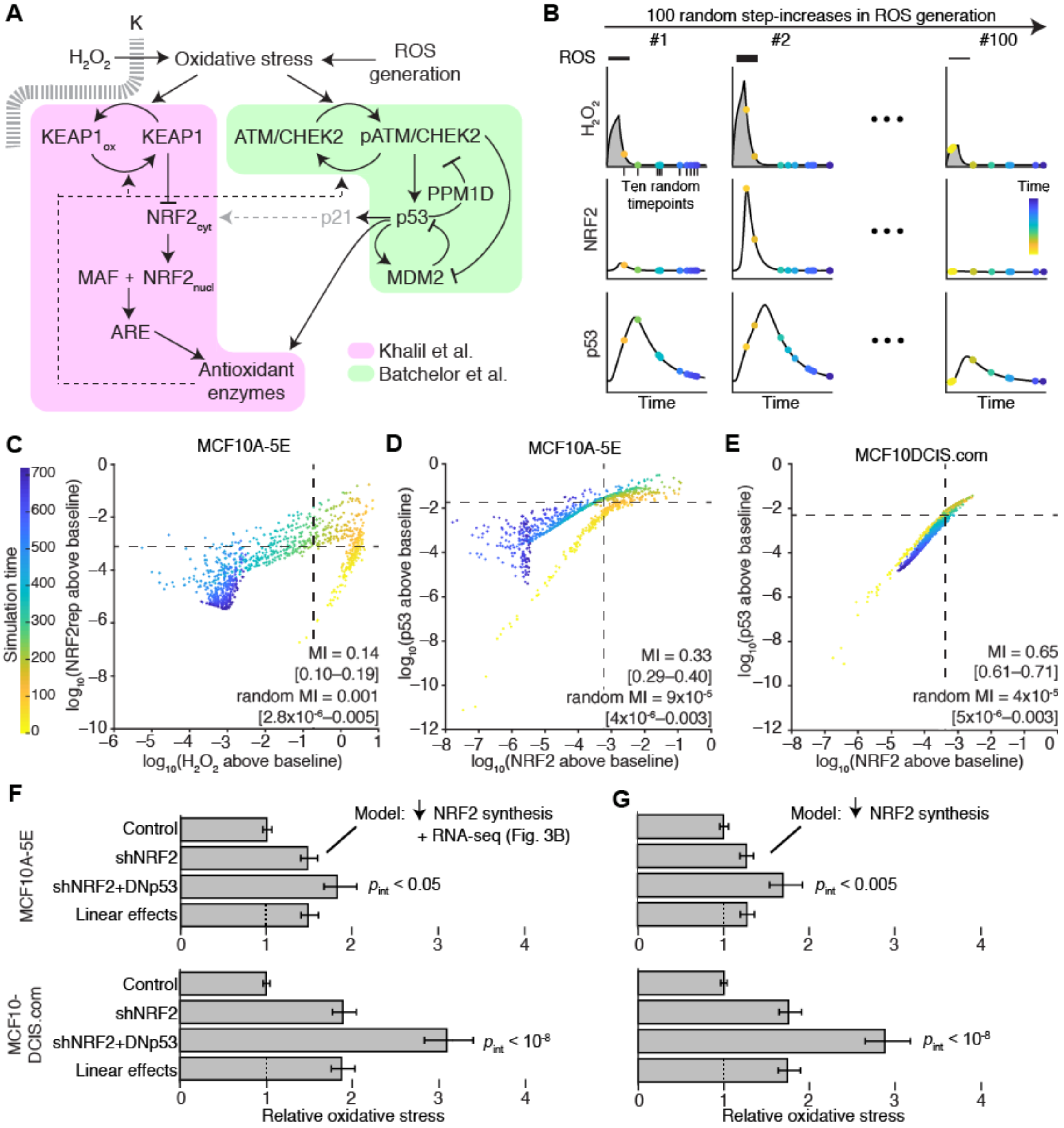
A
K
H_2O_2
Oxidative stress
ROS generation
KEAP1$_{ox}$
KEAP1
ATM/CHEK2
pATM/CHEK2
PPM1D
NRF2$_{cyt}$
p21
p53
MAF + NRF2$_{nucl}$
MDM2
ARE
Antioxidant enzymes
Khalil et al.
Batchelor et al.
B
100 random step-increases in ROS generation
#1
#2
#100
ROS
H_2O_2
NRF2
p53
Ten random timepoints
Time
Time
Time
Time
C
MCF10A-5E
Simulation time
700
600
500
400
300
200
100
0
$\log_{10}$(NRF2rep above baseline)
$\log_{10}$(H_2O_2 above baseline)
MI = 0.14
[0.10–0.19]
random MI = 0.001
[2.8x10^{-6}–0.005]
D
MCF10A-5E
$\log_{10}$(p53 above baseline)
$\log_{10}$(NRF2 above baseline)
MI = 0.33
[0.29–0.40]
random MI = 9x10^{-5}
[4x10^{-6}–0.003]
E
MCF10DCIS.com
$\log_{10}$(p53 above baseline)
$\log_{10}$(NRF2 above baseline)
MI = 0.65
[0.61–0.71]
random MI = 4x10^{-5}
[5x10^{-6}–0.003]
F
MCF10A-5E
MCF10-DCIS.com
Control
shNRF2
shNRF2+DNp53
Linear effects
Model: ↓ NRF2 synthesis + RNA-seq (Fig. 3B)
$p_{int} < 0.05$
$p_{int} < 10^{-8}$
Relative oxidative stress
G
Model: ↓ NRF2 synthesis
$p_{int} < 0.005$
$p_{int} < 10^{-8}$
Relative oxidative stress

Figure 5.1 NRF2–p53 pathway coordination and synergistic phenotypes are captured by an integrated-systems model of oxidative stress.
(A) Connecting NRF2 and p53 signaling models (427,428,430) through oxidative-stress activators and antioxidant target enzymes. Additional crosstalk linking p53 to NRF2 through p21 (435) is conditionally incorporated (gray). (B) Simulation strategy for quantifying association between signaling intermediates. The model was challenged with various ROS production rates and randomly sampled at multiple intermediate time points (yellow to blue). Integrated intracellular H2O2 (gray) is used for phenotype predictions related to NRF2 and p53 perturbation. (C) Intracellular H2O2 concentration is associated with a reporter of NRF2 stabilization (NRF2rep). (D and E) Coordination of NRF2 and p53 stabilization is high in the oxidative-stress model and increases further in simulations of premalignancy. (F and G) Modeling NRF2 knockdown by reduced synthesis captures the synergistic oxidative-stress profile of cells harboring dual perturbation of the NRF2 and p53 pathways. In (F), transcriptional changes secondary to NRF2 knockdown were added to the model according to the results in Figure 4.7B. For (C) to (E), simulated time points are shown as the log-scaled and background-subtracted mutual information (MI) with 90% CI for ten time points from n = 100 random ROS generation rates. For (F) and (G), time-integrated intracellular H2O2profiles are scaled to the unperturbed simulations and shown as the mean oxidative stress with 90% CI from n = 100 random ROS generation rates.

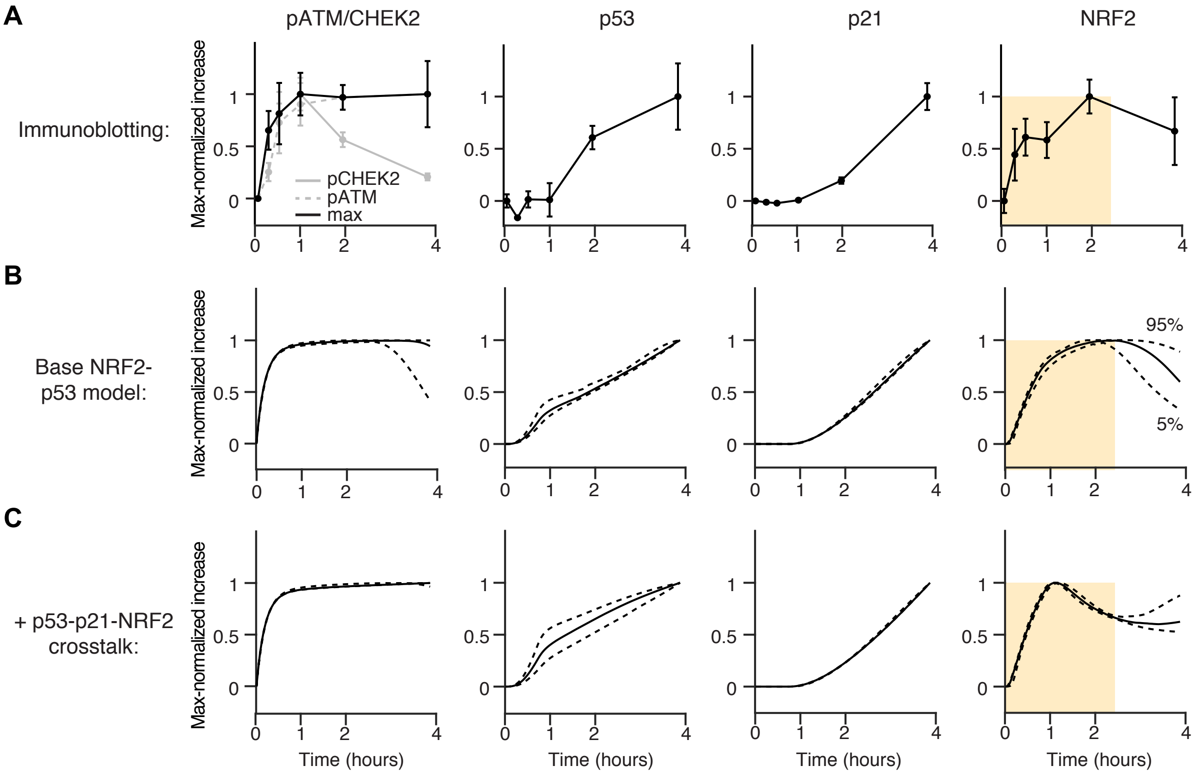

Figure 5.2 Calibration of an integrated NRF2–p53 systems model for oxidative stress. MCF10A-5E cells were treated with 200 μM H2O2 for the indicated times. (A) Quantitative immunoblotting for phospho-CHEK2 (pCHEK2 Thr68), phospho-ATM (pATM Ser1981), total p53, total p21, and total NRF2. Data are shown as the mean ± s.e.m. of n = 4 biological replicates. The maximum of pCHEK2 or pATM (max) was taken as the pATM/CHEK2 value for model calibration. (B) Calibration of the integrated base model to experimental data. (C) Addition of p53–p21–NRF2 crosstalk to the base model in (B). For (B) and (C), model results are shown as the median (solid) ± 90% confidence interval (dashed) from n = 50 simulations of initial conditions varied with a lognormal distribution of 10% about the geometric mean. Experiments and simulations are shown as the max-normalized increase above baseline, which was set to zero. The shaded region indicates the kinetic discrepancies between the two models relative to experiments.

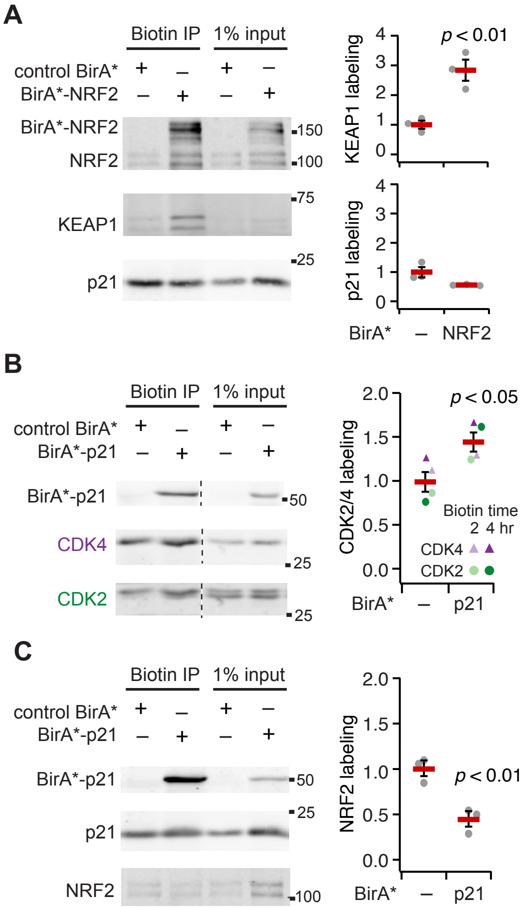

Figure 5.3 Endogenous NRF2 and p21 are not proximity labeled by BirA* fusions of each other.
(A) BirA*-NRF2 labels endogenous KEAP1 but not p21. (B and C) BirA*-p21 labels endogenous CDK4 and CDK2 (B) but not NRF2 (C). MCF10A-5E cells were treated with 1 μg/ml doxycycline for 48 hours, 10 μM sulforaphane, 10 μM Nutlin-3 and 1 mM biotin for 24 hours (A and B) or 2 and 4 hours as indicated (C). Dashed lines indicate noncontiguous lanes on the same immunoblot. Input and biotin immunoprecipitated lysates were immunoblotted for NRF2, p21, KEAP1, CDK4, and CDK2. Representative immunoblots are shown for n = 3 biological replicates for (A) and (C).

5.3.2 TNBC adaptations to p53 disruption predict variable NRF2 miscoordination, NRF2-deficient oxidative-stress profiles, and 3D growth responses

TP53 is the most-frequently mutated gene in TNBC (33), and transcriptomic analyses support it as a prevalent founder mutation in the disease (28). Disrupting p53 would undoubtedly impact transcriptional feedback and the overall cellular response to oxidative stress (Figure 5.1A). Conversely, neither *NFE2L2* nor *KEAP1* are mutated in breast cancer (28), but unclear is whether wildtype NRF2 might serve as a transient "non-oncogene" (40) that promotes stress tolerance during early tumorigenesis. Compared to in situ lesions, the stromal environment of invasive tumors is stiffer and more mesenchymal (436), which may render NRF2 signaling dispensable at later stages. We wondered whether the fragmentation of the NRF2–p53 network in TNBC cells and its origins could be reconciled with the systems model.

Using RNA-seq data from the NIH LINCS consortium (437) on 15 TNBC lines with mutated p53 (six claudin-low subtype, nine basal-like subtype), we adjusted initial conditions from the original MCF10A model and removed all transcriptional processes downstream of p53 (Figure 5.3A; see Materials and Methods). The individual TNBC models were run to steady state and then challenged with increased ROS generation rates as in Figure 5.1B. The coordination between NRF2 and mutant p53 was calculated by mutual information, and the integrated H_2O_2 response was scaled to that of MCF10A-5E cells as a relative measure of ROS tolerance. The goal was to associate the model-derived predictions with NRF2-knockdown phenotype in ROS-generating environments such as 3D culture. To the extent possible, we hoped that 3D growth in reconstituted basement membrane might quantify any vestigial requirements for NRF2 signaling from the in situ stage of the TNBC lines.

For all TNBC lines, the model predicted significantly reduced covariation between mutant p53 and NRF2 compared to MCF10DCIS.com cells with wildtype p53 (Figure 5.4B, MI < 0.25). We noted a spectrum of residual NRF2–p53 co-stabilization from weak (e.g., HCC1937, SUM159PT) to virtually nonexistent (MDA-MB-468, MDA-MB-231). Despite complete p53 deficiency in the model, this residual NRF2–p53 mutual information correlated strongly with the simulated relative increase in oxidative stress when ROS generation was increased (Figure 5.4B). Neither of these predictions mapped directly to specific transcripts in the TNBC-specific RNA-seq data (Figure 5.4A), reinforcing that the models were making nonobvious predictions about oxidative-stress handling.

To connect the model predictions with a continued role for NRF2 signaling in TNBC behavior, we selected five lines along the spectrum of mutual information and ROS tolerance. HCC1937 and SUM159PT cells were both predicted to have residual NRF2–p53 coordination and moderate ROS tolerance (Figure 5.4B). Accordingly, inducible knockdown of NRF2 in these lines did not lead to any consistent changes in 3D growth (Figure 5.4, C and D). By contrast, MDA-MB-231, HCC1806, and MDA-MB-468 cells were predicted to have among the least NRF2–p53 co-stabilization and ROS tolerance (Figure 5.4B). Knockdown of NRF2 in these lines with two different shRNAs caused significant increases or decreases in overall cell growth (Figure 5.4, E to G). Thus, model and experiment support that, despite p53 mutation, residual NRF2–p53 coupling indicates the primordial susceptibility of triple-negative malignancies to perturbations in the NRF2 pathway.

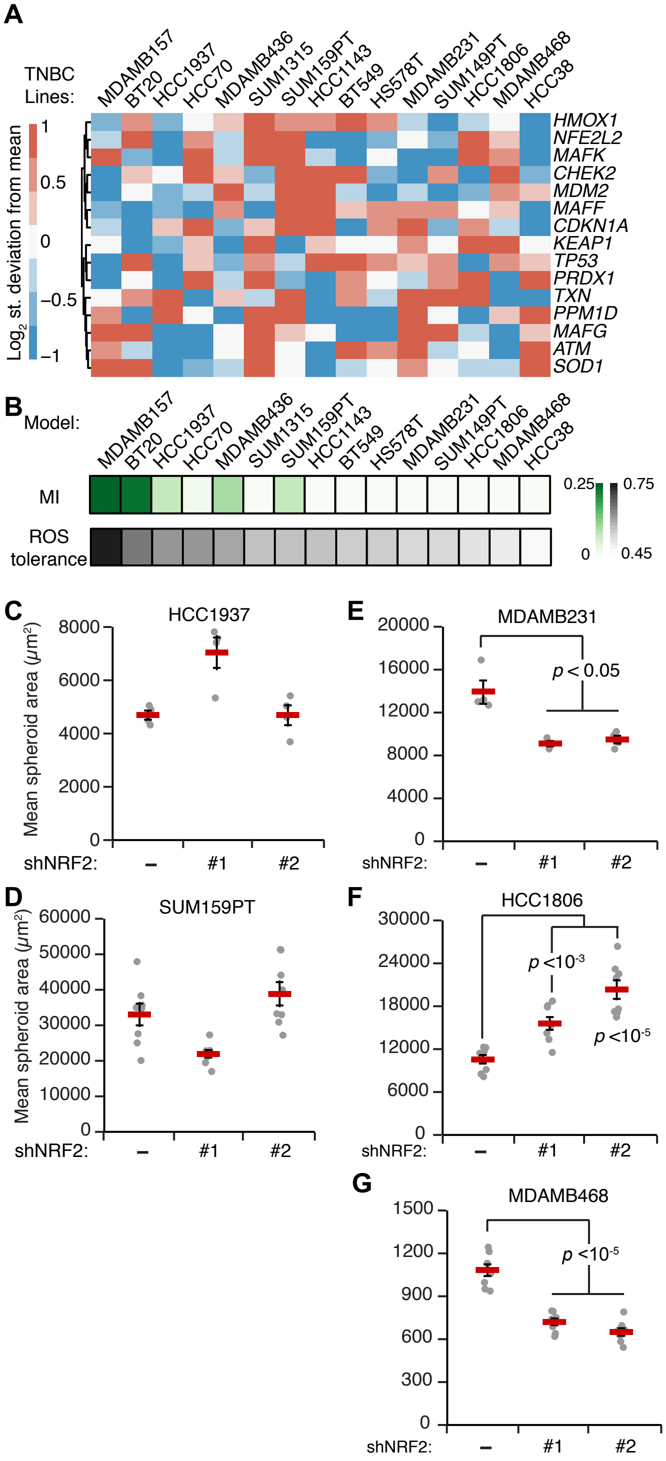
A
TNBC Lines:
MDAMB157
BT20
HCC1937
HCC70
MDAMB436
SUM1315
SUM159PT
HCC1143
BT549
HS578T
MDAMB231
SUM149PT
HCC1806
MDAMB468
HCC38
Log2 st. deviation from mean
1
0.5
0
−0.5
−1
HMOX1
NFE2L2
MAFK
CHEK2
MDM2
MAFF
CDKN1A
KEAP1
TP53
PRDX1
TXN
PPM1D
MAFG
ATM
SOD1
B
Model:
MI
ROS tolerance
0.25
0
0.75
0.45
C
HCC1937
Mean spheroid area (μm²)
8000
6000
4000
2000
0
shNRF2:
–
#1
#2
E
MDAMB231
20000
16000
12000
8000
4000
0
p < 0.05
shNRF2:
–
#1
#2
D
SUM159PT
Mean spheroid area (μm²)
60000
50000
40000
30000
20000
10000
0
shNRF2:
–
#1
#2
F
HCC1806
30000
24000
18000
12000
6000
0
p <10-3
p <10-5
shNRF2:
–
#1
#2
G
MDAMB468
1500
1200
900
600
300
0
p <10-5
shNRF2:
–
#1
#2

Figure 5.4 TNBC-specific signatures of the oxidative-stress network predict NRF2–p53 coupling and the response to NRF2 perturbations.
(A) Transcripts per million for the indicated TNBC cell lines scaled to MCF10A cells from the NIH LINCS dataset (437). The clustered transcripts were used to adjust the initial conditions of the model simulations for each cell line. (B) NRF2–p53 mutual information (MI) correlates with ROS tolerance in TNBC simulations. ROS tolerance was defined as the integrated intracellular H2O2 concentration in each cell line compared to that of MCF10A-5E cells in response to an increased ROS production rate as in Figure 5.1B. (C and D) 3D growth of TNBC cells with higher ROS tolerance and NRF2–p53 MI is unaffected by NRF2 knockdown. (E to G) TNBC cells with lower ROS tolerance and NRF2–p53 coordination show changes in 3D growth upon NRF2 knockdown. For (C) to (E), data are shown as the mean ± s.e.m. of n = 4–8 biological replicates**.**

5.4 Discussion

In this work, we use computational modeling to tackle the complexities of a dynamic oxidative stress response network in breast–mammary epithelia surrounded by basement membrane ECM. We use aspects of published computational models describing the NRF2 and p53 pathways individually to create a fused model to study pathway cooperation in response to oxidative stress at different stages of cancer progression. Despite the overall complexity of NRF2- and p53-mediated transcriptional programs (438,439) and the numerous reported mechanisms of pathway interaction (431,440–443), the coordinated response to oxidative stress is captured by a relatively simple mathematical encoding. Known core mechanisms of NRF2–p53 regulation are brought together by a shared ROS inducer and a common pool of detoxifying target genes without the need for any further crosstalk. Therefore, oxidative-stress handling in breast–mammary epithelia is usefully abstracted as two stability-regulated transcription factors working independently toward a common homeostatic goal.

Oxidative stress perturbations to the encoded NRF2–p53 network recapitulated the differing levels of signaling coordination observed experimentally in normal and premalignant breast epithelial cells. For TNBC cell lines with mutant p53, model predictions of residual NRF2–p53 coordination correlated with ROS tolerance in response to increased ROS generation. These measures coincided with TNBC growth phenotypes in reconstituted basement membrane upon NRF2 perturbation, suggesting that the model could predict which cell lines were dependent on NRF2 signaling during the in situ stage of growth.

Although NRF2 is not an oncogene for breast cancer, it has been connected with multiple breast-cancer tumor suppressors previously. In mammary epithelial cells, loss of Brca1 (a predisposing event for basal-subtype TNBC) destabilizes Nrf2 and causes an increase in ROS favoring the future acquisition of p53 mutations (108,110). In human breast cancer cells, gain-of-function p53 mutants interact directly with NRF2 and may help retain NRF2 in the nucleus (112). If certain p53 mutations were also to promote NRF2 stabilization, then it would provide a two-for-one benefit to cancer progression by relieving tumor suppression and conferring ROS tolerance constitutively. However, we did not note any association between gain-of-function p53 mutants and NRF2 abundance in TNBC lines (Figure 4.13C), suggesting that KEAP1 regulation predominates as indicated by the TNBC models. Chronic activation of the NRF2 pathway (for example, by activating *NFE2L2* mutation or *KEAP1* loss) may be disfavored if elevated intracellular ROS is not permanent. The models suggest that supraphysiological activation of NRF2 would lead to runaway induction of antioxidant enzymes, causing reductive stress as documented for NRF2 in other tissues (444). Wildtype NRF2 function must be sufficient to buffer cells from the early stresses of premalignancy and p53 disruption, allowing invasive TNBCs to deactivate the pathway when it is no longer needed. There are parallels to FOXO transcription factors (445), which are reversibly inactivated by mitogenic signals yet provide critical oxidative-stress tolerance when the breast-cancer tumor suppressor RUNX1 is disrupted (446–448).

Breast cancer cell lines organize very differently in 3D culture (449), but their response to perturbations is often less disparate. For example, gain-of-function p53 mutations cause luminal filling in MCF10A 3D cultures (353), similar to the delay in mammary-gland involution observed with mutant p53 in vivo (450). Reciprocally, knockdown of mutant p53 in MDA-MB-468 cells promotes luminal hollowing (451). Among p53-mutant TNBC lines, the impact of NRF2 knockdown on 3D growth was nonuniform but explainable through the oxidative-stress profiles inferred from TNBC-specific systems models. The balance of complexity and tractability make 3D spheroid–organoid cultures a compelling platform for systems-level dissection of cell-state heterogeneity and early tumorigenesis.

The 3D behavior of breast–mammary cancer cells is highly dependent on the surrounding ECM (452). Invasive cancers no longer encounter basement membrane ECM but must have bypassed it upon progression to carcinoma. Interestingly, although multiple TNBC lines will grow as 3D colonies in reconstituted basement membrane, others cannot, suggesting a type of cellular “amnesia” toward that past encounter. For cancers that do grow in 3D, the use of reconstituted basement membrane (as a more normal-like microenvironment) may give rise to cellular changes reminiscent of premalignancy. We exploited these changes to evaluate the relative importance of NRF2 signaling in different TNBC backgrounds. There are likely other opportunities to examine hurdles of premalignancy by using basement-membrane 3D cultures. For 3D-organoid biobanks (329), however, it is a reminder that such cultures are not propagating the primary breast tumor but rather tumor-derived cells in a more-primitive state.

Leveraging cellular redox alterations to develop effective cancer therapeutics requires the holistic understanding of redox signaling events. Our results suggest that levels of residual oxidative stress handling could identify ductal carcinoma in situ lesions that would benefit from NRF2 pathway perturbation, or more generally, oxidative stress-inducing therapeutics. The extraordinary complexity of ROS generation and its contextual effects reinforce the value of modeling redox networks at a granularity suited to a given physiology or pathology (167).

5.5 Materials and methods

Methods related to plasmids, viral transduction and selection, and mutual information calculation are exactly as in Chapter 4.5 Materials and methods.

5.5.1 Cell lines

SUM159PT cells were obtained from Asterand Biosciences and cultured in Ham's F-12 (Gibco) plus 10 mM HEPES (Gibco), 5 μg/ml insulin (Sigma), 1 μg/ml hydrocortisone (Sigma), and 5% fetal bovine serum (Hyclone). All other cell lines were obtained directly from ATCC. MDA-MB-231 and MDA-MB-468 cells were cultured in L-15 medium plus 10% fetal bovine serum without supplemental CO2. HCC1806 and HCC1937 cells were cultured in RPMI 1640 medium plus 10% fetal bovine serum. All base media were further supplemented with 1× penicillin and streptomycin (Gibco).

5.5.2 3D culture

3D overlay cultures were performed on top of Matrigel (BD Biosciences) as described previously for MCF-10A cells (404) with culture media previously optimized for each cell line (251). In addition, HCC1806 cells were cultured in MCF10A assay media (404), and SUM159PT cells were cultured in SUM159PT growth media (described above) plus 2% fetal bovine serum. For each culture, 45 μl of Matrigel was spread with a pipette tip on the bottom of an 8-well chamber slide. A suspension of 5000 single cells per well was laid on top of the Matrigel in culture media supplemented with 2% Matrigel. 3D culture medium was replaced every four days as originally described (404). For long-term knockdown experiments, cells were treated with 1 μg/ml doxycycline (Sigma) for three days before 3D culture, and doxycycline was maintained in the 3D culture medium throughout the experiment.

5.5.3 Quantitative immunoblotting

Quantitative immunoblotting was performed as previously described (25). Primary antibodies recognizing the following proteins or epitopes were used: NRF2 (Santa Cruz

Biotechnologies, #sc-13032, 1:1000), p53 (Santa Cruz Biotechnology #sc-126, 1:1000), p21 (Proteintech #10355-1-AP, 1:1000), total Chk2 (Cell Signaling #2662, 1:1000), phospho-Chk2 (Thr68, Cell Signaling #2197, 1:1000), phospho-ATM (Ser1981, Abcam #ab81292, 1:1000), KEAP1 (Santa Cruz Biotechnology #sc-15246, 1:1000), CDK4 (Cell Signaling #12790, 1:1000), CDK2 (Santa Cruz Biotechnology #sc-6248, 1:200), vinculin (Millipore #05-386, 1:10,000), GAPDH (Ambion #AM4300, 1:20,000), tubulin (Abcam #ab89984, 1:20,000), p38 (Santa Cruz Biotechnology #sc-535, 1:5000), Hsp90 (Santa Cruz Biotechnology #sc-7947, 1:5000).

5.5.4 Proximity ligation using BirA*-fusions of p21 and NRF2

MCF10A-5E cells inducibly expressing the promiscuous biotin ligase BirA* (453), BirA*-NRF2, or BirA*-CDKN1A were plated on 10-cm plates and induced with 1 µg/ml doxycycline at 50% confluency. After 24 hours, media was refed with 1 µg/ml doxycycline, 10 µM sulforaphane (Sigma), 10 µM Nutlin-3 (Calbiochem) and 1 mM biotin (Sigma). After 24 hours, cells were lysed in 200 µl RIPA buffer (50 mM Tris (pH 8.0), 150 mM NaCl, 5 mM EDTA, 1% Triton X-100, 0.1% SDS, 0.5% sodium deoxycholate). Anti-biotin antibody enrichment of biotinylated peptides was performed as previously described (454). Briefly, biotin antibody bound agarose beads (ImmuneChem Pharmaceuticals Inc., #ICP0615) were washed three times in IAP buffer (50 mM MOPS (pH 7.2), 10 mM sodium phosphate and 50 mM NaCl). 500 µg (50 µl) of antibody was added to each RIPA lysate on ice. Ice-cold IAP buffer was added up to 1 ml and samples were incubated on a nutator overnight at 4°C. The next day, beads were washed four times with ice-cold IAP buffer, boiled in dithiothreitol-containing 2× Laemmli sample buffer, and used for immunoblotting against the indicated targets.

5.5.5 Computational modeling

The NRF2 pathway was encoded as first- and second-order rate equations for KEAP1 oxidation and NRF2 stabilization; NRF2-mediated transcription of antioxidant enzymes was modeled as a Hill function (427,428). The p53 pathway was reconstructed from a delay differential equation model of p53 signaling in response to DNA damage (69). Abundances in original p53 model were unitless, but abundances were cast as concentrations in the earlier NRF2 models. Consequently, the integrated model adopted unitless abundances in its initial conditions and second-order parameters (table S2). To adapt the p53 DNA-damage model to respond to oxidative stress, we changed the ‘Signal’ activation (representing activation of upstream kinases p-ATM and p-CHEK2) from a Heaviside step function to a first-order oxidation reaction of ATM/CHEK2 by intracellular H2O2 (128). A basal ROS generation rate was added yielding a realistic intracellular H2O2 burden at steady state (429). Transcription of antioxidant enzymes by p53 (124) was modeled using the same model parameters describing the p53-mediated induction of MDM2 (430). p53- and NRF2-mediated antioxidant gene transcription contribute to a shared pool of antioxidant enzymes, which catalytically reverse the oxidation states of KEAP1 and p-ATM/CHEK2. Transcription of CDKN1A by p53 (455) was included for model calibration (Figure 5.2) and for testing the relevance of p53–p21–NRF2 crosstalk (see below). The integrated base model of NRF2–p53 oxidative-stress signaling contains 42 reactions and 22 ordinary differential equations (ODEs). The model was simulated with dde23 in MATLAB to reach steady state before the addition of oxidative stress.

The integrated model was calibrated to capture the dynamics of MCF10A-5E cells stimulated with 200 µM H2O2 (Figure 5.2). Bolus addition of H2O2 was simulated as an impulse of intracellular H2O2. We used an H2O2 partition coefficient that gave rise to NRF2 stabilization levels comparable to immunoblot quantification (extracellular / intracellular partition = 3). We approximated p-ATM/CHEK2 in the integrated model as the maximum normalized increase of p-ATM or p-CHEK2 over baseline at each experimental time point. Robustness of the system output to initial conditions was evaluated by randomly varying the concentration of model species with a log coefficient of variation of 10% taking the base model as the geometric mean.

For simulations involving the mRFP1-NRF2 reporter (NRF2rep, Figure 5.1C), NRF2rep and mature fluorescent species (Nrf2repmat) were added to the MCF10A-5E base model. Both reporter species were allowed to react with KEAP1, but neither could bind Maf proteins or antioxidant response elements in the model (Figure 4.11E). We used an mRFP1 maturation time of one hour (434) to model the conversion of NRF2rep to NRF2repmat. The modifications added 19 additional reactions and eight additional ODEs to the MCF10A-5E base model.

For simulations involving p53–p21–NRF2 crosstalk (Figure 5.2C), we added reactions involving p21 binding to NRF2 to the MCF10A-5E base model. p21 was assumed to interact with NRF2 like KEAP1 and compete with KEAP1 for binding NRF2 through its DLG and ETGE domains (431). The p21:NRF2 complex was assumed to degrade at the same reduced rate as when NRF2 is bound to oxidized KEAP1 (k_nrf2degox). These modifications added eight additional reactions and two additional ODEs to the MCF10A-5E base model.

For simulations involving MCF10DCIS.com cells (Figure 5.1, E to G), RNA-sequencing data (Figure 4.7B) was used to estimate proportional differences in model species abundance between MCF10DCIS.com and MCF10A-5E cells. Average gene expression in transcripts per million (TPM) from the four biological replicates of MCF10DCIS.com and MCF10A-5E control cell lines was calculated for each gene. Fold changes in model species of MCF10DCIS.com relative to MCF10A-5E were used to adjust each initial condition in the model. For the 'MAF' species, we used the median fold change in NRF2-binding small Mafs MAFF, MAFG, and MAFK (456). For the antioxidant species, we used the median fold-change in TXN, SOD1, PRDX1, and HMOX1 to include antioxidants that react with both free radicals and oxidized proteins (457). Additionally, the MCF10DCIS.com model included a 1.4-fold increase in the basal ROS generation rate, informed by the increased median HyPer2-ratio in MCF10DCIS.com cells compared to MCF10A-5E cells (Figure 4.11D). The increased ROS generation rate was paired with an increase basal turnover of the antioxidant pool to arrive at steady-state antioxidant gene expression levels consistent with MCF10DCIS.com RNA-seq data.

For simulations involving bursts of oxidative stress, an increased ROS production rate was added for two hours to match the duration of transient stabilizations of JUND (a gene in the

NRF2-associated gene cluster) in 3D (333). We selected the minimum increase in ROS generation that gave rise to a detectable stabilization of both the NRF2 and p53 pathways in the MCF10A-5E base model. For MCF10DCIS.com and TNBC models, the mean ROS generation rate was scaled 1.4-fold to reflect the increased basal ROS generation rate described above. NRF2 knockdown was encoded by decreasing the net synthesis rate of NRF2 fivefold to mimic the fivefold decrease in NRF2 protein resulting from short-hairpin knockdown (Figure 4.3C). To account for secondary transcriptional adaptations (Figure 5.1F), initial conditions were also adjusted by RNA-seq-based fold changes in model species for shNRF2 cells relative to negative-control cells (Figure 4.7B). Dominant negative p53 was encoded by removing all reactions downstream of p53 (transcriptional activation of MDM2, PPM1D, CDKN1A, and the p53 share of the antioxidant enzyme pool).

For the control case and all genetic perturbations (shNRF2, DNp53, and shNRF2+DNp53), 100 simulations were run with random ROS generation rates varied with a log coefficient of variation of 25% to capture the variability of HyPer-2 ratios observed experimentally (Figure 4.9D). Each simulation was run for two hours with increased ROS production rate and then an additional 10 hours to allow relaxation back to steady state. For assessment of species coordination (Figure 5.1, C to E, and 5.4B), species abundances were captured at 10 random timepoints from each simulation and mutual information was calculated as it was for quantitative immunofluorescence datasets. For oxidative stress analysis (Figure 5.1 F,G, and 5.4B), the time-integrated intracellular H2O2 concentration was used as an overall measure of oxidative stress.

For simulations involving TNBC cells (Figure 5.4, A,B), RNA-seq data from the NIH LINCS consortium (437) (HMS dataset ID: 20348) was used to estimate proportional differences in model species abundance between 15 TNBC cell lines and MCF10A cells. Reads per kilobase per million mapped reads values were normalized as transcripts per million before fold-change calculation. MAF and antioxidant species were estimated as described above. TNBC models used the same increased basal ROS generation rate as in the MCF10DCIS.com model (12). To simulate p53 mutation in the 15 p53-mutant TNBC cell lines, all reactions downstream of p53 were removed.

Chapter 6 Discussion and Future Directions

6.1 Summary of Dissertation

In this dissertation, we use systems-biology approaches to interrogate a heterogeneous stress-associated transcriptional state in breast mammary epithelial cells. In-depth knowledge of ROS (Chapter 2) and image processing techniques (Chapter 3) facilitated discovery that the transcriptional state was coordinated by the joint action of two stress-responsive transcription factors, NRF2 and p53. NRF2 and p53 are co-stabilized by spontaneous oxidative stresses in 3D culture. Perturbation of NRF2 and p53, both individually and jointly, has complex effects on target gene abundance and growth phenotypes. NRF2 disruption is compensated by p53 signaling, and disruption of both pathways results in context-dependent ROS-induced growth phenotypes.

Extending our analysis to clinical samples revealed that NRF2–p53 coordination is present in both normal breast epithelial tissue and hormone-negative ductal carcinoma in situ. However, in triple-negative breast cancers, NRF2 and now mutated p53 are largely uncoupled, suggesting invasive cancers rely on different mechanisms for oxidative stress tolerance.

To further characterize the stress response network and robustly assess NRF2–p53 co-stabilization during different stages of breast cancer, we built an integrated computational-systems model. Connecting the NRF2–p53 pathway through only a common ROS inducer and pool of antioxidant target genes recapitulated experimental measures of relative NRF2–p53 co-stabilization in normal and premalignant breast epithelial cells. The model was adapted to simulate p53 mutation in TNBC cell lines and predicted a spectrum of reduced NRF2–p53 coordination and tolerance to oxidative stress that coincided with growth phenotypes in reconstituted basement membrane.

Together, this work describes a novel linkage between the antioxidant transcription factor NRF2 and tumor suppressor p53 in detoxifying oxidative stresses. These results present an interesting paradigm in which cooperation of wild-type NRF2 and p53 provides a robust response to stress important for normal breast morphogenesis, but also creates a redundancy which could facilitate p53 loss en route to tumorigenesis. Besides the novel biological insight, this work provides a computational model which will hopefully be of use to the NRF2 and p53 cell signaling fields and a starting point for researchers seeking to holistically evaluate cellular response to oxidative stress.

6.2 Mechanistic insight on NRF2–p53 gene regulation

One of the questions that remains from this work is the exact mechanism behind gene cluster (Figure 4.1A) regulation by NRF2 and p53. Also, if this dual regulation extends to a broader network of genes important for the oxidative stress response. We began to address the first point by analyzing publically available NRF2 and p53 ChIP-SEQ datasets for binding sites within promoter regions of the cluster genes (see Materials and methods). Of the transcripts decreased upon NRF2 knockdown by short hairpin (blue in first column of Figure 6.1A), 8 contained an NRF2 binding site (Figure 6.1B). This data supports NRF2's, mainly positive, regulation over several cluster genes. Of the transcripts whose abundance increased upon NRF2 knockdown (red in first column of Figure 6.1A), 6 contained a p53 binding site, while only 2 had an NRF2 binding site. The presence of p53 binding sites in a portion of the genes upregulated upon NRF2 knockdown bolsters the claim that p53 compensates when NRF2 signaling is disrupted (Figure 4.6A,C and 4.7B). It also provides mechanistic evidence that p53 compensates through direct regulation of a number of these genes. Additionally, *CDKN1A*, one of the genes synergistically reduced upon compound NRF2–p53 perturbation, has binding sites for both NRF2 and p53, providing further evidence for its complex regulation.

Ideally, future work would involve performing NRF2 and p53 ChIP-SEQ experiments on MCF10A-5E spheroids, with identical experimental and computational workflows for each. This would allow a more accurate comparison of NRF2 and p53 binding sites throughout the genome. Also examining the intersection of NRF2 and p53 ChIP-SEQ datasets could define a broader network of genes dually regulated by NRF2 and p53 in response to spontaneous oxidative stresses in 3D cultures.

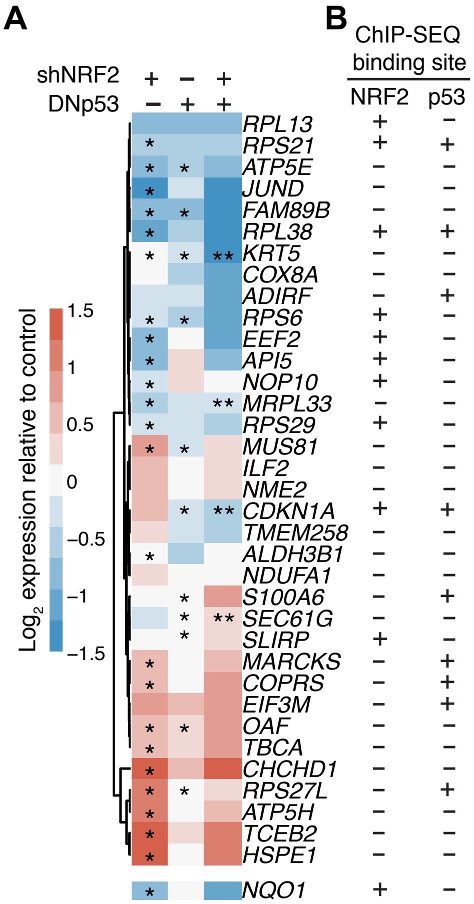

Figure 6.1 NRF2 and p53 binding sites from ChIP-SEQ analysis provide explanation for transcript level changes upon genetic perturbation of NRF2 and p53.
(A) Single and combined perturbations of NRF2 and p53 have complex effects on the gene cluster. The NRF2 target gene *NQO1* was used as a control for efficacy of shNRF2. Figure 4.2C subpanel reprinted. (B) NRF2 and p53 ChIP-SEQ binding sites annotated for cluster genes. ChIP-SEQ datasets included 3 cell lines per transcription factor. + indicates the presence of a peak in at least 1 cell line.

6.3 Applications of the NRF2–p53 network model

In Chapter 5, we built an integrated systems model of the NRF2–p53 in response to transient oxidative stresses. Incorporating RNA sequencing data as inputs, the model captured signaling coordination across multiple stages of breast tumorigenesis and made experimentally-validated predictions about oxidative-stress handling. Simulated features, including residual NRF2–p53 coupling and ROS tolerance, predicted susceptibility to perturbations in the NRF2 pathway when grown in basement membrane.

6.3.1 TNBC tumors from The Cancer Genome Atlas

To see if similar relationships between simulated features existed in the in vivo context, we used data from the Cancer Genome Atlas (https://www.cancer.gov/tcga) to predict NRF2–p53 coupling and ROS tolerance for individual TNBCs. The TNBC dataset comprises 122 tumors that were scored estrogen-receptor and progesterone-receptor negative and not HER2-enriched by a pathologist. RNA-sequencing profiles for all 122 tumors were downloaded, TPM-normalized, and used to estimate proportional differences in model species abundance between tumors and MCF10A cells. Simulations were carried out identically to how they were for TNBC cell lines (Chapter 5.5.5 Materials and methods).

Analyzing and displaying the model transcript levels in TNBC cell lines and tumors side-by-side revealed differences between the two contexts. Levels of certain species were consistently lower and more variable among tumors compared to cell lines (*CHEK2, ATM, MAFK, MDM2*). Decreased abundance of *CHEK2*, *ATM*, and *MDM2* suggest p53 pathway deficiency in tumors compared to cell lines. Since all cell lines and tumors alike had mutated p53, the difference is likely influenced by the in vivo context. Desmoplastic stroma, characteristic of most breast carcinomas, is stiffer than normal stroma and exerts tension on breast cancer cells (458,459). Matrix stiffening and tensile forces alter gene expression, including the activity of many adhesion and growth-factor dependent transcriptional networks

(460–462). In fact, matrix stiffening causes increased phosphorylation of focal adhesion kinase (FAK) (459), which inhibits p53 through enhanced ubiquitination and degradation (463–465). Thus, characteristics of the tumor microenvironment could explain some of the tumor-specific transcriptional differences observed (Figure 6.2A).

In TNBC cell lines, residual NRF2–p53 mutual information correlated with the simulated increase in oxidative stress compared to MCF10A cells when ROS generation was increased. Among TNBC tumors, however, the relationship is more complex (Figure 6.2B). NRF2–p53 mutual information no longer correlated with ability to tolerate increased ROS generation. Tumors also displayed a wider range of NRF2–p53 mutual information. The majority were within the range seen among cell lines (MI < 0.25), but there were several tumors having much greater simulated MI than cell lines (colored dark green in heatmap). These differences, including the larger range of NRF2–p53 MI observed, could be attributed to the heterogeneous tumor microenvironment and its influences on signaling pathways. Complexities in TNBC results aren't surprising, however, as model predictions of overall lower NRF2–p53 MI compared to normal breast epithelia and premalignancies suggested that full-blown TNBC evokes a different set of dependencies for stress tolerance.

The relatively simple NRF2–p53 computational model appears useful in the in vitro setting, where it correctly predicted levels of NRF2–p53 coordination and stress tolerance. However, interpreting predictions from patient data is more difficult, as these cannot be experimentally tested as they could for cell lines. It remains to be determined if the computational model can capture the complexities of an in vivo environment.

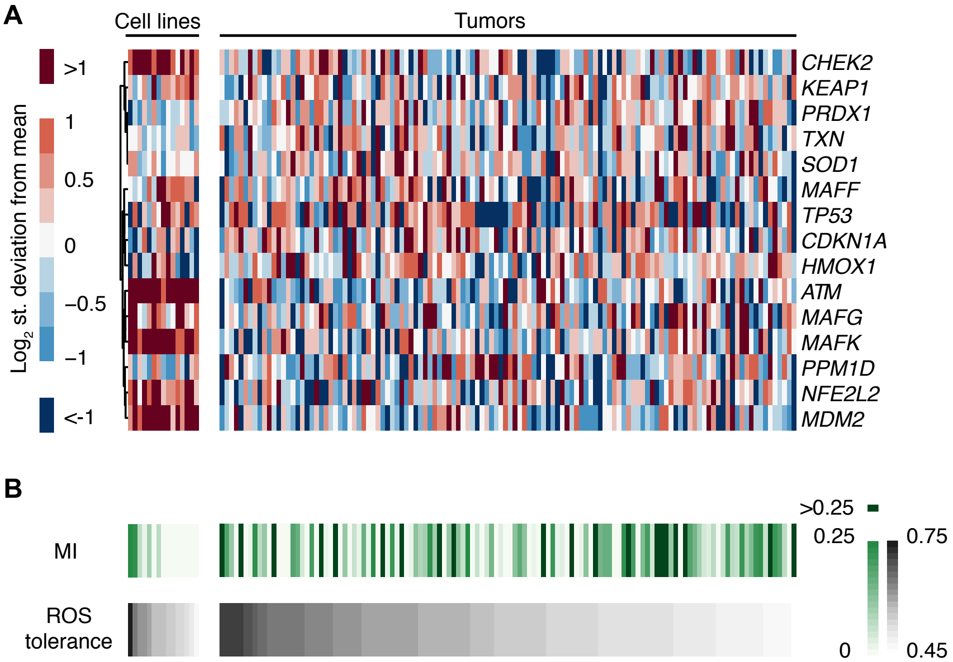

Figure 6.2 Tumor-specific differences in model transcript abundance and NRF2–p53 MI-ROS tolerance mapping.
(A) Transcripts per million for TNBC cell lines (in Figure 5.4A) and tumors from The Cancer Genome Atlas database scaled to MCF10A cells. (B) A complex relationship exists between NRF2–p53 mutual information (MI) and ROS tolerance in TNBC tumor simulations. ROS tolerance was defined as the integrated intracellular H2O2 concentration in each cell line compared to that of MCF10A-5E cells in response to an increased ROS production rate as in Figure 5.1B.

6.3.2 Gain-of-function p53 mutations

An important area which we did not delve into in this dissertation is the role of gain-of-function p53 mutants in NRF2 pathway regulation and response to oxidative stress. While the prevalence of GOF p53 mutations in TNBC is difficult to ascertain due to oncogenic properties of p53 mutants continually being discovered, a recent manual annotation of TCGA tumors we performed found that ~22% of TNBC tumors harbored mutants with published oncogenic properties. This represents a substantial portion of tumors in which mutant p53 has more than just a dominant-negative effect, as discussed earlier (Chapter 1.6.2).

There have been multiple reports of gain-of-function p53 mutants regulating NRF2 target genes (162,165). Both studies found evidence that GOF p53 mutants repressed NRF2-regulated genes in response to oxidative stress. Walerych et al. showed that five p53 missense mutants co-immunoprecipitated with NRF2 (162), indicating direct interaction of the two molecules. The computational NRF2–p53 systems model presented in Chapter 5 provides a platform to test hypotheses about NRF2-GOF p53 regulation. For example, to simulate the findings published by Walerych et al, reactions involving p53 binding NRF2 would be added to the TNBC model (used in Figure 5.4). As the exact location of GOF p53 binding to NRF2 is unknown, for simplicity we could model p53 binding and inhibiting NRF2 activity as its negative regulator KEAP1 does. Less antioxidant production by NRF2 due to GOF p53 binding should further decrease oxidative stress tolerance and have an unpredictable effect on NRF2–p53 MI. However, since GOF p53 is known to regulate multiple pathways besides NRF2 that could impinge upon the oxidative stress response, the current architecture might not be able to accurately capture all relevant signaling dynamics. For example, GOF p53 is known to activate the NF-κB pathway (466,467), which is responsible for inducing ROS scavenging enzymes such as SOD2 (236). An expanded model including additional ROS-mediating signaling pathways might be necessary to most accurately capture GOF p53 effects on oxidative-stress handling.

6.3.3 Hormone-positive breast cancers

The NRF2–p53 oxidative stress handling network may be relevant for other subtypes of breast cancer. While the network was discovered in a basal-like breast epithelial cell line, NRF2–p53 coordination was observed in normal breast epithelial tissue (Figure 4.14D), thus not necessarily limiting its relevance to the basal-like subtype. It would be interesting to evaluate NRF2–p53 coordination in hormone-positive premalignancies and breast cancers. As opposed to basal-like breast cancer, of which 80% are *TP53* mutated, hormone-positive subtypes comprise less *TP53* mutated tumors (33). NRF2–p53 coordination by mutual information was significantly diminished in TNBC tissue regardless of whether p53 was hyperstabilized (presumably mutated) or not (Figure 4.14D). However, computational modeling predicted a spectrum of residual co-stabilization observed among TNBC cell lines (Figure 5.4B) and tumors (Figure 6.1B). It would be hard to thoroughly evaluate the effect of *TP53* mutation on NRF2–p53 coordination within TNBC tumors because the vast majority are mutated (in fact, all tumors analyzed in Figure 6.1 for which somatic mutation data was available had *TP53* mutations).

Luminal A or luminal B tumors, of which only 12% and 29% harbor *TP53* mutations respectively (33), are a useful testbed to robustly evaluate the effect of *TP53* mutation on NRF2–p53 coordination within the same tumor subtype. I would expect that NRF2 and p53 would remain coupled in hormone-positive premalignancies to detoxify increased levels of oxidative stress, as they were in hormone-negative lesions. Luminal breast cancers might exhibit a wider range of NRF2–p53 coordination as compared to TNBCs, as tumors with wild-type p53 might rely more heavily on the intact NRF2–p53 oxidative stress response. In addition, estrogen generates ROS through its metabolism by cytochrome P450 enzymes, which gives rise to reactive semiquinones and quinones (468–471). ER+ breast cancers exhibit higher levels of 8-hydroxydeoxyguanosine, a marker of oxidative DNA damage, compared to TNBC cells, indicating a higher oxidative burden (472,473). Increased ROS levels could potentially make the NRF2–p53 oxidative stress response more important for ER+ breast cancer cell survival.

Collectively, experimental and computational analysis of NRF2–p53 coordination in luminal tumors would help to determine if the NRF2–p53 stress response is 1) a conserved mechanism used by breast premalignant cells regardless of hormone receptor status and 2) relevant in breast cancer cells with wild-type p53 that have invaded into the stroma.

6.4 Concluding remarks

This dissertation demonstrates the power of a systems biology approach to discover biological meaning from large datasets. Starting from a group of heterogeneously expressed transcripts found by microarray profiling, analytical methods identified NRF2 as a candidate regulator of a stress-associated gene cluster. These results guided experiments to validate candidate regulators, assess potential coregulation with another stress-activated transcription factor, and evaluate upstream coordinators of the regulatory state. Immunofluorescence was heavily used to assess pathway coactivation in multiple settings, and image processing techniques were crucial to produce quantitative metrics from fluorescence images. Experimental evidence that NRF2 and p53 were coordinately activated by oxidative stress led us to build an integrated systems model to robustly test hypotheses of network architecture and NRF2–p53 coordination during different stages of breast cancer. Finally, the model made nonobvious predictions about oxidative stress tolerance in TNBC cell lines, which we tested using 3D spheroid–organoid cultures. The synergistic blend of experimental and computational approaches allowed us to address a hypothesis from multiple angles and, ultimately, to integrate individual cellular mechanisms into a stress-handling network model that is both explanatory and predictive.

6.5 Materials and methods

NRF2 ChIP-SEQ raw data files were downloaded from ENCODE (Accession #ENCAB800OND), consisting of fastq files from 3 cell lines (K562, A549, HepG2) with 2 biological replicates each. Quality of the sequenced reads was analyzed using FastQC. Reads were aligned to the human genome (hg19) using BWA with the -M option. Peaks were identified using MACS2 (version 2.1.0) with a FDR cutoff of 0.01 to reduce the number of spurious peaks. Irreproducibility discovery rate analysis was performed on biological replicates and a cutoff of 0.05 was used to generate a list of high confidence peaks for each cell line. Peaks were annotated using the Homer annotatePeaks program.

p53 ChIP-SEQ binding sites were used from a recently published ChIP-SEQ dataset (474). Briefly, ChIP-SEQ was performed on 3 cell lines (HCT116, MCF7, SJSA) treated with or without the MDM2 inhibitor Nutlin. Reads were mapped to hg19 using Bowtie2 and peaks were identified and annotated using the Homer suite.

Binding site is indicated (Figure 6.1B) if a peak was present for a gene in at least 1 of 3 cell lines analyzed for each ChIP-SEQ dataset.

References

1. Bae YS, Kang SW, Seo MS, Baines IC, Tekle E, Chock PB, et al. Epidermal growth factor (EGF)-induced generation of hydrogen peroxide. Role in EGF receptor-mediated tyrosine phosphorylation. J Biol Chem. 1997 Jan 3;272(1):217–21.
2. Sundaresan M, Yu ZX, Ferrans VJ, Irani K, Finkel T. Requirement for generation of H2O2 for platelet-derived growth factor signal transduction. Science. 1995 Oct 13;270(5234):296–9.
3. Schmid E, El Benna J, Galter D, Klein G, Dröge W. Redox priming of the insulin receptor beta-chain associated with altered tyrosine kinase activity and insulin responsiveness in the absence of tyrosine autophosphorylation. FASEB J. 1998 Jul;12(10):863–70.
4. Abe J, Kusuhara M, Ulevitch RJ, Berk BC, Lee JD. Big mitogen-activated protein kinase 1 (BMK1) is a redox-sensitive kinase. J Biol Chem. 1996 Jul 12;271(28):16586–90.
5. Beckman KB, Ames BN. The free radical theory of aging matures. Physiol Rev. 1998 Apr;78(2):547–81.
6. Dreher D, Junod AF. Role of oxygen free radicals in cancer development. Eur J Cancer. 1996 Jan;32A(1):30–8.
7. Hussain SP, Aguilar F, Amstad P, Cerutti P. Oxy-radical induced mutagenesis of hotspot codons 248 and 249 of the human p53 gene. Oncogene. 1994 Aug;9(8):2277–81.
8. Ogrunc M, Di Micco R, Liontos M, Bombardelli L, Mione M, Fumagalli M, et al. Oncogene-induced reactive oxygen species fuel hyperproliferation and DNA damage response activation. Cell Death & Differentiation. 2014 Jun;21(6):998–1012.
9. Mason JA, Davison-Versagli CA, Leliaert AK, Pape DJ, McCallister C, Zuo J, et al. Oncogenic Ras differentially regulates metabolism and anoikis in extracellular matrix-detached cells. Cell Death Differ. 2016;23(8):1271–82.
10. Davison CA, Durbin SM, Thau MR, Zellmer VR, Chapman SE, Diener J, et al. Antioxidant enzymes mediate survival of breast cancer cells deprived of extracellular matrix. Cancer Res. 2013 Jun 15;73(12):3704–15.
11. Schafer ZT, Grassian AR, Song L, Jiang Z, Gerhart-Hines Z, Irie HY, et al. Antioxidant and oncogene rescue of metabolic defects caused by loss of matrix attachment. Nature. 2009 Sep 3;461(7260):109–13.
12. Szatrowski TP, Nathan CF. Production of large amounts of hydrogen peroxide by human tumor cells. Cancer Res. 1991 Feb 1;51(3):794–8.
13. Toyokuni S, Okamoto K, Yodoi J, Hiai H. Persistent oxidative stress in cancer. FEBS Lett. 1995 Jan 16;358(1):1–3.
14. Diehn M, Cho RW, Lobo NA, Kalisky T, Dorie MJ, Kulp AN, et al. Association of reactive oxygen species levels and radioresistance in cancer stem cells. Nature. 2009 Apr 9;458(7239):780–3.
15. Behrend L, Henderson G, Zwacka RM. Reactive oxygen species in oncogenic transformation. Biochem Soc Trans. 2003 Dec;31(Pt 6):1441–4.
16. Wu W-S. The signaling mechanism of ROS in tumor progression. Cancer Metastasis Rev. 2006 Dec;25(4):695–705.
17. Perou CM, Sørlie T, Eisen MB, van de Rijn M, Jeffrey SS, Rees CA, et al. Molecular portraits of human breast tumours. Nature. 2000 Aug;406(6797):747–52.
18. Sørlie T, Perou CM, Tibshirani R, Aas T, Geisler S, Johnsen H, et al. Gene expression patterns of breast carcinomas distinguish tumor subclasses with clinical implications. Proc Natl Acad Sci USA. 2001 Sep 11;98(19):10869–74.
19. Parker JS, Mullins M, Cheang MC, Leung S, Voduc D, Vickery T, et al. Supervised risk predictor of breast cancer based on intrinsic subtypes. J Clin Oncol. 2009 Mar 10;27(8):1160–7.

20. Louie MC, Sevigny MB. Steroid hormone receptors as prognostic markers in breast cancer. Am J Cancer Res. 2017 Aug 1;7(8):1617–36.
21. Fisher B, Redmond C, Fisher ER, Caplan R. Relative worth of estrogen or progesterone receptor and pathologic characteristics of differentiation as indicators of prognosis in node negative breast cancer patients: findings from National Surgical Adjuvant Breast and Bowel Project Protocol B-06. J Clin Oncol. 1988 Jul;6(7):1076–87.
22. Parl FF, Schmidt BP, Dupont WD, Wagner RK. Prognostic significance of estrogen receptor status in breast cancer in relation to tumor stage, axillary node metastasis, and histopathologic grading. Cancer. 1984 Nov 15;54(10):2237–42.
23. Crowe JP, Gordon NH, Hubay CA, Shenk RR, Zollinger RM, Brumberg DJ, et al. Estrogen receptor determination and long term survival of patients with carcinoma of the breast. Surg Gynecol Obstet. 1991 Oct;173(4):273–8.
24. Oh D-Y, Bang Y-J. HER2-targeted therapies — a role beyond breast cancer. Nature Reviews Clinical Oncology. 2020 Jan;17(1):33–48.
25. Nielsen TO, Hsu FD, Jensen K, Cheang M, Karaca G, Hu Z, et al. Immunohistochemical and clinical characterization of the basal-like subtype of invasive breast carcinoma. Clin Cancer Res. 2004 Aug 15;10(16):5367–74.
26. van de Rijn M, Perou CM, Tibshirani R, Haas P, Kallioniemi O, Kononen J, et al. Expression of Cytokeratins 17 and 5 Identifies a Group of Breast Carcinomas with Poor Clinical Outcome. Am J Pathol. 2002 Dec;161(6):1991–6.
27. Dent R, Trudeau M, Pritchard KI, Hanna WM, Kahn HK, Sawka CA, et al. Triple-negative breast cancer: clinical features and patterns of recurrence. Clin Cancer Res. 2007 Aug 1;13(15 Pt 1):4429–34.
28. Shah SP, Roth A, Goya R, Oloumi A, Ha G, Zhao Y, et al. The clonal and mutational evolution spectrum of primary triple-negative breast cancers. Nature. 2012 Apr 4;486(7403):395–9.
29. Banerjee S, Reis-Filho JS, Ashley S, Steele D, Ashworth A, Lakhani SR, et al. Basal-like breast carcinomas: clinical outcome and response to chemotherapy. J Clin Pathol. 2006 Jul;59(7):729–35.
30. Higgins MJ, Baselga J. Targeted therapies for breast cancer. J Clin Invest. 2011 Oct;121(10):3797–803.
31. Laakso M, Tanner M, Nilsson J, Wiklund T, Erikstein B, Kellokumpu-Lehtinen P, et al. Basoluminal carcinoma: a new biologically and prognostically distinct entity between basal and luminal breast cancer. Clin Cancer Res. 2006 Jul 15;12(14 Pt 1):4185–91.
32. Bryan BB, Schnitt SJ, Collins LC. Ductal carcinoma in situ with basal-like phenotype: a possible precursor to invasive basal-like breast cancer. Mod Pathol. 2006 May;19(5):617–21.
33. Cancer Genome Atlas N. Comprehensive molecular portraits of human breast tumours. Nature. 2012 Oct 4;490(7418):61–70.
34. Foulkes WD, Stefansson IM, Chappuis PO, Bégin LR, Goffin JR, Wong N, et al. Germline BRCA1 mutations and a basal epithelial phenotype in breast cancer. J Natl Cancer Inst. 2003 Oct 1;95(19):1482–5.
35. Stefansson OA, Jonasson JG, Olafsdottir K, Hilmarsdottir H, Olafsdottir G, Esteller M, et al. CpG island hypermethylation of BRCA1 and loss of pRb as co-occurring events in basal/triple-negative breast cancer. Epigenetics. 2011 May;6(5):638–49.
36. Lakhani SR, Reis-Filho JS, Fulford L, Penault-Llorca F, van der Vijver M, Parry S, et al. Prediction of BRCA1 status in patients with breast cancer using estrogen receptor and basal phenotype. Clin Cancer Res. 2005 Jul 15;11(14):5175–80.
37. Fridman JS, Lowe SW. Control of apoptosis by p53. Oncogene. 2003 Dec;22(56):9030–40.

38. Crook T, Brooks LA, Crossland S, Osin P, Barker KT, Waller J, et al. p53 mutation with frequent novel condons but not a mutator phenotype in BRCA1- and BRCA2-associated breast tumours. Oncogene. 1998 Oct 1;17(13):1681–9.
39. Peng L, Xu T, Long T, Zuo H. Association Between BRCA Status and P53 Status in Breast Cancer: A Meta-Analysis. Med Sci Monit. 2016 Jun 8;22:1939–45.
40. Luo J, Solimini NL, Elledge SJ. Principles of Cancer Therapy: Oncogene and Non-oncogene Addiction. Cell. 2009 Mar 6;136(5):823–37.
41. Collin F. Chemical Basis of Reactive Oxygen Species Reactivity and Involvement in Neurodegenerative Diseases. Int J Mol Sci [Internet]. 2019 May 15 [cited 2020 Jan 23];20(10). Available from: https://www.ncbi.nlm.nih.gov/pmc/articles/PMC6566277/
42. Muller FL, Liu Y, Van Remmen H. Complex III releases superoxide to both sides of the inner mitochondrial membrane. J Biol Chem. 2004 Nov 19;279(47):49064–73.
43. Rhee SG, Bae YS, Lee SR, Kwon J. Hydrogen peroxide: a key messenger that modulates protein phosphorylation through cysteine oxidation. Sci STKE. 2000 Oct 10;2000(53):pe1.
44. Itoh K, Chiba T, Takahashi S, Ishii T, Igarashi K, Katoh Y, et al. An Nrf2/small Maf heterodimer mediates the induction of phase II detoxifying enzyme genes through antioxidant response elements. Biochem Biophys Res Commun. 1997 Jul 18;236(2):313–22.
45. Chorley BN, Campbell MR, Wang X, Karaca M, Sambandan D, Bangura F, et al. Identification of novel NRF2-regulated genes by ChIP-Seq: influence on retinoid X receptor alpha. Nucleic Acids Res. 2012 Aug;40(15):7416–29.
46. Wardman P. Reduction Potentials of One-Electron Couples Involving Free Radicals in Aqueous Solution. Journal of Physical and Chemical Reference Data. 1989 Oct 1;18(4):1637–755.
47. Jackson AL, Loeb LA. The contribution of endogenous sources of DNA damage to the multiple mutations in cancer. Mutat Res. 2001 Jun 2;477(1–2):7–21.
48. Cadet J, Wagner JR. DNA Base Damage by Reactive Oxygen Species, Oxidizing Agents, and UV Radiation. Cold Spring Harb Perspect Biol [Internet]. 2013 Feb [cited 2020 Jan 15];5(2). Available from: https://www.ncbi.nlm.nih.gov/pmc/articles/PMC3552502/
49. Breen AP, Murphy JA. Reactions of oxyl radicals with DNA. Free Radic Biol Med. 1995 Jun;18(6):1033–77.
50. Bhattacharyya A, Chattopadhyay R, Mitra S, Crowe SE. Oxidative Stress: An Essential Factor in the Pathogenesis of Gastrointestinal Mucosal Diseases. Physiol Rev. 2014 Apr;94(2):329–54.
51. Diakowska D, Lewandowski A, Kopeć W, Diakowski W, Chrzanowska T. Oxidative DNA damage and total antioxidant status in serum of patients with esophageal squamous cell carcinoma. Hepatogastroenterology. 2007 Sep;54(78):1701–4.
52. Neeley WL, Essigmann JM. Mechanisms of formation, genotoxicity, and mutation of guanine oxidation products. Chem Res Toxicol. 2006 Apr;19(4):491–505.
53. Weinberg RA, Weinberg RA. The Biology of Cancer. Garland Science; 2013. 962 p.
54. Zienolddiny S, Ryberg D, Haugen A. Induction of microsatellite mutations by oxidative agents in human lung cancer cell lines. Carcinogenesis. 2000 Aug;21(8):1521–6.
55. Nelson DR, Kamataki T, Waxman DJ, Guengerich FP, Estabrook RW, Feyereisen R, et al. The P450 superfamily: update on new sequences, gene mapping, accession numbers, early trivial names of enzymes, and nomenclature. DNA Cell Biol. 1993 Feb;12(1):1–51.
56. Xu C, Li CY-T, Kong A-NT. Induction of phase I, II and III drug metabolism/transport by xenobiotics. Arch Pharm Res. 2005 Mar;28(3):249–68.
57. Ma Q. Role of Nrf2 in Oxidative Stress and Toxicity. Annu Rev Pharmacol Toxicol. 2013;53:401–26.

58. Raghunath A, Sundarraj K, Nagarajan R, Arfuso F, Bian J, Kumar AP, et al. Antioxidant response elements: Discovery, classes, regulation and potential applications. Redox Biology. 2018 Jul 1;17:297–314.
59. Sandelin A, Alkema W, Engström P, Wasserman WW, Lenhard B. JASPAR: an open-access database for eukaryotic transcription factor binding profiles. Nucleic Acids Res. 2004 Jan 1;32(Database issue):D91-94.
60. Rushmore TH, Morton MR, Pickett CB. The antioxidant responsive element. Activation by oxidative stress and identification of the DNA consensus sequence required for functional activity. J Biol Chem. 1991 Jun 25;266(18):11632–9.
61. Cullinan SB, Gordan JD, Jin J, Harper JW, Diehl JA. The Keap1-BTB Protein Is an Adaptor That Bridges Nrf2 to a Cul3-Based E3 Ligase: Oxidative Stress Sensing by a Cul3-Keap1 Ligase. Molecular and Cellular Biology. 2004 Oct 1;24(19):8477–86.
62. Kobayashi A, Kang M-I, Okawa H, Ohtsuji M, Zenke Y, Chiba T, et al. Oxidative Stress Sensor Keap1 Functions as an Adaptor for Cul3-Based E3 Ligase To Regulate Proteasomal Degradation of Nrf2. Molecular and Cellular Biology. 2004 Aug 15;24(16):7130–9.
63. Zhang DD, Lo S-C, Cross JV, Templeton DJ, Hannink M. Keap1 Is a Redox-Regulated Substrate Adaptor Protein for a Cul3-Dependent Ubiquitin Ligase Complex. Molecular and Cellular Biology. 2004 Dec 15;24(24):10941–53.
64. Tong KI, Katoh Y, Kusunoki H, Itoh K, Tanaka T, Yamamoto M. Keap1 Recruits Neh2 through Binding to ETGE and DLG Motifs: Characterization of the Two-Site Molecular Recognition Model. Mol Cell Biol. 2006 Apr;26(8):2887–900.
65. Kobayashi M, Itoh K, Suzuki T, Osanai H, Nishikawa K, Katoh Y, et al. Identification of the interactive interface and phylogenic conservation of the Nrf2-Keap1 system. Genes Cells. 2002 Aug;7(8):807–20.
66. Katoh Y, Iida K, Kang M-I, Kobayashi A, Mizukami M, Tong KI, et al. Evolutionary conserved N-terminal domain of Nrf2 is essential for the Keap1-mediated degradation of the protein by proteasome. Arch Biochem Biophys. 2005 Jan 15;433(2):342–50.
67. Itoh K, Wakabayashi N, Katoh Y, Ishii T, O'Connor T, Yamamoto M. Keap1 regulates both cytoplasmic-nuclear shuttling and degradation of Nrf2 in response to electrophiles. Genes Cells. 2003 Apr;8(4):379–91.
68. Dinkova-Kostova AT, Holtzclaw WD, Cole RN, Itoh K, Wakabayashi N, Katoh Y, et al. Direct evidence that sulfhydryl groups of Keap1 are the sensors regulating induction of phase 2 enzymes that protect against carcinogens and oxidants. Proc Natl Acad Sci U S A. 2002 Sep 3;99(18):11908–13.
69. Satoh T, Kosaka K, Itoh K, Kobayashi A, Yamamoto M, Shimojo Y, et al. Carnosic acid, a catechol-type electrophilic compound, protects neurons both in vitro and in vivo through activation of the Keap1/Nrf2 pathway via S-alkylation of targeted cysteines on Keap1. J Neurochem. 2008 Feb;104(4):1116–31.
70. Saito R, Suzuki T, Hiramoto K, Asami S, Naganuma E, Suda H, et al. Characterizations of Three Major Cysteine Sensors of Keap1 in Stress Response. Mol Cell Biol. 2016 15;36(2):271–84.
71. Suzuki T, Muramatsu A, Saito R, Iso T, Shibata T, Kuwata K, et al. Molecular Mechanism of Cellular Oxidative Stress Sensing by Keap1. Cell Rep. 2019 Jul 16;28(3):746-758 e4.
72. Hu C, Eggler AL, Mesecar AD, van Breemen RB. Modification of keap1 cysteine residues by sulforaphane. Chem Res Toxicol. 2011 Apr 18;24(4):515–21.
73. Hong F, Freeman ML, Liebler DC. Identification of sensor cysteines in human Keap1 modified by the cancer chemopreventive agent sulforaphane. Chem Res Toxicol. 2005 Dec;18(12):1917–26.

74. Zhang DD, Hannink M. Distinct cysteine residues in Keap1 are required for Keap1-dependent ubiquitination of Nrf2 and for stabilization of Nrf2 by chemopreventive agents and oxidative stress. Mol Cell Biol. 2003 Nov;23(22):8137–51.
75. Itoh K, Igarashi K, Hayashi N, Nishizawa M, Yamamoto M. Cloning and characterization of a novel erythroid cell-derived CNC family transcription factor heterodimerizing with the small Maf family proteins. Mol Cell Biol. 1995 Aug;15(8):4184–93.
76. Thimmulappa RK, Mai KH, Srisuma S, Kensler TW, Yamamoto M, Biswal S. Identification of Nrf2-regulated Genes Induced by the Chemopreventive Agent Sulforaphane by Oligonucleotide Microarray. Cancer Res. 2002 Sep 15;62(18):5196–203.
77. Nguyen T, Huang HC, Pickett CB. Transcriptional Regulation of the Antioxidant Response Element ACTIVATION BY Nrf2 AND REPRESSION BY MafK. J Biol Chem. 2000 May 19;275(20):15466–73.
78. Abu-Bakar A, Lämsä V, Arpiainen S, Moore MR, Lang MA, Hakkola J. Regulation of CYP2A5 Gene by the Transcription Factor Nuclear Factor (Erythroid-Derived 2)-Like 2. Drug Metab Dispos. 2007 May 1;35(5):787–94.
79. Marchitti SA, Brocker C, Orlicky DJ, Vasiliou V. Molecular Characterization, Expression Analysis and Role of ALDH3B1 in The Cellular Protection Against Oxidative Stress. Free Radic Biol Med. 2010 Nov 15;49(9):1432–43.
80. Favreau LV, Pickett CB. Transcriptional regulation of the rat NAD(P)H:quinone reductase gene. Identification of regulatory elements controlling basal level expression and inducible expression by planar aromatic compounds and phenolic antioxidants. J Biol Chem. 1991 Mar 5;266(7):4556–61.
81. Mitsuishi Y, Taguchi K, Kawatani Y, Shibata T, Nukiwa T, Aburatani H, et al. Nrf2 redirects glucose and glutamine into anabolic pathways in metabolic reprogramming. Cancer Cell. 2012 Jul 10;22(1):66–79.
82. Moinova HR, Mulcahy RT. An electrophile responsive element (EpRE) regulates beta-naphthoflavone induction of the human gamma-glutamylcysteine synthetase regulatory subunit gene. Constitutive expression is mediated by an adjacent AP-1 site. J Biol Chem. 1998 Jun 12;273(24):14683–9.
83. Mulcahy RT, Wartman MA, Bailey HH, Gipp JJ. Constitutive and beta-naphthoflavone-induced expression of the human gamma-glutamylcysteine synthetase heavy subunit gene is regulated by a distal antioxidant response element/TRE sequence. J Biol Chem. 1997 Mar 14;272(11):7445–54.
84. Rangasamy T, Cho CY, Thimmulappa RK, Zhen L, Srisuma SS, Kensler TW, et al. Genetic ablation of Nrf2 enhances susceptibility to cigarette smoke-induced emphysema in mice. J Clin Invest. 2004 Nov;114(9):1248–59.
85. Harvey CJ, Thimmulappa RK, Singh A, Blake DJ, Ling G, Wakabayashi N, et al. Nrf2-regulated glutathione recycling independent of biosynthesis is critical for cell survival during oxidative stress. Free Radic Biol Med. 2009 Feb 15;46(4):443–53.
86. Sasaki H, Sato H, Kuriyama-Matsumura K, Sato K, Maebara K, Wang H, et al. Electrophile response element-mediated induction of the cystine/glutamate exchange transporter gene expression. J Biol Chem. 2002 Nov 22;277(47):44765–71.
87. Hawkes H-JK, Karlenius TC, Tonissen KF. Regulation of the human thioredoxin gene promoter and its key substrates: a study of functional and putative regulatory elements. Biochim Biophys Acta. 2014 Jan;1840(1):303–14.
88. Kim Y-J, Ahn J-Y, Liang P, Ip C, Zhang Y, Park Y-M. Human prx1 gene is a target of Nrf2 and is up-regulated by hypoxia/reoxygenation: implication to tumor biology. Cancer Res. 2007 Jan 15;67(2):546–54.
89. Alam J, Stewart D, Touchard C, Boinapally S, Choi AM, Cook JL. Nrf2, a Cap'n'Collar transcription factor, regulates induction of the heme oxygenase-1 gene. J Biol Chem. 1999 Sep 10;274(37):26071–8.

90. Aggarwal BB, Bhardwaj A, Aggarwal RS, Seeram NP, Shishodia S, Takada Y. Role of resveratrol in prevention and therapy of cancer: preclinical and clinical studies. Anticancer Res. 2004 Oct;24(5A):2783–840.
91. Liou G-Y, Storz P. Reactive oxygen species in cancer. Free Radic Res [Internet]. 2010 May [cited 2020 Jan 20];44(5). Available from: https://www.ncbi.nlm.nih.gov/pmc/articles/PMC3880197/
92. Ichijo H, Nishida E, Irie K, ten Dijke P, Saitoh M, Moriguchi T, et al. Induction of apoptosis by ASK1, a mammalian MAPKKK that activates SAPK/JNK and p38 signaling pathways. Science. 1997 Jan 3;275(5296):90–4.
93. Moon D-O, Kim M-O, Choi YH, Hyun JW, Chang WY, Kim G-Y. Butein induces G(2)/M phase arrest and apoptosis in human hepatoma cancer cells through ROS generation. Cancer Lett. 2010 Feb 28;288(2):204–13.
94. Trachootham D, Zhou Y, Zhang H, Demizu Y, Chen Z, Pelicano H, et al. Selective killing of oncogenically transformed cells through a ROS-mediated mechanism by beta-phenylethyl isothiocyanate. Cancer Cell. 2006 Sep;10(3):241–52.
95. Shaw AT, Winslow MM, Magendantz M, Ouyang C, Dowdle J, Subramanian A, et al. Selective killing of K-ras mutant cancer cells by small molecule inducers of oxidative stress. Proc Natl Acad Sci USA. 2011 May 24;108(21):8773–8.
96. Ren D, Villeneuve NF, Jiang T, Wu T, Lau A, Toppin HA, et al. Brusatol enhances the efficacy of chemotherapy by inhibiting the Nrf2-mediated defense mechanism. Proc Natl Acad Sci USA. 2011 Jan 25;108(4):1433–8.
97. Hayes JD, McMahon M. NRF2 and KEAP1 mutations: permanent activation of an adaptive response in cancer. Trends Biochem Sci. 2009 Apr;34(4):176–88.
98. Weinstein JN, Collisson EA, Mills GB, Shaw KM, Ozenberger BA, Ellrott K, et al. The Cancer Genome Atlas Pan-Cancer Analysis Project. Nat Genet. 2013 Oct;45(10):1113–20.
99. Shibata T, Ohta T, Tong KI, Kokubu A, Odogawa R, Tsuta K, et al. Cancer related mutations in NRF2 impair its recognition by Keap1-Cul3 E3 ligase and promote malignancy. PNAS. 2008 Sep 9;105(36):13568–73.
100. Tao S, Wang S, Moghaddam SJ, Ooi A, Chapman E, Wong PK, et al. Oncogenic KRAS confers chemoresistance by upregulating NRF2. Cancer Res. 2014 Dec 15;74(24):7430–41.
101. Tew KD. Glutathione-associated enzymes in anticancer drug resistance. Cancer Res. 1994 Aug 15;54(16):4313–20.
102. Young LC, Campling BG, Cole SP, Deeley RG, Gerlach JH. Multidrug resistance proteins MRP3, MRP1, and MRP2 in lung cancer: correlation of protein levels with drug response and messenger RNA levels. Clin Cancer Res. 2001 Jun;7(6):1798–804.
103. Soini Y, Näpänkangas U, Järvinen K, Kaarteenaho-Wiik R, Pääkkö P, Kinnula VL. Expression of gamma-glutamyl cysteine synthetase in nonsmall cell lung carcinoma. Cancer. 2001 Dec 1;92(11):2911–9.
104. Ohta T, Iijima K, Miyamoto M, Nakahara I, Tanaka H, Ohtsuji M, et al. Loss of Keap1 function activates Nrf2 and provides advantages for lung cancer cell growth. Cancer Res. 2008 Mar 1;68(5):1303–9.
105. Satoh H, Moriguchi T, Takai J, Ebina M, Yamamoto M. Nrf2 prevents initiation but accelerates progression through the Kras signaling pathway during lung carcinogenesis. Cancer Res. 2013 Jul 1;73(13):4158–68.
106. Aoki Y, Hashimoto AH, Amanuma K, Matsumoto M, Hiyoshi K, Takano H, et al. Enhanced spontaneous and benzo(a)pyrene-induced mutations in the lung of Nrf2-deficient gpt delta mice. Cancer Res. 2007 Jun 15;67(12):5643–8.

107. Singh B, Chatterjee A, Ronghe AM, Bhat NK, Bhat HK. Antioxidant-mediated up-regulation of OGG1 via NRF2 induction is associated with inhibition of oxidative DNA damage in estrogen-induced breast cancer. BMC Cancer. 2013 May 22;13:253.
108. Gorrini C, Gang BP, Bassi C, Wakeham A, Baniasadi SP, Hao Z, et al. Estrogen controls the survival of BRCA1-deficient cells via a PI3K-NRF2-regulated pathway. Proc Natl Acad Sci U S A. 2014 Mar 25;111(12):4472–7.
109. Narod SA, Foulkes WD. BRCA1 and BRCA2: 1994 and beyond. Nat Rev Cancer. 2004 Sep;4(9):665–76.
110. Gorrini C, Baniasadi PS, Harris IS, Silvester J, Inoue S, Snow B, et al. BRCA1 interacts with Nrf2 to regulate antioxidant signaling and cell survival. J Exp Med. 2013 Jul 29;210(8):1529–44.
111. Wen WX, Leong C-O. Association of BRCA1- and BRCA2-deficiency with mutation burden, expression of PD-L1/PD-1, immune infiltrates, and T cell-inflamed signature in breast cancer. PLoS One [Internet]. 2019 Apr 25 [cited 2020 Jan 20];14(4). Available from: https://www.ncbi.nlm.nih.gov/pmc/articles/PMC6483182/
112. Walerych D, Lisek K, Sommaggio R, Piazza S, Ciani Y, Dalla E, et al. Proteasome machinery is instrumental in a common gain-of-function program of the p53 missense mutants in cancer. Nat Cell Biol. 2016 Aug;18(8):897–909.
113. Horn HF, Vousden KH. Coping with stress: multiple ways to activate p53. Oncogene. 2007 Feb 26;26(9):1306–16.
114. Joerger AC, Fersht AR. The Tumor Suppressor p53: From Structures to Drug Discovery. Cold Spring Harb Perspect Biol [Internet]. 2010 Jun [cited 2020 Jan 21];2(6). Available from: https://www.ncbi.nlm.nih.gov/pmc/articles/PMC2869527/
115. Balagurumoorthy P, Sakamoto H, Lewis MS, Zambrano N, Clore GM, Gronenborn AM, et al. Four p53 DNA-binding domain peptides bind natural p53-response elements and bend the DNA. Proc Natl Acad Sci U S A. 1995 Sep 12;92(19):8591–5.
116. Wang Y, Schwedes JF, Parks D, Mann K, Tegtmeyer P. Interaction of p53 with its consensus DNA-binding site. Mol Cell Biol. 1995 Apr;15(4):2157–65.
117. el-Deiry WS, Kern SE, Pietenpol JA, Kinzler KW, Vogelstein B. Definition of a consensus binding site for p53. Nat Genet. 1992 Apr;1(1):45–9.
118. Kannan K, Kaminski N, Rechavi G, Jakob-Hirsch J, Amariglio N, Givol D. DNA microarray analysis of genes involved in p53 mediated apoptosis: activation of Apaf-1. Oncogene. 2001 Jun 7;20(26):3449–55.
119. Madden SL, Galella EA, Zhu J, Bertelsen AH, Beaudry GA. SAGE transcript profiles for p53-dependent growth regulation. Oncogene. 1997 Aug 28;15(9):1079–85.
120. Mirza A, Wu Q, Wang L, McClanahan T, Bishop WR, Gheyas F, et al. Global transcriptional program of p53 target genes during the process of apoptosis and cell cycle progression. Oncogene. 2003 Jun 5;22(23):3645–54.
121. Chen X, Chen J, Gan S, Guan H, Zhou Y, Ouyang Q, et al. DNA damage strength modulates a bimodal switch of p53 dynamics for cell-fate control. BMC Biol. 2013 Jun 21;11:73.
122. Purvis JE, Karhohs KW, Mock C, Batchelor E, Loewer A, Lahav G. p53 dynamics control cell fate. Science. 2012 Jun 15;336(6087):1440–4.
123. Lahav G, Rosenfeld N, Sigal A, Geva-Zatorsky N, Levine AJ, Elowitz MB, et al. Dynamics of the p53-Mdm2 feedback loop in individual cells. Nat Genet. 2004 Feb;36(2):147–50.
124. Sablina AA, Budanov AV, Ilyinskaya GV, Agapova LS, Kravchenko JE, Chumakov PM. The antioxidant function of the p53 tumor suppressor. Nat Med. 2005 Dec;11(12):1306–13.
125. Kubbutat MH, Jones SN, Vousden KH. Regulation of p53 stability by Mdm2. Nature. 1997 May 15;387(6630):299–303.

126. Bakkenist CJ, Kastan MB. DNA damage activates ATM through intermolecular autophosphorylation and dimer dissociation. Nature. 2003 Jan 30;421(6922):499–506.
127. Hirao A, Kong YY, Matsuoka S, Wakeham A, Ruland J, Yoshida H, et al. DNA damage-induced activation of p53 by the checkpoint kinase Chk2. Science. 2000 Mar 10;287(5459):1824–7.
128. Guo Z, Kozlov S, Lavin MF, Person MD, Paull TT. ATM Activation by Oxidative Stress. Science. 2010 Oct 22;330(6003):517–21.
129. Lu X, Nannenga B, Donehower LA. PPM1D dephosphorylates Chk1 and p53 and abrogates cell cycle checkpoints. Genes Dev. 2005 May 15;19(10):1162–74.
130. Tan T, Chu G. p53 Binds and Activates the Xeroderma Pigmentosum DDB2 Gene in Humans but Not Mice. Mol Cell Biol. 2002 May;22(10):3247–54.
131. Adimoolam S, Ford JM. p53 and DNA damage-inducible expression of the xeroderma pigmentosum group C gene. Proc Natl Acad Sci USA. 2002 Oct 1;99(20):12985–90.
132. Xu J, Morris GF. p53-Mediated Regulation of Proliferating Cell Nuclear Antigen Expression in Cells Exposed to Ionizing Radiation. Mol Cell Biol. 1999 Jan;19(1):12–20.
133. Velasco-Miguel S, Buckbinder L, Jean P, Gelbert L, Talbott R, Laidlaw J, et al. PA26, a novel target of the p53 tumor suppressor and member of the GADD family of DNA damage and growth arrest inducible genes. Oncogene. 1999 Jan 7;18(1):127–37.
134. Tan M, Li S, Swaroop M, Guan K, Oberley LW, Sun Y. Transcriptional activation of the human glutathione peroxidase promoter by p53. J Biol Chem. 1999 Apr 23;274(17):12061–6.
135. Hussain SP, Amstad P, He P, Robles A, Lupold S, Kaneko I, et al. p53-induced up-regulation of MnSOD and GPx but not catalase increases oxidative stress and apoptosis. Cancer Res. 2004 Apr 1;64(7):2350–6.
136. el-Deiry WS, Tokino T, Velculescu VE, Levy DB, Parsons R, Trent JM, et al. WAF1, a potential mediator of p53 tumor suppression. Cell. 1993 Nov 19;75(4):817–25.
137. Kastan MB, Zhan Q, el-Deiry WS, Carrier F, Jacks T, Walsh WV, et al. A mammalian cell cycle checkpoint pathway utilizing p53 and GADD45 is defective in ataxia-telangiectasia. Cell. 1992 Nov 13;71(4):587–97.
138. Okamoto K, Beach D. Cyclin G is a transcriptional target of the p53 tumor suppressor protein. EMBO J. 1994 Oct 17;13(20):4816–22.
139. Miyashita T, Reed JC. Tumor suppressor p53 is a direct transcriptional activator of the human bax gene. Cell. 1995 Jan 27;80(2):293–9.
140. Sax JK, Fei P, Murphy ME, Bernhard E, Korsmeyer SJ, El-Deiry WS. BID regulation by p53 contributes to chemosensitivity. Nat Cell Biol. 2002 Nov;4(11):842–9.
141. Oda E, Ohki R, Murasawa H, Nemoto J, Shibue T, Yamashita T, et al. Noxa, a BH3-only member of the Bcl-2 family and candidate mediator of p53-induced apoptosis. Science. 2000 May 12;288(5468):1053–8.
142. Nakano K, Vousden KH. PUMA, a novel proapoptotic gene, is induced by p53. Mol Cell. 2001 Mar;7(3):683–94.
143. Müller M, Wilder S, Bannasch D, Israeli D, Lehlbach K, Li-Weber M, et al. p53 Activates the CD95 (APO-1/Fas) Gene in Response to DNA Damage by Anticancer Drugs. J Exp Med. 1998 Dec 7;188(11):2033–45.
144. MacLachlan TK, El-Deiry WS. Apoptotic threshold is lowered by p53 transactivation of caspase-6. Proc Natl Acad Sci USA. 2002 Jul 9;99(14):9492–7.
145. Bensaad K, Tsuruta A, Selak MA, Vidal MNC, Nakano K, Bartrons R, et al. TIGAR, a p53-inducible regulator of glycolysis and apoptosis. Cell. 2006 Jul 14;126(1):107–20.
146. Koch JG, Gu X, Han Y, El-Naggar AK, Olson MV, Medina D, et al. Mammary tumor modifiers in BALB/cJ mice heterozygous for p53. Mamm Genome. 2007 May;18(5):300–9.

147. Wu X, Bayle JH, Olson D, Levine AJ. The p53-mdm-2 autoregulatory feedback loop. Genes Dev. 1993 Jul;7(7A):1126–32.
148. Juven T, Barak Y, Zauberman A, George DL, Oren M. Wild type p53 can mediate sequence-specific transactivation of an internal promoter within the mdm2 gene. Oncogene. 1993 Dec;8(12):3411–6.
149. Fiscella M, Zhang H, Fan S, Sakaguchi K, Shen S, Mercer WE, et al. Wip1, a novel human protein phosphatase that is induced in response to ionizing radiation in a p53-dependent manner. Proc Natl Acad Sci USA. 1997 Jun 10;94(12):6048–53.
150. Hollstein M, Sidransky D, Vogelstein B, Harris CC. p53 mutations in human cancers. Science. 1991 Jul 5;253(5015):49–53.
151. Vogelstein B, Lane D, Levine AJ. Surfing the p53 network. Nature. 2000 Nov 16;408(6810):307–10.
152. Robles AI, Linke SP, Harris CC. The p53 network in lung carcinogenesis. Oncogene. 2002 Oct 7;21(45):6898–907.
153. Hollstein M, Rice K, Greenblatt MS, Soussi T, Fuchs R, Sørlie T, et al. Database of p53 gene somatic mutations in human tumors and cell lines. Nucleic Acids Res. 1994 Sep;22(17):3551–5.
154. Milner J, Medcalf EA. Cotranslation of activated mutant p53 with wild type drives the wild-type p53 protein into the mutant conformation. Cell. 1991 May 31;65(5):765–74.
155. Milner J, Medcalf EA, Cook AC. Tumor suppressor p53: analysis of wild-type and mutant p53 complexes. Mol Cell Biol. 1991 Jan;11(1):12–9.
156. Chin KV, Ueda K, Pastan I, Gottesman MM. Modulation of activity of the promoter of the human MDR1 gene by Ras and p53. Science. 1992 Jan 24;255(5043):459–62.
157. Frazier MW, He X, Wang J, Gu Z, Cleveland JL, Zambetti GP. Activation of c-myc Gene Expression by Tumor-Derived p53 Mutants Requires a Discrete C-Terminal Domain. Mol Cell Biol. 1998 Jul;18(7):3735–43.
158. Ludes-Meyers JH, Subler MA, Shivakumar CV, Munoz RM, Jiang P, Bigger JE, et al. Transcriptional activation of the human epidermal growth factor receptor promoter by human p53. Mol Cell Biol. 1996 Nov;16(11):6009–19.
159. Lee YI, Lee S, Das GC, Park US, Park SM, Lee YI. Activation of the insulin-like growth factor II transcription by aflatoxin B1 induced p53 mutant 249 is caused by activation of transcription complexes; implications for a gain-of-function during the formation of hepatocellular carcinoma. Oncogene. 2000 Aug 3;19(33):3717–26.
160. Brosh R, Rotter V. When mutants gain new powers: news from the mutant p53 field. Nat Rev Cancer. 2009 Oct;9(10):701–13.
161. Walerych D, Napoli M, Collavin L, Del Sal G. The rebel angel: mutant p53 as the driving oncogene in breast cancer. Carcinogenesis. 2012 Nov;33(11):2007–17.
162. Walerych D, Lisek K, Sommaggio R, Piazza S, Ciani Y, Dalla E, et al. Proteasome machinery is instrumental in a common gain-of-function program of the p53 missense mutants in cancer. Nat Cell Biol. 2016 Aug;18(8):897–909.
163. Weisz L, Damalas A, Liontos M, Karakaidos P, Fontemaggi G, Maor-Aloni R, et al. Mutant p53 enhances nuclear factor kappaB activation by tumor necrosis factor alpha in cancer cells. Cancer Res. 2007 15;67(6):2396–401.
164. Di Agostino S, Strano S, Emiliozzi V, Zerbini V, Mottolese M, Sacchi A, et al. Gain of function of mutant p53: the mutant p53/NF-Y protein complex reveals an aberrant transcriptional mechanism of cell cycle regulation. Cancer Cell. 2006 Sep;10(3):191–202.
165. Kalo E, Kogan-Sakin I, Solomon H, Bar-Nathan E, Shay M, Shetzer Y, et al. Mutant p53R273H attenuates the expression of phase 2 detoxifying enzymes and promotes the survival of cells with high levels of reactive oxygen species. J Cell Sci. 2012 Nov 15;125(Pt 22):5578–86.

166. Pereira EJ, Burns JS, Lee CY, Marohl T, Calderon D, Wang L, et al. Sporadic activation of an oxidative stress-dependent NRF2–p53 signaling network in breast epithelial spheroids and premalignancies. bioRxiv. 2019 Dec 5;862474.
167. Pereira EJ, Smolko CM, Janes KA. Computational Models of Reactive Oxygen Species as Metabolic Byproducts and Signal-Transduction Modulators. Front Pharmacol [Internet]. 2016 [cited 2016 Nov 29];7. Available from: http://journal.frontiersin.org/article/10.3389/fphar.2016.00457/abstract
168. Smith MA, Richey Harris PL, Sayre LM, Beckman JS, Perry G. Widespread peroxynitrite-mediated damage in Alzheimer's disease. J Neurosci. 1997 Apr 15;17(8):2653–7.
169. Giasson BI, Duda JE, Murray IVJ, Chen Q, Souza JM, Hurtig HI, et al. Oxidative Damage Linked to Neurodegeneration by Selective α-Synuclein Nitration in Synucleinopathy Lesions. Science. 2000 Nov 3;290(5493):985–9.
170. Patetsios P, Song M, Shutze WP, Pappas C, Rodino W, Ramirez JA, et al. Identification of uric acid and xanthine oxidase in atherosclerotic plaque. Am J Cardiol. 2001 Jul 15;88(2):188–91, A6.
171. Guzik TJ, Sadowski J, Guzik B, Jopek A, Kapelak B, Przybylowski P, et al. Coronary artery superoxide production and nox isoform expression in human coronary artery disease. Arterioscler Thromb Vasc Biol. 2006 Feb;26(2):333–9.
172. Nishikawa T, Edelstein D, Du XL, Yamagishi S, Matsumura T, Kaneda Y, et al. Normalizing mitochondrial superoxide production blocks three pathways of hyperglycaemic damage. Nature. 2000 Apr 13;404(6779):787–90.
173. Dounousi E, Papavasiliou E, Makedou A, Ioannou K, Katopodis KP, Tselepis A, et al. Oxidative stress is progressively enhanced with advancing stages of CKD. Am J Kidney Dis. 2006 Nov;48(5):752–60.
174. Meng T-C, Fukada T, Tonks NK. Reversible oxidation and inactivation of protein tyrosine phosphatases in vivo. Mol Cell. 2002 Feb;9(2):387–99.
175. Leslie NR, Bennett D, Lindsay YE, Stewart H, Gray A, Downes CP. Redox regulation of PI 3-kinase signalling via inactivation of PTEN. EMBO J. 2003 Oct 15;22(20):5501–10.
176. Ruiz-Ginés JA, López-Ongil S, González-Rubio M, González-Santiago L, Rodríguez-Puyol M, Rodríguez-Puyol D. Reactive oxygen species induce proliferation of bovine aortic endothelial cells. J Cardiovasc Pharmacol. 2000 Jan;35(1):109–13.
177. Nieto N, Friedman SL, Cederbaum AI. Stimulation and proliferation of primary rat hepatic stellate cells by cytochrome P450 2E1–derived reactive oxygen species. Hepatology. 2002 Jan 1;35(1):62–73.
178. Qu Y, Wang J, Ray PS, Guo H, Huang J, Shin-Sim M, et al. Thioredoxin-like 2 regulates human cancer cell growth and metastasis via redox homeostasis and NF-κB signaling. J Clin Invest. 2011 Jan;121(1):212–25.
179. Pierce GB, Parchment RE, Lewellyn AL. Hydrogen peroxide as a mediator of programmed cell death in the blastocyst. Differentiation. 1991 Apr;46(3):181–6.
180. Janes KA, Lauffenburger DA. Models of signalling networks - what cell biologists can gain from them and give to them. J Cell Sci. 2013 May 1;126(Pt 9):1913–21.
181. Rota C, Fann YC, Mason RP. Phenoxyl free radical formation during the oxidation of the fluorescent dye 2',7'-dichlorofluorescein by horseradish peroxidase. Possible consequences for oxidative stress measurements. J Biol Chem. 1999 Oct 1;274(40):28161–8.
182. Hanson GT, Aggeler R, Oglesbee D, Cannon M, Capaldi RA, Tsien RY, et al. Investigating mitochondrial redox potential with redox-sensitive green fluorescent protein indicators. J Biol Chem. 2004 Mar 26;279(13):13044–53.
183. Belousov VV, Fradkov AF, Lukyanov KA, Staroverov DB, Shakhbazov KS, Terskikh AV, et al. Genetically encoded fluorescent indicator for intracellular hydrogen peroxide. Nat Methods. 2006 Apr;3(4):281–6.

184. Meyer AJ, Dick TP. Fluorescent protein-based redox probes. Antioxid Redox Signal. 2010 Sep 1;13(5):621–50.
185. Malinouski M, Zhou Y, Belousov VV, Hatfield DL, Gladyshev VN. Hydrogen peroxide probes directed to different cellular compartments. PLoS ONE. 2011 Jan 21;6(1):e14564.
186. Swain L, Kesemeyer A, Meyer-Roxlau S, Vettel C, Zieseniss A, Güntsch A, et al. Redox Imaging Using Cardiac Myocyte-Specific Transgenic Biosensor Mice. Circ Res. 2016 Oct 14;119(9):1004–16.
187. Ezeriņa D, Morgan B, Dick TP. Imaging dynamic redox processes with genetically encoded probes. J Mol Cell Cardiol. 2014 Aug;73:43–9.
188. Brito PM, Antunes F. Estimation of kinetic parameters related to biochemical interactions between hydrogen peroxide and signal transduction proteins. Front Chem [Internet]. 2014 Oct 2 [cited 2016 Oct 31];2. Available from: http://www.ncbi.nlm.nih.gov/pmc/articles/PMC4183122/
189. Lim JB, Huang BK, Deen WM, Sikes HD. Analysis of the lifetime and spatial localization of hydrogen peroxide generated in the cytosol using a reduced kinetic model. Free Radic Biol Med. 2015 Dec;89:47–53.
190. Lim JB, Langford TF, Huang BK, Deen WM, Sikes HD. A reaction-diffusion model of cytosolic hydrogen peroxide. Free Radic Biol Med. 2016 Jan;90:85–90.
191. Sobotta MC, Barata AG, Schmidt U, Mueller S, Millonig G, Dick TP. Exposing cells to H2O2: a quantitative comparison between continuous low-dose and one-time high-dose treatments. Free Radic Biol Med. 2013 Jul;60:325–35.
192. Cheong T-C, Shin EP, Kwon E-K, Choi J-H, Wang K-K, Sharma P, et al. Functional manipulation of dendritic cells by photoswitchable generation of intracellular reactive oxygen species. ACS Chem Biol. 2015 Mar 20;10(3):757–65.
193. Chandel NS, McClintock DS, Feliciano CE, Wood TM, Melendez JA, Rodriguez AM, et al. Reactive oxygen species generated at mitochondrial complex III stabilize hypoxia-inducible factor-1alpha during hypoxia: a mechanism of O2 sensing. J Biol Chem. 2000 Aug 18;275(33):25130–8.
194. Selivanov VA, Votyakova TV, Zeak JA, Trucco M, Roca J, Cascante M. Bistability of mitochondrial respiration underlies paradoxical reactive oxygen species generation induced by anoxia. PLoS Comput Biol. 2009 Dec;5(12):e1000619.
195. Gauthier LD, Greenstein JL, Cortassa S, O'Rourke B, Winslow RL. A computational model of reactive oxygen species and redox balance in cardiac mitochondria. Biophys J. 2013 Aug 20;105(4):1045–56.
196. Padmaraj D, Pande R, Miller JH, Wosik J, Zagozdzon-Wosik W. Mitochondrial Membrane Studies Using Impedance Spectroscopy with Parallel pH Monitoring. PLoS One [Internet]. 2014 Jul 10 [cited 2016 Sep 6];9(7). Available from: http://www.ncbi.nlm.nih.gov/pmc/articles/PMC4091947/
197. Korshunov SS, Skulachev VP, Starkov AA. High protonic potential actuates a mechanism of production of reactive oxygen species in mitochondria. FEBS Letters. 1997 Oct 13;416(1):15–8.
198. Selivanov VA, Zeak JA, Roca J, Cascante M, Trucco M, Votyakova TV. The role of external and matrix pH in mitochondrial reactive oxygen species generation. J Biol Chem. 2008 Oct 24;283(43):29292–300.
199. Aon MA, Cortassa S, O'Rourke B. Redox-optimized ROS balance: a unifying hypothesis. Biochim Biophys Acta. 2010;1797(6–7):865–77.
200. Gauthier LD, Greenstein JL, O'Rourke B, Winslow RL. An Integrated Mitochondrial ROS Production and Scavenging Model: Implications for Heart Failure. Biophys J. 2013 Dec 17;105(12):2832–42.

201. Kembro JM, Aon MA, Winslow RL, O'Rourke B, Cortassa S. Integrating mitochondrial energetics, redox and ROS metabolic networks: a two-compartment model. Biophys J. 2013 Jan 22;104(2):332–43.
202. Satapati S, Kucejova B, Duarte JAG, Fletcher JA, Reynolds L, Sunny NE, et al. Mitochondrial metabolism mediates oxidative stress and inflammation in fatty liver. J Clin Invest. 125(12):4447–62.
203. Linke A, Adams V, Schulze PC, Erbs S, Gielen S, Fiehn E, et al. Antioxidative effects of exercise training in patients with chronic heart failure: increase in radical scavenger enzyme activity in skeletal muscle. Circulation. 2005 Apr 12;111(14):1763–70.
204. Bazil JN, Beard DA, Vinnakota KC. Catalytic Coupling of Oxidative Phosphorylation, ATP Demand, and Reactive Oxygen Species Generation. Biophys J. 2016 Feb 23;110(4):962–71.
205. Beard DA. A biophysical model of the mitochondrial respiratory system and oxidative phosphorylation. PLoS Comput Biol. 2005 Sep;1(4):e36.
206. Liu S-S. Mitochondrial Q cycle-derived superoxide and chemiosmotic bioenergetics. Ann N Y Acad Sci. 2010 Jul;1201:84–95.
207. Selivanov VA, Votyakova TV, Pivtoraiko VN, Zeak J, Sukhomlin T, Trucco M, et al. Reactive oxygen species production by forward and reverse electron fluxes in the mitochondrial respiratory chain. PLoS Comput Biol. 2011 Mar;7(3):e1001115.
208. Chouchani ET, Pell VR, Gaude E, Aksentijević D, Sundier SY, Robb EL, et al. Ischaemic accumulation of succinate controls reperfusion injury through mitochondrial ROS. Nature. 2014 Nov 20;515(7527):431–5.
209. Valls-Lacalle L, Barba I, Miró-Casas E, Alburquerque-Béjar JJ, Ruiz-Meana M, Fuertes-Agudo M, et al. Succinate dehydrogenase inhibition with malonate during reperfusion reduces infarct size by preventing mitochondrial permeability transition. Cardiovasc Res. 2016 Mar 1;109(3):374–84.
210. Park J, Lee J, Choi C. Mitochondrial Network Determines Intracellular ROS Dynamics and Sensitivity to Oxidative Stress through Switching Inter-Mitochondrial Messengers. PLoS One [Internet]. 2011 Aug 4 [cited 2016 Sep 6];6(8). Available from: http://www.ncbi.nlm.nih.gov/pmc/articles/PMC3150422/
211. Maianski NA, Geissler J, Srinivasula SM, Alnemri ES, Roos D, Kuijpers TW. Functional characterization of mitochondria in neutrophils: a role restricted to apoptosis. Cell Death Differ. 2004 Feb;11(2):143–53.
212. Parra Cid T, Conejo García JR, Carballo Alvarez F, de Arriba G. Antioxidant nutrients protect against cyclosporine A nephrotoxicity. Toxicology. 2003 Jul 15;189(1–2):99–111.
213. Hamon J, Jennings P, Bois FY. Systems biology modeling of omics data: effect of cyclosporine a on the Nrf2 pathway in human renal cells. BMC Syst Biol. 2014;8:76.
214. Wilmes A, Limonciel A, Aschauer L, Moenks K, Bielow C, Leonard MO, et al. Application of integrated transcriptomic, proteomic and metabolomic profiling for the delineation of mechanisms of drug induced cell stress. J Proteomics. 2013 Feb 21;79:180–94.
215. Zhang Q, Pi J, Woods CG, Andersen ME. Phase I to II cross-induction of xenobiotic metabolizing enzymes: a feedforward control mechanism for potential hormetic responses. Toxicol Appl Pharmacol. 2009 Jun 15;237(3):345–56.
216. Henderson LM, Chappel JB. NADPH oxidase of neutrophils. Biochim Biophys Acta. 1996 Feb 15;1273(2):87–107.
217. Wymann MP, Kernen P, Deranleau DA, Baggiolini M. Respiratory burst oscillations in human neutrophils and their correlation with fluctuations in apparent cell shape. J Biol Chem. 1989 Sep 25;264(27):15829–34.
218. Olsen LF, Kummer U, Kindzelskii AL, Petty HR. A Model of the Oscillatory Metabolism of Activated Neutrophils. Biophys J. 2003 Jan;84(1):69–81.

219. Petty HR. Neutrophil oscillations: temporal and spatiotemporal aspects of cell behavior. Immunol Res. 2001;23(1):85–94.
220. Recchioni R, Marcheselli F, Moroni F, Gáspár R, Damjanovich S, Pieri C. Melatonin increases the intensity of respiratory burst and prevents L-selectin shedding in human neutrophils in vitro. Biochem Biophys Res Commun. 1998 Nov 9;252(1):20–4.
221. Meier B, Radeke HH, Selle S, Younes M, Sies H, Resch K, et al. Human fibroblasts release reactive oxygen species in response to interleukin-1 or tumour necrosis factor-alpha. Biochem J. 1989 Oct 15;263(2):539–45.
222. Thannickal VJ, Fanburg BL. Activation of an H2O2-generating NADH oxidase in human lung fibroblasts by transforming growth factor beta 1. J Biol Chem. 1995 Dec 22;270(51):30334–8.
223. Haack F, Lemcke H, Ewald R, Rharass T, Uhrmacher AM. Spatio-temporal Model of Endogenous ROS and Raft-Dependent WNT/Beta-Catenin Signaling Driving Cell Fate Commitment in Human Neural Progenitor Cells. PLoS Comput Biol [Internet]. 2015 Mar 20 [cited 2016 Sep 6];11(3). Available from: http://www.ncbi.nlm.nih.gov/pmc/articles/PMC4368204/
224. Funato Y, Michiue T, Asashima M, Miki H. The thioredoxin-related redox-regulating protein nucleoredoxin inhibits Wnt-beta-catenin signalling through dishevelled. Nat Cell Biol. 2006 May;8(5):501–8.
225. Rharass T, Lemcke H, Lantow M, Kuznetsov SA, Weiss DG, Panáková D. Ca2+-mediated mitochondrial reactive oxygen species metabolism augments Wnt/β-catenin pathway activation to facilitate cell differentiation. J Biol Chem. 2014 Oct 3;289(40):27937–51.
226. Dwivedi G, Gran MA, Bagchi P, Kemp ML. Dynamic Redox Regulation of IL-4 Signaling. PLoS Comput Biol. 2015 Nov;11(11):e1004582.
227. Sharma P, Chakraborty R, Wang L, Min B, Tremblay ML, Kawahara T, et al. Redox Regulation of Interleukin-4 Signaling. Immunity. 2008 Oct;29(4):551–64.
228. Smith GR, Shanley DP. Computational modelling of the regulation of Insulin signalling by oxidative stress. BMC Syst Biol. 2013;7:41.
229. Sedaghat AR, Sherman A, Quon MJ. A mathematical model of metabolic insulin signaling pathways. Am J Physiol Endocrinol Metab. 2002 Nov;283(5):E1084-1101.
230. Mahadev K, Zilbering A, Zhu L, Goldstein BJ. Insulin-stimulated hydrogen peroxide reversibly inhibits protein-tyrosine phosphatase 1b in vivo and enhances the early insulin action cascade. J Biol Chem. 2001 Jun 15;276(24):21938–42.
231. Wang L, Brugge JS, Janes KA. Intersection of FOXO- and RUNX1-mediated gene expression programs in single breast epithelial cells during morphogenesis and tumor progression. Proc Natl Acad Sci USA. 2011 Oct 4;108(40):E803-812.
232. Zeigler AC, Richardson WJ, Holmes JW, Saucerman JJ. A computational model of cardiac fibroblast signaling predicts context-dependent drivers of myofibroblast differentiation. J Mol Cell Cardiol. 2016 May;94:72–81.
233. Moreo A, Ambrosio G, De Chiara B, Pu M, Tran T, Mauri F, et al. Influence of myocardial fibrosis on left ventricular diastolic function: noninvasive assessment by cardiac magnetic resonance and echo. Circ Cardiovasc Imaging. 2009 Nov;2(6):437–43.
234. Kraeutler MJ, Soltis AR, Saucerman JJ. Modeling cardiac β-adrenergic signaling with normalized-Hill differential equations: comparison with a biochemical model. BMC Syst Biol. 2010;4:157.
235. Schreck R, Rieber P, Baeuerle PA. Reactive oxygen intermediates as apparently widely used messengers in the activation of the NF-kappa B transcription factor and HIV-1. EMBO J. 1991 Aug;10(8):2247–58.
236. Wong GH, Goeddel DV. Induction of manganous superoxide dismutase by tumor necrosis factor: possible protective mechanism. Science. 1988 Nov 11;242(4880):941–4.

237. Finn NA, Kemp ML. Pro-oxidant and antioxidant effects of N-acetylcysteine regulate doxorubicin-induced NF-kappa B activity in leukemic cells. Mol Biosyst. 2012 Feb;8(2):650–62.
238. Schwarz KB. Oxidative stress during viral infection: a review. Free Radic Biol Med. 1996;21(5):641–9.
239. Bajikar SS, Janes KA. Multiscale models of cell signaling. Ann Biomed Eng. 2012 Nov;40(11):2319–27.
240. Wang C-C, Jamal L, Janes KA. Normal morphogenesis of epithelial tissues and progression of epithelial tumors. Wiley Interdiscip Rev Syst Biol Med. 2012 Feb;4(1):51–78.
241. Anderson ARA, Weaver AM, Cummings PT, Quaranta V. Tumor morphology and phenotypic evolution driven by selective pressure from the microenvironment. Cell. 2006 Dec 1;127(5):905–15.
242. Chitforoushzadeh Z, Ye Z, Sheng Z, LaRue S, Fry RC, Lauffenburger DA, et al. TNF-insulin crosstalk at the transcription factor GATA6 is revealed by a model that links signaling and transcriptomic data tensors. Sci Signal. 2016;9(431):ra59.
243. Kim H-J, Ha S, Lee HY, Lee K-J. ROSics: chemistry and proteomics of cysteine modifications in redox biology. Mass Spectrom Rev. 2015 Apr;34(2):184–208.
244. Nieborowska-Skorska M, Flis S, Skorski T. AKT-induced reactive oxygen species generate imatinib-resistant clones emerging from chronic myeloid leukemia progenitor cells. Leukemia. 2014 Dec;28(12):2416–8.
245. Okon IS, Coughlan KA, Zhang M, Wang Q, Zou M-H. Gefitinib-mediated reactive oxygen specie (ROS) instigates mitochondrial dysfunction and drug resistance in lung cancer cells. J Biol Chem. 2015 Apr 3;290(14):9101–10.
246. Bresciani G, Cruz IBM, de Paz JA, Cuevas MJ, González-Gallego J. The MnSOD Ala16Val SNP: relevance to human diseases and interaction with environmental factors. Free Radic Res. 2013 Oct;47(10):781–92.
247. Meijles DN, Fan LM, Ghazaly MM, Howlin B, Krönke M, Brooks G, et al. p22phox C242T Single-Nucleotide Polymorphism Inhibits Inflammatory Oxidative Damage to Endothelial Cells and Vessels. Circulation. 2016 Jun 14;133(24):2391–403.
248. Shen D, Wu G, Suk H-I. Deep Learning in Medical Image Analysis. Annu Rev Biomed Eng. 2017 Jun 21;19:221–48.
249. Haralick RM, Shapiro LG. Image segmentation techniques. Computer Vision, Graphics, and Image Processing. 1985 Jan 1;29(1):100–32.
250. Haralick RM, Shanmugam K, Dinstein I. Textural Features for Image Classification. IEEE Transactions on Systems, Man, and Cybernetics. 1973 Nov;SMC-3(6):610–21.
251. Bajikar SS, Wang C-C, Borten MA, Pereira EJ, Atkins KA, Janes KA. Tumor Suppressor Inactivation of GDF11 Occurs by Precursor Sequestration in Triple-Negative Breast Cancer. Dev Cell. 2017 Nov 20;43(4):418-435.e13.
252. Fried R, Dehling H. Robust nonparametric tests for the two-sample location problem. Stat Methods Appl. 2011 Nov 1;20(4):409–22.
253. Vonesch C, Aguet F, Vonesch J-L, Unser M. The colored revolution of bioimaging. IEEE Signal Processing Magazine. 2006 May;23(3):20–31.
254. Canny J. A Computational Approach to Edge Detection. IEEE Transactions on Pattern Analysis and Machine Intelligence. 1986 Nov;PAMI-8(6):679–98.
255. Chen S-C, Zhao T, Gordon GJ, Murphy RF. A Novel Graphical Model Approach to Segmenting Cell Images. In: 2006 IEEE Symposium on Computational Intelligence and Bioinformatics and Computational Biology. 2006. p. 1–8.
256. Wählby C, Sintorn I-M, Erlandsson F, Borgefors G, Bengtsson E. Combining intensity, edge and shape information for 2D and 3D segmentation of cell nuclei in tissue sections. J Microsc. 2004 Jul;215(Pt 1):67–76.

257. Subbarao M, Choi T-S, Nikzad A. Focusing techniques. OE. 1993 Nov;32(11):2824–37.
258. McQuin C, Goodman A, Chernyshev V, Kamentsky L, Cimini BA, Karhohs KW, et al. CellProfiler 3.0: Next-generation image processing for biology. PLoS Biol. 2018;16(7):e2005970.
259. Ho J, Parwani AV, Jukic DM, Yagi Y, Anthony L, Gilbertson JR. Use of whole slide imaging in surgical pathology quality assurance: design and pilot validation studies. Hum Pathol. 2006 Mar;37(3):322–31.
260. Lewis JSJ, Ali S, Luo J, Thorstad WL, Madabhushi A. A Quantitative Histomorphometric Classifier (QuHbIC) Identifies Aggressive Versus Indolent p16-Positive Oropharyngeal Squamous Cell Carcinoma. The American Journal of Surgical Pathology. 2014 Jan;38(1):128.
261. Kong J, Cooper LAD, Wang F, Gao J, Teodoro G, Scarpace L, et al. Machine-Based Morphologic Analysis of Glioblastoma Using Whole-Slide Pathology Images Uncovers Clinically Relevant Molecular Correlates. PLOS ONE. 2013 Nov 13;8(11):e81049.
262. Lee G, Sparks R, Ali S, Shih NNC, Feldman MD, Spangler E, et al. Co-occurring gland angularity in localized subgraphs: predicting biochemical recurrence in intermediate-risk prostate cancer patients. PLoS ONE. 2014;9(5):e97954.
263. Xin Yao. Evolving artificial neural networks. Proceedings of the IEEE. 1999 Sep;87(9):1423–47.
264. Krizhevsky A, Sutskever I, Hinton GE. ImageNet Classification with Deep Convolutional Neural Networks. In: Pereira F, Burges CJC, Bottou L, Weinberger KQ, editors. Advances in Neural Information Processing Systems 25 [Internet]. Curran Associates, Inc.; 2012 [cited 2019 Dec 31]. p. 1097–1105. Available from: http://papers.nips.cc/paper/4824-imagenet-classification-with-deep-convolutional-neural-networks.pdf
265. LeCun Y, Bengio Y, Hinton G. Deep learning. Nature. 2015 May 28;521(7553):436–44.
266. Bishop CM, Bishop P of NCCM. Neural Networks for Pattern Recognition. Clarendon Press; 1995. 501 p.
267. Glorot X, Bordes A, Bengio Y. Deep Sparse Rectifier Neural Networks. In: Proceedings of the Fourteenth International Conference on Artificial Intelligence and Statistics [Internet]. 2011 [cited 2020 Jan 2]. p. 315–23. Available from: http://proceedings.mlr.press/v15/glorot11a.html
268. Dahl GE, Sainath TN, Hinton GE. Improving deep neural networks for LVCSR using rectified linear units and dropout. In: 2013 IEEE International Conference on Acoustics, Speech and Signal Processing. 2013. p. 8609–13.
269. Bishop CM. Pattern recognition and machine learning. New York: Springer; 2006. 738 p. (Information science and statistics).
270. Deng L. A tutorial survey of architectures, algorithms, and applications for deep learning. APSIPA Transactions on Signal and Information Processing [Internet]. 2014 ed [cited 2020 Jan 3];3. Available from: https://www.cambridge.org/core/journals/apsipa-transactions-on-signal-and-information-processing/article/tutorial-survey-of-architectures-algorithms-and-applications-for-deep-learning/023B6ADF962FA37F8EC684B209E3DFAE
271. Zarella MD, Bowman D, Aeffner F, Farahani N, Xthona A, Absar SF, et al. A Practical Guide to Whole Slide Imaging: A White Paper From the Digital Pathology Association. Arch Pathol Lab Med. 2019;143(2):222–34.
272. A BEAP, C P, Carolina M. A study of the behavior of several methods for balancing machine learning training data. ACM SIGKDD Explorations Newsletter [Internet]. 2004 Jun 1 [cited 2019 Dec 31]; Available from: https://dl.acm.org/doi/abs/10.1145/1007730.1007735
273. Widrow B, Lehr MA. 30 years of adaptive neural networks: perceptron, Madaline, and backpropagation. Proceedings of the IEEE. 1990 Sep;78(9):1415–42.

274. Rumelhart DE, Hinton GE, Williams RJ. Learning representations by back-propagating errors. Nature. 1986 Oct;323(6088):533–6.
275. Thimm G, Fiesler E. Neural network initialization. In: Mira J, Sandoval F, editors. From Natural to Artificial Neural Computation. Berlin, Heidelberg: Springer; 1995. p. 535–42. (Lecture Notes in Computer Science).
276. Kline DM, Berardi VL. Revisiting squared-error and cross-entropy functions for training neural network classifiers. Neural Comput & Applic. 2005 Dec 1;14(4):310–8.
277. Baum EB, Wilczek F. Supervised Learning of Probability Distributions by Neural Networks. In: Anderson DZ, editor. Neural Information Processing Systems [Internet]. American Institute of Physics; 1988 [cited 2019 Dec 31]. p. 52–61. Available from: http://papers.nips.cc/paper/3-supervised-learning-of-probability-distributions-by-neural-networks.pdf
278. Robbins H, Monro S. A Stochastic Approximation Method. The Annals of Mathematical Statistics. 1951;22(3):400–7.
279. Baratloo A, Hosseini M, Negida A, El Ashal G. Part 1: Simple Definition and Calculation of Accuracy, Sensitivity and Specificity. Emerg (Tehran). 2015;3(2):48–9.
280. Cancer Facts & Figures 2016 | American Cancer Society [Internet]. [cited 2020 Jan 3]. Available from: https://www.cancer.org/research/cancer-facts-statistics/all-cancer-facts-figures/cancer-facts-figures-2016.html
281. Rogers HW, Weinstock MA, Feldman SR, Coldiron BM. Incidence Estimate of Nonmelanoma Skin Cancer (Keratinocyte Carcinomas) in the U.S. Population, 2012. JAMA Dermatol. 2015 Oct;151(10):1081–6.
282. Stern RS. Prevalence of a history of skin cancer in 2007: results of an incidence-based model. Arch Dermatol. 2010 Mar;146(3):279–82.
283. Feramisco JD, Sadreyev RI, Murray ML, Grishin NV, Tsao H. Phenotypic and genotypic analyses of genetic skin disease through the Online Mendelian Inheritance in Man (OMIM) database. J Invest Dermatol. 2009 Nov;129(11):2628–36.
284. Ronneberger O, Fischer P, Brox T. U-Net: Convolutional Networks for Biomedical Image Segmentation. arXiv:150504597 [cs] [Internet]. 2015 May 18 [cited 2020 Jan 3]; Available from: http://arxiv.org/abs/1505.04597
285. Mehregan AH, Brownstein MH. Pilar Sheath Acanthoma. Arch Dermatol. 1978 Oct 1;114(10):1495–7.
286. Breathnach SM, Wells GC. Acanthosis palmaris: tripe palms. Clinical and Experimental Dermatology. 1980;5(2):181–9.
287. He K, Zhang X, Ren S, Sun J. Spatial Pyramid Pooling in Deep Convolutional Networks for Visual Recognition. arXiv:14064729 [cs]. 2014;8691:346–61.
288. Gut G, Herrmann MD, Pelkmans L. Multiplexed protein maps link subcellular organization to cellular states. Science [Internet]. 2018 Aug 3 [cited 2020 Jan 4];361(6401). Available from: https://science.sciencemag.org/content/361/6401/eaar7042
289. Frei AP, Bava F-A, Zunder ER, Hsieh EWY, Chen S-Y, Nolan GP, et al. Highly multiplexed simultaneous detection of RNAs and proteins in single cells. Nat Methods. 2016 Mar;13(3):269–75.
290. Lin J-R, Izar B, Wang S, Yapp C, Mei S, Shah PM, et al. Highly multiplexed immunofluorescence imaging of human tissues and tumors using t-CyCIF and conventional optical microscopes. Elife. 2018 11;7.
291. Grys BT, Lo DS, Sahin N, Kraus OZ, Morris Q, Boone C, et al. Machine learning and computer vision approaches for phenotypic profiling. J Cell Biol. 2017 Jan 2;216(1):65–71.
292. Levsky JM, Shenoy SM, Pezo RC, Singer RH. Single-cell gene expression profiling. Science. 2002 Aug 2;297(5582):836–40.

293. Wang G, Moffitt JR, Zhuang X. Multiplexed imaging of high-density libraries of RNAs with MERFISH and expansion microscopy. Scientific Reports. 2018 Mar 19;8(1):1–13.

294. Pichon X, Lagha M, Mueller F, Bertrand E. A Growing Toolbox to Image Gene Expression in Single Cells: Sensitive Approaches for Demanding Challenges. Molecular Cell. 2018 Aug;71(3):468–80.

295. Simonyan K, Zisserman A. Very Deep Convolutional Networks for Large-Scale Image Recognition. arXiv:14091556 [cs] [Internet]. 2015 Apr 10 [cited 2020 Jan 5]; Available from: http://arxiv.org/abs/1409.1556

296. Szegedy C, Liu W, Jia Y, Sermanet P, Reed S, Anguelov D, et al. Going Deeper with Convolutions. arXiv:14094842 [cs] [Internet]. 2014 Sep 16 [cited 2020 Jan 5]; Available from: http://arxiv.org/abs/1409.4842

297. He K, Zhang X, Ren S, Sun J. Deep Residual Learning for Image Recognition. arXiv:151203385 [cs] [Internet]. 2015 Dec 10 [cited 2020 Jan 5]; Available from: http://arxiv.org/abs/1512.03385

298. Halevy A, Norvig P, Pereira F. The Unreasonable Effectiveness of Data. IEEE Intelligent Systems. 2009 Mar;24(2):8–12.

299. Leevy JL, Khoshgoftaar TM, Bauder RA, Seliya N. A survey on addressing high-class imbalance in big data. Journal of Big Data. 2018 Nov 1;5(1):42.

300. Sun C, Shrivastava A, Singh S, Gupta A. Revisiting Unreasonable Effectiveness of Data in Deep Learning Era. arXiv:170702968 [cs] [Internet]. 2017 Aug 3 [cited 2020 Jan 5]; Available from: http://arxiv.org/abs/1707.02968

301. Esteva A, Kuprel B, Novoa RA, Ko J, Swetter SM, Blau HM, et al. Dermatologist-level classification of skin cancer with deep neural networks. Nature. 2017 Feb;542(7639):115–8.

302. Rajpurkar P, Irvin J, Zhu K, Yang B, Mehta H, Duan T, et al. CheXNet: Radiologist-Level Pneumonia Detection on Chest X-Rays with Deep Learning. arXiv:171105225 [cs, stat] [Internet]. 2017 Dec 25 [cited 2020 Jan 5]; Available from: http://arxiv.org/abs/1711.05225

303. Hawkins DM. The Problem of Overfitting. Journal of Chemical Information and Computer Sciences. 2004 Jan;44(1):1–12.

304. Tanner MA, Wong WH. The Calculation of Posterior Distributions by Data Augmentation. Journal of the American Statistical Association. 1987 Jun 1;82(398):528–40.

305. Ho D, Liang E, Stoica I, Abbeel P, Chen X. Population Based Augmentation: Efficient Learning of Augmentation Policy Schedules. arXiv:190505393 [cs, stat] [Internet]. 2019 May 14 [cited 2020 Jan 5]; Available from: http://arxiv.org/abs/1905.05393

306. Wong SC, Gatt A, Stamatescu V, McDonnell MD. Understanding Data Augmentation for Classification: When to Warp? In: 2016 International Conference on Digital Image Computing: Techniques and Applications (DICTA). 2016. p. 1–6.

307. Bengio Y, Courville A, Vincent P. Representation Learning: A Review and New Perspectives. arXiv:12065538 [cs] [Internet]. 2014 Apr 23 [cited 2020 Jan 8]; Available from: http://arxiv.org/abs/1206.5538

308. Russakovsky O, Deng J, Su H, Krause J, Satheesh S, Ma S, et al. ImageNet Large Scale Visual Recognition Challenge. Int J Comput Vis. 2015 Dec 1;115(3):211–52.

309. Clark K, Vendt B, Smith K, Freymann J, Kirby J, Koppel P, et al. The Cancer Imaging Archive (TCIA): Maintaining and Operating a Public Information Repository. J Digit Imaging. 2013 Dec;26(6):1045–57.

310. Bankhead P, Loughrey MB, Fernández JA, Dombrowski Y, McArt DG, Dunne PD, et al. QuPath: Open source software for digital pathology image analysis. Scientific Reports. 2017 Dec 4;7(1):1–7.

311. Medina D. The mammary gland: a unique organ for the study of development and tumorigenesis. J Mammary Gland Biol Neoplasia. 1996 Jan;1(1):5–19.

312. Paine IS, Lewis MT. The Terminal End Bud: the Little Engine that Could. J Mammary Gland Biol Neoplasia. 2017 Jun;22(2):93–108.
313. Ewald AJ, Brenot A, Duong M, Chan BS, Werb Z. Collective epithelial migration and cell rearrangements drive mammary branching morphogenesis. Dev Cell. 2008 Apr;14(4):570–81.
314. Brisken C, O'Malley B. Hormone action in the mammary gland. Cold Spring Harb Perspect Biol. 2010 Dec;2(12):a003178.
315. Sternlicht MD. Key stages in mammary gland development: the cues that regulate ductal branching morphogenesis. Breast Cancer Res. 2006;8(1):201.
316. Sympson CJ, Talhouk RS, Alexander CM, Chin JR, Clift SM, Bissell MJ, et al. Targeted expression of stromelysin-1 in mammary gland provides evidence for a role of proteinases in branching morphogenesis and the requirement for an intact basement membrane for tissue-specific gene expression. J Cell Biol. 1994 May;125(3):681–93.
317. Huebner RJ, Lechler T, Ewald AJ. Developmental stratification of the mammary epithelium occurs through symmetry-breaking vertical divisions of apically positioned luminal cells. Development. 2014 Mar;141(5):1085–94.
318. Mailleux AA, Overholtzer M, Schmelzle T, Bouillet P, Strasser A, Brugge JS. BIM regulates apoptosis during mammary ductal morphogenesis, and its absence reveals alternative cell death mechanisms. Dev Cell. 2007 Feb;12(2):221–34.
319. Hasegawa D, Calvo V, Avivar-Valderas A, Lade A, Chou HI, Lee YA, et al. Epithelial Xbp1 is required for cellular proliferation and differentiation during mammary gland development. Mol Cell Biol. 2015 May;35(9):1543–56.
320. Avivar-Valderas A, Wen HC, Aguirre-Ghiso JA. Stress signaling and the shaping of the mammary tissue in development and cancer. Oncogene. 2014 Nov 27;33(48):5483–90.
321. Wang C-C, Jamal L, Janes KA. Normal morphogenesis of epithelial tissues and progression of epithelial tumors. Wiley Interdiscip Rev Syst Biol Med. 2012 Feb;4(1):51–78.
322. Feigin ME, Muthuswamy SK. Polarity proteins regulate mammalian cell-cell junctions and cancer pathogenesis. Curr Opin Cell Biol. 2009 Oct;21(5):694–700.
323. Debnath J, Brugge JS. Modelling glandular epithelial cancers in three-dimensional cultures. Nat Rev Cancer. 2005 Sep;5(9):675–88.
324. Shamir ER, Ewald AJ. Three-dimensional organotypic culture: experimental models of mammalian biology and disease. Nat Rev Mol Cell Biol. 2014 Oct;15(10):647–64.
325. Lee GY, Kenny PA, Lee EH, Bissell MJ. Three-dimensional culture models of normal and malignant breast epithelial cells. Nature methods. 2007 Apr;4(4):359–65.
326. Wang H, Lacoche S, Huang L, Xue B, Muthuswamy SK. Rotational motion during three-dimensional morphogenesis of mammary epithelial acini relates to laminin matrix assembly. Proc Natl Acad Sci U S A. 2013 Jan 2;110(1):163–8.
327. Jarde T, Lloyd-Lewis B, Thomas M, Kendrick H, Melchor L, Bougaret L, et al. Wnt and Neuregulin1/ErbB signalling extends 3D culture of hormone responsive mammary organoids. Nat Commun. 2016 Oct 26;7:13207.
328. Jamieson PR, Dekkers JF, Rios AC, Fu NY, Lindeman GJ, Visvader JE. Derivation of a robust mouse mammary organoid system for studying tissue dynamics. Development. 2017 Mar 15;144(6):1065–71.
329. Sachs N, de Ligt J, Kopper O, Gogola E, Bounova G, Weeber F, et al. A Living Biobank of Breast Cancer Organoids Captures Disease Heterogeneity. Cell. 2018 Jan 11;172(1–2):373-386 e10.
330. Janes KA, Wang CC, Holmberg KJ, Cabral K, Brugge JS. Identifying single-cell molecular programs by stochastic profiling. Nat Methods. 2010 Apr;7(4):311–7.

331. Wang L, Brugge JS, Janes KA. Intersection of FOXO- and RUNX1-mediated gene expression programs in single breast epithelial cells during morphogenesis and tumor progression. Proc Natl Acad Sci USA. 2011 Oct 4;108(40):E803-812.
332. Debnath J, Mills KR, Collins NL, Reginato MJ, Muthuswamy SK, Brugge JS. The role of apoptosis in creating and maintaining luminal space within normal and oncogene-expressing mammary acini. Cell. 2002 Oct 4;111(1):29–40.
333. Wang CC, Bajikar SS, Jamal L, Atkins KA, Janes KA. A time- and matrix-dependent TGFBR3-JUND-KRT5 regulatory circuit in single breast epithelial cells and basal-like premalignancies. Nat Cell Biol. 2014 Apr;16(4):345–56.
334. Bajikar SS, Wang CC, Borten MA, Pereira EJ, Atkins KA, Janes KA. Tumor-Suppressor Inactivation of GDF11 Occurs by Precursor Sequestration in Triple-Negative Breast Cancer. Dev Cell. 2017 Nov 20;43(4):418-435 e13.
335. Gerald D, Berra E, Frapart YM, Chan DA, Giaccia AJ, Mansuy D, et al. JunD reduces tumor angiogenesis by protecting cells from oxidative stress. Cell. 2004 Sep 17;118(6):781–94.
336. O'Reilly MA. Redox activation of p21Cip1/WAF1/Sdi1: a multifunctional regulator of cell survival and death. Antioxid Redox Signal. 2005 Jan;7(1–2):108–18.
337. Minocherhomji S, Ying S, Bjerregaard VA, Bursomanno S, Aleliunaite A, Wu W, et al. Replication stress activates DNA repair synthesis in mitosis. Nature. 2015 Dec 10;528(7581):286–90.
338. Czarnecka AM, Campanella C, Zummo G, Cappello F. Mitochondrial chaperones in cancer: from molecular biology to clinical diagnostics. Cancer Biol Ther. 2006 Jul;5(7):714–20.
339. Tanioka M, Fan C, Parker JS, Hoadley KA, Hu Z, Li Y, et al. Integrated Analysis of RNA and DNA from the Phase III Trial CALGB 40601 Identifies Predictors of Response to Trastuzumab-Based Neoadjuvant Chemotherapy in HER2-Positive Breast Cancer. Clin Cancer Res. 2018 Nov 1;24(21):5292–304.
340. Sykiotis GP, Bohmann D. Stress-activated cap'n'collar transcription factors in aging and human disease. Sci Signal. 2010 Mar 9;3(112):re3.
341. Rojo de la Vega M, Chapman E, Zhang DD. NRF2 and the Hallmarks of Cancer. Cancer Cell. 2018 Jul 9;34(1):21–43.
342. Sharpless NE, DePinho RA. p53: good cop/bad cop. Cell. 2002 Jul 12;110(1):9–12.
343. Bajikar SS, Fuchs C, Roller A, Theis FJ, Janes KA. Parameterizing cell-to-cell regulatory heterogeneities via stochastic transcriptional profiles. Proc Natl Acad Sci U S A. 2014 Feb 4;111(5):E626-35.
344. Shalek AK, Satija R, Adiconis X, Gertner RS, Gaublomme JT, Raychowdhury R, et al. Single-cell transcriptomics reveals bimodality in expression and splicing in immune cells. Nature. 2013 Jun 13;498(7453):236–40.
345. Gotea V, Ovcharenko I. DiRE: identifying distant regulatory elements of co-expressed genes. Nucleic Acids Res. 2008 Jul 1;36(Web Server issue):W133–9.
346. Chen EY, Xu H, Gordonov S, Lim MP, Perkins MH, Ma'ayan A. Expression2Kinases: mRNA profiling linked to multiple upstream regulatory layers. Bioinformatics. 2012 Jan 1;28(1):105–11.
347. Bailey TL, Johnson J, Grant CE, Noble WS. The MEME Suite. Nucleic Acids Res. 2015 Jul 1;43(W1):W39-49.
348. Kwon AT, Arenillas DJ, Worsley Hunt R, Wasserman WW. oPOSSUM-3: advanced analysis of regulatory motif over-representation across genes or ChIP-Seq datasets. G3 (Bethesda). 2012 Sep;2(9):987–1002.
349. Kleinman HK, Martin GR. Matrigel: basement membrane matrix with biological activity. Semin Cancer Biol. 2005 Oct;15(5):378–86.

350. Singh S, Wang L, Schaff DL, Sutcliffe MD, Koeppel AF, Kim J, et al. In situ 10-cell RNA sequencing in tissue and tumor biopsy samples. Sci Rep. 2019 Mar 20;9(1):4836.
351. The Gene Ontology C. The Gene Ontology Resource: 20 years and still GOing strong. Nucleic Acids Res. 2019 Jan 8;47(D1):D330–8.
352. Loewer A, Batchelor E, Gaglia G, Lahav G. Basal dynamics of p53 reveal transcriptionally attenuated pulses in cycling cells. Cell. 2010 Jul 9;142(1):89–100.
353. Zhang Y, Yan W, Chen X. Mutant p53 disrupts MCF-10A cell polarity in three-dimensional culture via epithelial-to-mesenchymal transitions. J Biol Chem. 2011 May 6;286(18):16218–28.
354. Bowman T, Symonds H, Gu L, Yin C, Oren M, Van Dyke T. Tissue-specific inactivation of p53 tumor suppression in the mouse. Genes Dev. 1996 Apr 1;10(7):826–35.
355. Faraonio R, Vergara P, Di Marzo D, Pierantoni MG, Napolitano M, Russo T, et al. p53 suppresses the Nrf2-dependent transcription of antioxidant response genes. J Biol Chem. 2006 Dec 29;281(52):39776–84.
356. Munger K, Werness BA, Dyson N, Phelps WC, Harlow E, Howley PM. Complex formation of human papillomavirus E7 proteins with the retinoblastoma tumor suppressor gene product. EMBO J. 1989 Dec 20;8(13):4099–105.
357. Miller FR, Santner SJ, Tait L, Dawson PJ. MCF10DCIS.com xenograft model of human comedo ductal carcinoma in situ. Journal of the National Cancer Institute. 2000 Jul 19;92(14):1185–6.
358. Hu M, Yao J, Carroll DK, Weremowicz S, Chen H, Carrasco D, et al. Regulation of in situ to invasive breast carcinoma transition. Cancer cell. 2008 May;13(5):394–406.
359. Dawson PJ, Wolman SR, Tait L, Heppner GH, Miller FR. MCF10AT: a model for the evolution of cancer from proliferative breast disease. Am J Pathol. 1996 Jan;148(1):313–9.
360. Wasielewski M, Hanifi-Moghaddam P, Hollestelle A, Merajver SD, van den Ouweland A, Klijn JG, et al. Deleterious CHEK2 1100delC and L303X mutants identified among 38 human breast cancer cell lines. Breast Cancer Res Treat. 2009 Jan;113(2):285–91.
361. Hirao A, Cheung A, Duncan G, Girard PM, Elia AJ, Wakeham A, et al. Chk2 is a tumor suppressor that regulates apoptosis in both an ataxia telangiectasia mutated (ATM)-dependent and an ATM-independent manner. Mol Cell Biol. 2002 Sep;22(18):6521–32.
362. Hong F, Freeman ML, Liebler DC. Identification of sensor cysteines in human Keap1 modified by the cancer chemopreventive agent sulforaphane. Chem Res Toxicol. 2005 Dec;18(12):1917–26.
363. Vassilev LT, Vu BT, Graves B, Carvajal D, Podlaski F, Filipovic Z, et al. In vivo activation of the p53 pathway by small-molecule antagonists of MDM2. Science. 2004 Feb 6;303(5659):844–8.
364. Lane DP. Cancer. p53, guardian of the genome. Nature. 1992 Jul 2;358(6381):15–6.
365. Barr AR, Cooper S, Heldt FS, Butera F, Stoy H, Mansfeld J, et al. DNA damage during S-phase mediates the proliferation-quiescence decision in the subsequent G1 via p21 expression. Nat Commun. 2017 Mar 20;8:14728.
366. Guo Z, Kozlov S, Lavin MF, Person MD, Paull TT. ATM activation by oxidative stress. Science. 2010 Oct 22;330(6003):517–21.
367. Kannan N, Nguyen LV, Makarem M, Dong Y, Shih K, Eirew P, et al. Glutathione-dependent and -independent oxidative stress-control mechanisms distinguish normal human mammary epithelial cell subsets. Proc Natl Acad Sci U S A. 2014 May 27;111(21):7789–94.
368. Molyneux G, Geyer FC, Magnay FA, McCarthy A, Kendrick H, Natrajan R, et al. BRCA1 basal-like breast cancers originate from luminal epithelial progenitors and not from basal stem cells. Cell stem cell. 2010 Sep 3;7(3):403–17.

369. Takahashi N, Chen H-Y, Harris IS, Stover DG, Selfors LM, Bronson RT, et al. Cancer Cells Co-opt the Neuronal Redox-Sensing Channel TRPA1 to Promote Oxidative-Stress Tolerance. Cancer Cell. 2018 11;33(6):985-1003.e7.
370. Markvicheva KN, Bilan DS, Mishina NM, Gorokhovatsky AY, Vinokurov LM, Lukyanov S, et al. A genetically encoded sensor for H2O2 with expanded dynamic range. Bioorg Med Chem. 2011 Feb 1;19(3):1079–84.
371. Lakhani SR, Van De Vijver MJ, Jacquemier J, Anderson TJ, Osin PP, McGuffog L, et al. The pathology of familial breast cancer: predictive value of immunohistochemical markers estrogen receptor, progesterone receptor, HER-2, and p53 in patients with mutations in BRCA1 and BRCA2. J Clin Oncol. 2002 May 1;20(9):2310–8.
372. Karihtala P, Kauppila S, Soini Y, Arja Jukkola V. Oxidative stress and counteracting mechanisms in hormone receptor positive, triple-negative and basal-like breast carcinomas. BMC Cancer. 2011 Jun 21;11:262.
373. Kemmerer ZA, Ader NR, Mulroy SS, Eggler AL. Comparison of human Nrf2 antibodies: A tale of two proteins. Toxicol Lett. 2015 Oct 14;238(2):83–9.
374. Lau A, Tian W, Whitman SA, Zhang DD. The predicted molecular weight of Nrf2: it is what it is not. Antioxid Redox Signal. 2013 Jan 1;18(1):91–3.
375. Maguire SL, Peck B, Wai PT, Campbell J, Barker H, Gulati A, et al. Three-dimensional modelling identifies novel genetic dependencies associated with breast cancer progression in the isogenic MCF10 model. J Pathol. 2016 Nov;240(3):315–28.
376. DeNicola GM, Karreth FA, Humpton TJ, Gopinathan A, Wei C, Frese K, et al. Oncogene-induced Nrf2 transcription promotes ROS detoxification and tumorigenesis. Nature. 2011 Jul 6;475(7354):106–9.
377. Rios AC, Fu NY, Lindeman GJ, Visvader JE. In situ identification of bipotent stem cells in the mammary gland. Nature. 2014 Feb 20;506(7488):322–7.
378. Humphreys RC, Krajewska M, Krnacik S, Jaeger R, Weiher H, Krajewski S, et al. Apoptosis in the terminal endbud of the murine mammary gland: a mechanism of ductal morphogenesis. Development. 1996 Dec;122(12):4013–22.
379. Hennighausen L, Robinson GW. Signaling pathways in mammary gland development. Dev Cell. 2001 Oct;1(4):467–75.
380. Gajewska M, Zielniok K, Motyl T. Autophagy in Development and Remodelling of Mammary Gland. Autophagy - A Double-Edged Sword - Cell Survival or Death? [Internet]. 2013 Apr 17 [cited 2020 Jan 9]; Available from: https://www.intechopen.com/books/autophagy-a-double-edged-sword-cell-survival-or-death-/autophagy-in-development-and-remodelling-of-mammary-gland
381. Fung C, Lock R, Gao S, Salas E, Debnath J. Induction of autophagy during extracellular matrix detachment promotes cell survival. Mol Biol Cell. 2008 Mar;19(3):797–806.
382. Espina V, Mariani BD, Gallagher RI, Tran K, Banks S, Wiedemann J, et al. Malignant precursor cells pre-exist in human breast DCIS and require autophagy for survival. PLoS ONE. 2010 Apr 20;5(4):e10240.
383. Avivar-Valderas A, Salas E, Bobrovnikova-Marjon E, Diehl JA, Nagi C, Debnath J, et al. PERK integrates autophagy and oxidative stress responses to promote survival during extracellular matrix detachment. Mol Cell Biol. 2011 Sep;31(17):3616–29.
384. Jain A, Rusten TE, Katheder N, Elvenes J, Bruun J-A, Sjøttem E, et al. p62/Sequestosome-1, Autophagy-related Gene 8, and Autophagy in Drosophila Are Regulated by Nuclear Factor Erythroid 2-related Factor 2 (NRF2), Independent of Transcription Factor TFEB. J Biol Chem. 2015 Jun 12;290(24):14945–62.
385. Walker A, Singh A, Tully E, Woo J, Le A, Nguyen T, et al. Nrf2 signaling and autophagy are complementary in protecting breast cancer cells during glucose deprivation. Free Radic Biol Med. 2018 20;120:407–13.

386. Tang Z, Hu B, Zang F, Wang J, Zhang X, Chen H. Nrf2 drives oxidative stress-induced autophagy in nucleus pulposus cells via a Keap1/Nrf2/p62 feedback loop to protect intervertebral disc from degeneration. Cell Death Dis. 2019 Jul 1;10(7):510.
387. Bartolini D, Dallaglio K, Torquato P, Piroddi M, Galli F. Nrf2-p62 autophagy pathway and its response to oxidative stress in hepatocellular carcinoma. Transl Res. 2018;193:54–71.
388. el-Deiry WS, Tokino T, Velculescu VE, Levy DB, Parsons R, Trent JM, et al. WAF1, a potential mediator of p53 tumor suppression. Cell. 1993 Nov 19;75(4):817–25.
389. Malhotra D, Portales-Casamar E, Singh A, Srivastava S, Arenillas D, Happel C, et al. Global mapping of binding sites for Nrf2 identifies novel targets in cell survival response through ChIP-Seq profiling and network analysis. Nucleic Acids Res. 2010 Sep;38(17):5718–34.
390. Tanikawa C, Zhang Y-Z, Yamamoto R, Tsuda Y, Tanaka M, Funauchi Y, et al. The Transcriptional Landscape of p53 Signalling Pathway. EBioMedicine. 2017 Jun;20:109–19.
391. Kenzelmann Broz D, Spano Mello S, Bieging KT, Jiang D, Dusek RL, Brady CA, et al. Global genomic profiling reveals an extensive p53-regulated autophagy program contributing to key p53 responses. Genes Dev. 2013 May 1;27(9):1016–31.
392. Pan X, Hobbs RP, Coulombe PA. The expanding significance of keratin intermediate filaments in normal and diseased epithelia. Curr Opin Cell Biol. 2013 Feb;25(1):47–56.
393. Zhou Q, Ji X, Chen L, Greenberg HB, Lu SC, Omary MB. Keratin mutation primes mouse liver to oxidative injury. Hepatology. 2005 Mar;41(3):517–25.
394. Castro NP, Rangel MC, Merchant AS, MacKinnon G, Cuttitta F, Salomon DS, et al. Sulforaphane Suppresses the Growth of Triple-negative Breast Cancer Stem-like Cells In vitro and In vivo. Cancer Prev Res (Phila). 2019 Mar;12(3):147–58.
395. Li Y, Zhang T, Korkaya H, Liu S, Lee HF, Newman B, et al. Sulforaphane, a dietary component of broccoli/broccoli sprouts, inhibits breast cancer stem cells. Clin Cancer Res. 2010 May 1;16(9):2580–90.
396. Zhang C, Wang H-J, Bao Q-C, Wang L, Guo T-K, Chen W-L, et al. NRF2 promotes breast cancer cell proliferation and metastasis by increasing RhoA/ROCK pathway signal transduction. Oncotarget. 2016 Nov 8;7(45):73593–606.
397. Zhang H-S, Zhang Z-G, Du G-Y, Sun H-L, Liu H-Y, Zhou Z, et al. Nrf2 promotes breast cancer cell migration via up-regulation of G6PD/HIF-1α/Notch1 axis. J Cell Mol Med. 2019 May;23(5):3451–63.
398. Yaffe MB. Why geneticists stole cancer research even though cancer is primarily a signaling disease. Sci Signal [Internet]. 2019 Jan 22;12(565). Available from: https://www.ncbi.nlm.nih.gov/pubmed/30670634
399. Sayin VI, Ibrahim MX, Larsson E, Nilsson JA, Lindahl P, Bergo MO. Antioxidants accelerate lung cancer progression in mice. Sci Transl Med. 2014 Jan 29;6(221):221ra15.
400. Moffat J, Grueneberg DA, Yang X, Kim SY, Kloepfer AM, Hinkle G, et al. A lentiviral RNAi library for human and mouse genes applied to an arrayed viral high-content screen. Cell. 2006 Mar 24;124(6):1283–98.
401. Yang X, Boehm JS, Salehi-Ashtiani K, Hao T, Shen Y, Lubonja R, et al. A public genome-scale lentiviral expression library of human ORFs. Nature methods. 2011 Aug;8(8):659–61.
402. Roux KJ, Kim DI, Raida M, Burke B. A promiscuous biotin ligase fusion protein identifies proximal and interacting proteins in mammalian cells. J Cell Biol. 2012 Mar 19;196(6):801–10.
403. Strickland SW, Vande Pol S. The Human Papillomavirus 16 E7 Oncoprotein Attenuates AKT Signaling To Promote Internal Ribosome Entry Site-Dependent Translation and Expression of c-MYC. J Virol. 2016 Jun 15;90(12):5611–21.

404. Debnath J, Muthuswamy SK, Brugge JS. Morphogenesis and oncogenesis of MCF-10A mammary epithelial acini grown in three-dimensional basement membrane cultures. Methods. 2003 Jul;30(3):256–68.
405. Robinson MD, McCarthy DJ, Smyth GK. edgeR: a Bioconductor package for differential expression analysis of digital gene expression data. Bioinformatics. 2010 Jan 1;26(1):139–40.
406. Subramanian A, Tamayo P, Mootha VK, Mukherjee S, Ebert BL, Gillette MA, et al. Gene set enrichment analysis: a knowledge-based approach for interpreting genome-wide expression profiles. Proc Natl Acad Sci U S A. 2005 Oct 25;102(43):15545–50.
407. Liberzon A, Subramanian A, Pinchback R, Thorvaldsdottir H, Tamayo P, Mesirov JP. Molecular signatures database (MSigDB) 3.0. Bioinformatics. 2011 Jun 15;27(12):1739–40.
408. Miller-Jensen K, Janes KA, Brugge JS, Lauffenburger DA. Common effector processing mediates cell-specific responses to stimuli. Nature. 2007 Aug 2;448(7153):604–8.
409. Borten MA, Bajikar SS, Sasaki N, Clevers H, Janes KA. Automated brightfield morphometry of 3D organoid populations by OrganoSeg. Sci Rep. 2018 Mar 28;8(1):5319.
410. Del Castillo P, Llorente AR, Stockert JC. Influence of fixation, exciting light and section thickness on the primary fluorescence of samples for microfluorometric analysis. Basic Appl Histochem. 1989;33(3):251–7.
411. Margolin AA, Nemenman I, Basso K, Wiggins C, Stolovitzky G, Dalla Favera R, et al. ARACNE: an algorithm for the reconstruction of gene regulatory networks in a mammalian cellular context. BMC Bioinformatics. 2006 Mar 20;7 Suppl 1:S7.
412. Janes KA, Reinhardt HC, Yaffe MB. Cytokine-induced signaling networks prioritize dynamic range over signal strength. Cell. 2008 Oct 17;135(2):343–54.
413. Ince RAA, Giordano BL, Kayser C, Rousselet GA, Gross J, Schyns PG. A statistical framework for neuroimaging data analysis based on mutual information estimated via a gaussian copula. Hum Brain Mapp. 2017;38(3):1541–73.
414. Lachmann A, Xu H, Krishnan J, Berger SI, Mazloom AR, Ma'ayan A. ChEA: transcription factor regulation inferred from integrating genome-wide ChIP-X experiments. Bioinformatics. 2010 Oct 1;26(19):2438–44.
415. Bailey TL, Elkan C. Fitting a mixture model by expectation maximization to discover motifs in biopolymers. Proc Int Conf Intell Syst Mol Biol. 1994;2:28–36.
416. Bailey TL, Boden M, Buske FA, Frith M, Grant CE, Clementi L, et al. MEME SUITE: tools for motif discovery and searching. Nucleic Acids Res. 2009 Jul;37(Web Server issue):W202-8.
417. Khan A, Fornes O, Stigliani A, Gheorghe M, Castro-Mondragon JA, van der Lee R, et al. JASPAR 2018: update of the open-access database of transcription factor binding profiles and its web framework. Nucleic Acids Res. 2018 Jan 4;46(D1):D260–6.
418. Kulakovskiy IV, Vorontsov IE, Yevshin IS, Sharipov RN, Fedorova AD, Rumynskiy EI, et al. HOCOMOCO: towards a complete collection of transcription factor binding models for human and mouse via large-scale ChIP-Seq analysis. Nucleic Acids Res. 2018 Jan 4;46(D1):D252–9.
419. Ames BN, Shigenaga MK, Hagen TM. Oxidants, antioxidants, and the degenerative diseases of aging. Proc Natl Acad Sci U S A. 1993 Sep 1;90(17):7915–22.
420. Cooke MS, Evans MD, Dizdaroglu M, Lunec J. Oxidative DNA damage: mechanisms, mutation, and disease. FASEB J. 2003 Jul;17(10):1195–214.
421. Irani K, Xia Y, Zweier JL, Sollott SJ, Der CJ, Fearon ER, et al. Mitogenic Signaling Mediated by Oxidants in Ras-Transformed Fibroblasts. Science. 1997 Mar 14;275(5306):1649–52.

422. Ishikawa K, Takenaga K, Akimoto M, Koshikawa N, Yamaguchi A, Imanishi H, et al. ROS-generating mitochondrial DNA mutations can regulate tumor cell metastasis. Science. 2008 May 2;320(5876):661–4.
423. DeNicola GM, Chen P-H, Mullarky E, Sudderth JA, Hu Z, Wu D, et al. NRF2 regulates serine biosynthesis in non-small cell lung cancer. Nat Genet. 2015 Dec;47(12):1475–81.
424. Poole LB, Karplus PA, Claiborne A. Protein sulfenic acids in redox signaling. Annu Rev Pharmacol Toxicol. 2004;44:325–47.
425. Chio IIC, Tuveson DA. ROS in Cancer: The Burning Question. Trends Mol Med. 2017;23(5):411–29.
426. Vafa O, Wade M, Kern S, Beeche M, Pandita TK, Hampton GM, et al. c-Myc can induce DNA damage, increase reactive oxygen species, and mitigate p53 function: a mechanism for oncogene-induced genetic instability. Mol Cell. 2002 May;9(5):1031–44.
427. Khalil HS, Goltsov A, Langdon SP, Harrison DJ, Bown J, Deeni Y. Quantitative analysis of NRF2 pathway reveals key elements of the regulatory circuits underlying antioxidant response and proliferation of ovarian cancer cells. J Biotechnol. 2015 May 20;202:12–30.
428. Zhang Q, Andersen ME. Dose response relationship in anti-stress gene regulatory networks. PLoS Comput Biol. 2007 Mar 2;3(3):e24.
429. Oshino N, Chance B, Sies H, Bucher T. The role of H 2 O 2 generation in perfused rat liver and the reaction of catalase compound I and hydrogen donors. Arch Biochem Biophys. 1973 Jan;154(1):117–31.
430. Batchelor E, Mock CS, Bhan I, Loewer A, Lahav G. Recurrent initiation: a mechanism for triggering p53 pulses in response to DNA damage. Mol Cell. 2008 May 9;30(3):277–89.
431. Chen W, Sun Z, Wang XJ, Jiang T, Huang Z, Fang D, et al. Direct interaction between Nrf2 and p21(Cip1/WAF1) upregulates the Nrf2-mediated antioxidant response. Mol Cell. 2009 Jun 26;34(6):663–73.
432. Shan Y, Wei Z, Tao L, Wang S, Zhang F, Shen C, et al. Prophylaxis of Diallyl Disulfide on Skin Carcinogenic Model via p21-dependent Nrf2 stabilization. Sci Rep. 2016 Oct 19;6:35676.
433. Kaczara P, Sarna T, Burke JM. Dynamics of H2O2 availability to ARPE-19 cultures in models of oxidative stress. Free Radic Biol Med. 2010 Apr 15;48(8):1064–70.
434. Balleza E, Kim JM, Cluzel P. Systematic characterization of maturation time of fluorescent proteins in living cells. Nat Methods. 2018 Jan;15(1):47–51.
435. Chen W, Sun Z, Wang X-J, Jiang T, Huang Z, Fang D, et al. Direct interaction between Nrf2 and p21(Cip1/WAF1) upregulates the Nrf2-mediated antioxidant response. Mol Cell. 2009 Jun 26;34(6):663–73.
436. Butcher DT, Alliston T, Weaver VM. A tense situation: forcing tumour progression. Nat Rev Cancer. 2009 Feb;9(2):108–22.
437. Keenan AB, Jenkins SL, Jagodnik KM, Koplev S, He E, Torre D, et al. The Library of Integrated Network-Based Cellular Signatures NIH Program: System-Level Cataloging of Human Cells Response to Perturbations. Cell Syst. 2018 Jan 24;6(1):13–24.
438. Thimmulappa RK, Mai KH, Srisuma S, Kensler TW, Yamamoto M, Biswal S. Identification of Nrf2-regulated genes induced by the chemopreventive agent sulforaphane by oligonucleotide microarray. Cancer Res. 2002 Sep 15;62(18):5196–203.
439. Allen MA, Andrysik Z, Dengler VL, Mellert HS, Guarnieri A, Freeman JA, et al. Global analysis of p53-regulated transcription identifies its direct targets and unexpected regulatory mechanisms. Elife. 2014 May 27;3:e02200.
440. Asher G, Lotem J, Cohen B, Sachs L, Shaul Y. Regulation of p53 stability and p53-dependent apoptosis by NADH quinone oxidoreductase 1. Proc Natl Acad Sci USA. 2001 Jan 30;98(3):1188–93.

441. You A, Nam C-W, Wakabayashi N, Yamamoto M, Kensler TW, Kwak M-K. Transcription factor Nrf2 maintains the basal expression of Mdm2: An implication of the regulation of p53 signaling by Nrf2. Arch Biochem Biophys. 2011 Mar 15;507(2):356–64.
442. Faraonio R, Vergara P, Di Marzo D, Pierantoni MG, Napolitano M, Russo T, et al. p53 suppresses the Nrf2-dependent transcription of antioxidant response genes. J Biol Chem. 2006 Dec 29;281(52):39776–84.
443. Hiemstra S, Niemeijer M, Koedoot E, Wink S, Klip JE, Vlasveld M, et al. Comprehensive Landscape of Nrf2 and p53 Pathway Activation Dynamics by Oxidative Stress and DNA Damage. Chem Res Toxicol. 2017 17;30(4):923–33.
444. Rajasekaran NS, Varadharaj S, Khanderao GD, Davidson CJ, Kannan S, Firpo MA, et al. Sustained activation of nuclear erythroid 2-related factor 2/antioxidant response element signaling promotes reductive stress in the human mutant protein aggregation cardiomyopathy in mice. Antioxid Redox Signal. 2011 Mar 15;14(6):957–71.
445. Hornsveld M, Smits LMM, Meerlo M, van Amersfoort M, Groot Koerkamp MJA, van Leenen D, et al. FOXO Transcription Factors Both Suppress and Support Breast Cancer Progression. Cancer Res. 2018 May 1;78(9):2356–69.
446. Ellis MJ, Ding L, Shen D, Luo J, Suman VJ, Wallis JW, et al. Whole-genome analysis informs breast cancer response to aromatase inhibition. Nature. 2012 Jun 21;486(7403):353–60.
447. Banerji S, Cibulskis K, Rangel-Escareno C, Brown KK, Carter SL, Frederick AM, et al. Sequence analysis of mutations and translocations across breast cancer subtypes. Nature. 2012 Jun 21;486(7403):405–9.
448. Wang L, Brugge JS, Janes KA. Intersection of FOXO- and RUNX1-mediated gene expression programs in single breast epithelial cells during morphogenesis and tumor progression. Proc Natl Acad Sci U S A. 2011 Oct 4;108(40):E803-12.
449. Kenny PA, Lee GY, Myers CA, Neve RM, Semeiks JR, Spellman PT, et al. The morphologies of breast cancer cell lines in three-dimensional assays correlate with their profiles of gene expression. Mol Oncol. 2007 Jun;1(1):84–96.
450. Jerry DJ, Kuperwasser C, Downing SR, Pinkas J, He C, Dickinson E, et al. Delayed involution of the mammary epithelium in BALB/c-p53null mice. Oncogene. 1998 Nov 5;17(18):2305–12.
451. Freed-Pastor WA, Mizuno H, Zhao X, Langerod A, Moon SH, Rodriguez-Barrueco R, et al. Mutant p53 disrupts mammary tissue architecture via the mevalonate pathway. Cell. 2012 Jan 20;148(1–2):244–58.
452. Nguyen-Ngoc KV, Cheung KJ, Brenot A, Shamir ER, Gray RS, Hines WC, et al. ECM microenvironment regulates collective migration and local dissemination in normal and malignant mammary epithelium. Proc Natl Acad Sci U S A. 2012 Sep 25;109(39):E2595-604.
453. Kwon K, Beckett D. Function of a conserved sequence motif in biotin holoenzyme synthetases. Protein Sci. 2000 Aug;9(8):1530–9.
454. Udeshi ND, Pedram K, Svinkina T, Fereshetian S, Myers SA, Aygun O, et al. Antibodies to biotin enable large-scale detection of biotinylation sites on proteins. Nat Methods. 2017 Dec;14(12):1167–70.
455. Reyes J, Chen JY, Stewart-Ornstein J, Karhohs KW, Mock CS, Lahav G. Fluctuations in p53 Signaling Allow Escape from Cell-Cycle Arrest. Mol Cell. 2018 Aug 16;71(4):581-591 e5.
456. Marini MG, Chan K, Casula L, Kan YW, Cao A, Moi P. hMAF, a small human transcription factor that heterodimerizes specifically with Nrf1 and Nrf2. J Biol Chem. 1997 Jun 27;272(26):16490–7.

457. Prinz WA, Aslund F, Holmgren A, Beckwith J. The role of the thioredoxin and glutaredoxin pathways in reducing protein disulfide bonds in the Escherichia coli cytoplasm. J Biol Chem. 1997 Jun 20;272(25):15661–7.
458. Walker RA. The complexities of breast cancer desmoplasia. Breast Cancer Res. 2001;3(3):143–5.
459. Paszek MJ, Zahir N, Johnson KR, Lakins JN, Rozenberg GI, Gefen A, et al. Tensional homeostasis and the malignant phenotype. Cancer Cell. 2005 Sep;8(3):241–54.
460. Payne SL, Hendrix MJC, Kirschmann DA. Paradoxical roles for lysyl oxidases in cancer--a prospect. J Cell Biochem. 2007 Aug 15;101(6):1338–54.
461. Triplett JW, O'Riley R, Tekulve K, Norvell SM, Pavalko FM. Mechanical loading by fluid shear stress enhances IGF-1 receptor signaling in osteoblasts in a PKCzeta-dependent manner. Mol Cell Biomech. 2007 Mar;4(1):13–25.
462. Reichelt J. Mechanotransduction of keratinocytes in culture and in the epidermis. Eur J Cell Biol. 2007 Dec;86(11–12):807–16.
463. Lewis JM, Truong TN, Schwartz MA. Integrins regulate the apoptotic response to DNA damage through modulation of p53. Proc Natl Acad Sci USA. 2002 Mar 19;99(6):3627–32.
464. Golubovskaya VM, Cance WG. FAK and p53 protein interactions. Anticancer Agents Med Chem. 2011 Sep;11(7):617–9.
465. Lim S-T, Chen XL, Lim Y, Hanson DA, Vo T-T, Howerton K, et al. Nuclear FAK promotes cell proliferation and survival through FERM-enhanced p53 degradation. Mol Cell. 2008 Jan 18;29(1):9–22.
466. Cooks T, Pateras IS, Tarcic O, Solomon H, Schetter AJ, Wilder S, et al. Mutant p53 prolongs NF-κB activation and promotes chronic inflammation and inflammation-associated colorectal cancer. Cancer Cell. 2013 May 13;23(5):634–46.
467. Damalas A, Weis L, Nordgard S, Kristensen V, Gardner K, Cheng G, et al. Mutant p53 exerts its gain of function through activation of the NF-κB pathway. Breast Cancer Res. 2005;7(Suppl 2):P4.46.
468. Yager JD. Endogenous estrogens as carcinogens through metabolic activation. J Natl Cancer Inst Monographs. 2000;(27):67–73.
469. Cavalieri E, Frenkel K, Liehr JG, Rogan E, Roy D. Estrogens as endogenous genotoxic agents--DNA adducts and mutations. J Natl Cancer Inst Monographs. 2000;(27):75–93.
470. Okoh V, Deoraj A, Roy D. Estrogen-induced reactive oxygen species-mediated signalings contribute to breast cancer. Biochim Biophys Acta. 2011 Jan;1815(1):115–33.
471. Roy D, Cai Q, Felty Q, Narayan S. Estrogen-induced generation of reactive oxygen and nitrogen species, gene damage, and estrogen-dependent cancers. J Toxicol Environ Health B Crit Rev. 2007 Jul;10(4):235–57.
472. Jakovcevic D, Dedic-Plavetic N, Vrbanec D, Jakovcevic A, Jakic-Razumovic J. Breast Cancer Molecular Subtypes and Oxidative DNA Damage. Appl Immunohistochem Mol Morphol. 2015 Dec;23(10):696–703.
473. Karihtala P, Kauppila S, Soini Y, Arja-Jukkola-Vuorinen. Oxidative stress and counteracting mechanisms in hormone receptor positive, triple-negative and basal-like breast carcinomas. BMC Cancer. 2011 Jun 21;11:262.
474. Andrysik Z, Galbraith MD, Guarnieri AL, Zaccara S, Sullivan KD, Pandey A, et al. Identification of a core TP53 transcriptional program with highly distributed tumor suppressive activity. Genome Res. 2017;27(10):1645–57.